MPD

Fast Forward Detector

Technical Design Report

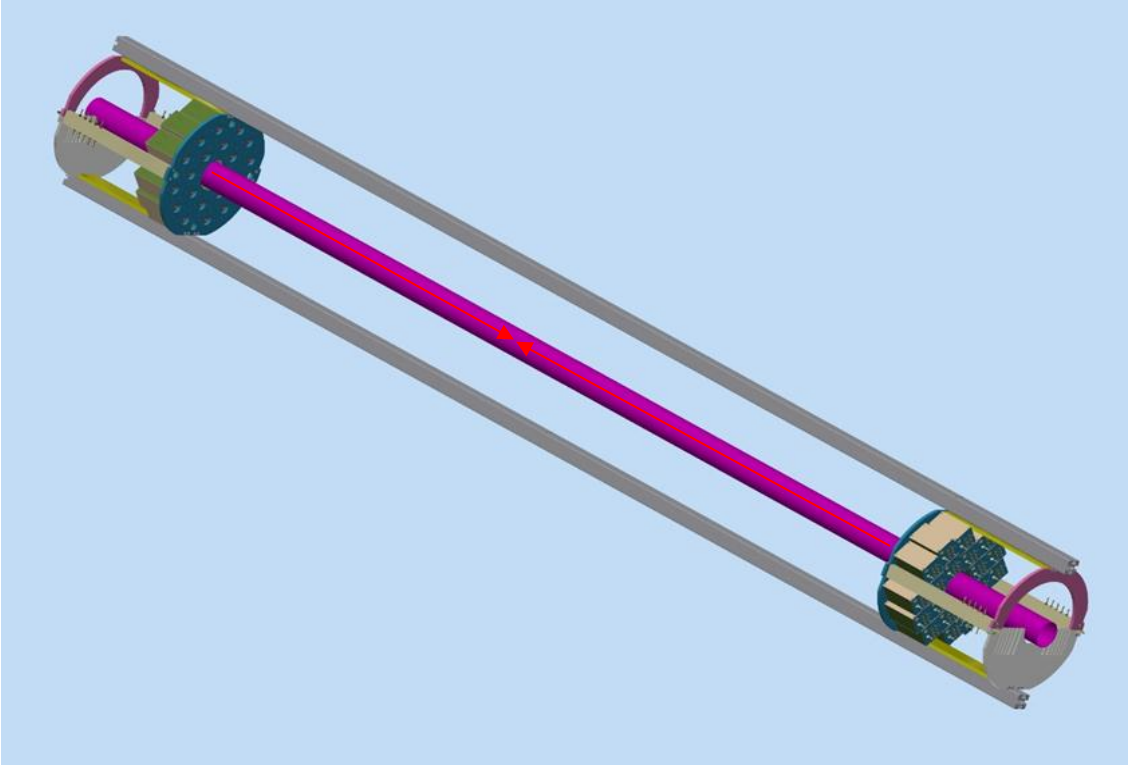

January 2019

FFD group

Project leader: V. I. Yurevich

Participants:

Joint Institute for Nuclear Research, Dubna

S. A. Sedykh, S. V. Sergeev, D. N. Bogoslovsky, V. Yu. Rogov, V. V. Tikhomirov, G. S. Averichev, G. N. Agakichiev, A. A. Timoshenko, N. A. Lashmanov, A. N. Zubarev, G. A. Yarigin, V. A. Pavlyukevich, V. S. Kuzmin

Monte-Carlo simulation of the FFD performance:

Joint Institute for Nuclear Research, Dubna

S. P. Lobastov, A. I. Zinchenko, E. I. Litvinenko, A. G. Litvinenko

Contents

1. Introduction

The Fast Forward Detector (FFD) is an important part of the Multi-Purpose Detector (MPD) setup for study of Au + Au collisions with beams of NICA collider in the energy interval $4 \leq \sqrt{s_{NN}} \leq 11$ GeV. The main aims of the FFD are (i) fast and effective triggering of Au + Au collisions in the center of the MPD setup and (ii) generation of the start pulse for the TOF detector.

Fast triggering of nucleus – nucleus collisions and the precise TOF measurement with picosecond time resolution are important features of all experiments at RHIC and LHC colliders. For these aims a two-arm modular detector with fast Cherenkov or scintillation counters is used.

In the PHENIX experiment, the Beam-Beam Counter (BBC) is used as the start detector [1]. It consists of two arrays of 64 Cherenkov quartz counters located very close to the beam pipe at a distance of ±144 cm from the interaction point (IP) covering a pseudorapidity range of $3.0 < |\eta| < 3.9$. A Hamamatsu R3432 fine mesh dynode PMT is used to detect the Cherenkov light and this PMT is capable of operation in strong magnetic fields. The fully implemented and installed BBC of 128 channels showed a single detector time resolution of 52 ± 2 ps at RHIC for 130 GeV per nucleon Au + Au collisions [2].

The time-zero Cherenkov detectors in the PHOBOS experiment are located at $|z| = 5.3$ m from IP [3]. The resolution of each read-out channel was about 60 ps after corrections of the slewing effect [4] which causes a correlation between the recorded time and the pulse amplitude.

Two arrays of the ALICE T0 detector [5] each consisting of 12 PMTs are located from IP at a distance of 70 cm on one side, covering the pseudorapidity range of $2.9 < |\eta| < 3.3$ and at 370 cm on other side, covering the pseudorapidity range of $4.5 < |\eta| < 5$. The 3.0- cm thick quartz Cherenkov radiators are optically coupled to the fine mesh dynode PMTs FEU-187, produced by Electron Co., Russia. In test runs with a beam of negative pions and Kaons, a time resolution of 37 ps was obtained for the detector with 3.0- cm diameter radiator and better time resolution of 28 ps was obtained with smaller 2.0- cm diameter radiator [6]. Recently a new project of the T0 detector FIT based on MCP-PMTs from Photonis has been proposed [7, 8]. The goals of the detector upgrade are (i) improve the trigger efficiency by increasing the detector acceptance, (ii) combine the functionality of T0 detector (Start Detector), V0 detector

(two arrays of scintillation counters), and FMD (Forward Multiplicity Detector) in one system, (iii) extend the functionality (wide dynamic range, reaction plane, centrality determination), and (iv) to get advanced detector response and reduce the volume occupied by the detector.

The STAR start detector VPD also consists of two identical arrays with 19 read-out channels. Each read-out channel consists of a Hamamatsu R5946 fine mesh dynode PMT, a 1- cm thick scintillator (Eljen EJ-204), and a 6.4- mm Pb converter (~1.13 X_0). The primary photons hit the Pb layer and generate by pair production process some electrons which come in the scintillator and initiate a light pulse. The time resolution of single detector channel changes from 95 ps to ~150 ps measured in Au + Au collisions at $\sqrt{s_{NN}}$ = 39 and 62.4 GeV (2010) and *p* + *p* collisions at energy of 590 GeV (2013) [9].

NICA operates at much lower beam energy than RHIC and LHC. It leads to rather low multiplicity of particles produced in heavy ion collisions and the particles are not ultrarelativistic (even the spectator protons). The kinetic energy and normalized velocity ($\beta = v/c$) of the NICA beams are shown in Fig. 1-1 as a function of $\sqrt{s_{NN}}$.

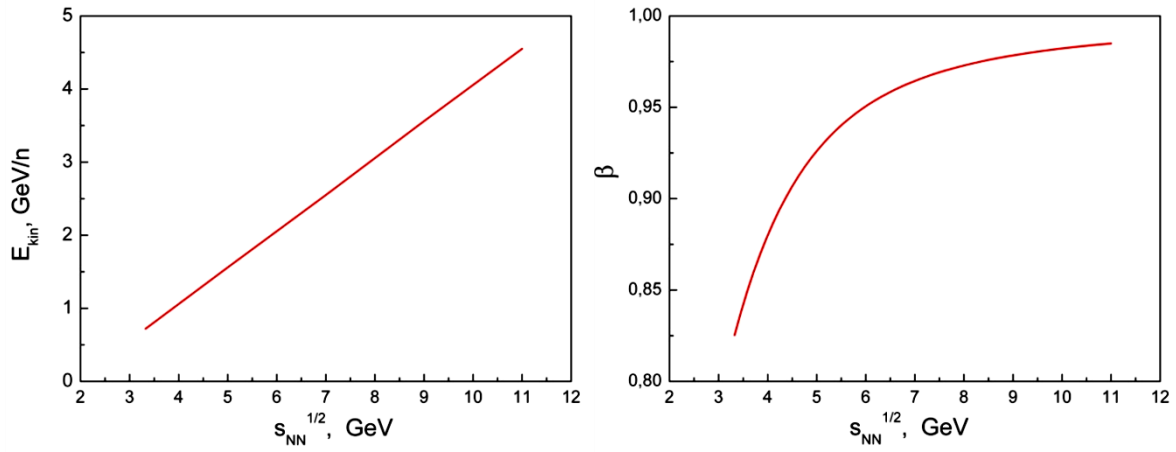

Fig. 1-1. The kinetic energy and normalized velocity of the NICA heavy ions as a function of $\sqrt{s_{NN}}$.

The Monte Carlo simulation of the timing and trigger performance of FFD with the detector position in interval of $100 \leq z \leq 260$ cm from the center of MPD setup showed some degradation of the time resolution and trigger efficiency with the distance. Finally, a position of z = 140 cm was chosen for the FFD sub-detectors.

The time-of-flight spectra of detected charged particles arriving from IP to FFD position of 140 cm from the MPD center are shown in Fig. 1-2 for Au + Au collisions at $\sqrt{s_{NN}}$ = 5 and 11 GeV. The time is calculated as the difference between the arrival time of photons and the

arrival time of charged particles. It is clearly seen that the delay of charged particle arrival reaches of hundreds of picoseconds at the low energy of beam and more than 50 ps for majority of particles at the highest energy.

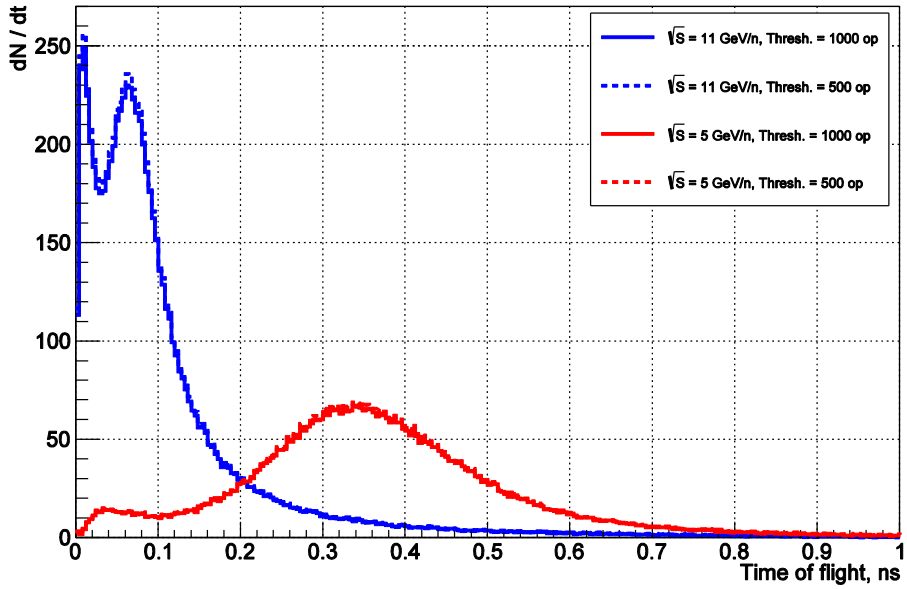

Fig. 1-2. The delay of charged particle arrival in FFD modules in comparison with arrival time of photons for Au + Au collisions at $\sqrt{s_{NN}}$ = 5 (red) and 11 (blue) GeV and FFD position of 140 cm: the solid curves – the threshold of registration is 1000 Cherenkov photons, the dashed curves – the threshold is 500 Cherenkov photons.

As a result, effective triggering on Au + Au collisions and picosecond time resolution of the start signal are two nontrivial problems which must be solved in MPD project.

It is the goal of the Cherenkov Fast Forward Detector to solve these problems by using two advanced modular arrays with large active area and picoseconds time resolution. This is achieved by detecting both high-energy photons from π^0-decays and the fastest charged particles.

The charged particle distributions on pseudorapidity for Au + Au collisions at min. bias and $\sqrt{s_{NN}}$ = 5 and 11 GeV are shown in Fig. 1-3 with intervals covered by the FFD arrays. The same distributions but for emitted high-energy photons are shown in Fig. 1-4. Some primary charged pions, spectator protons and deuterons, and high-energy photons come in the FFD range and form a response of the detector.

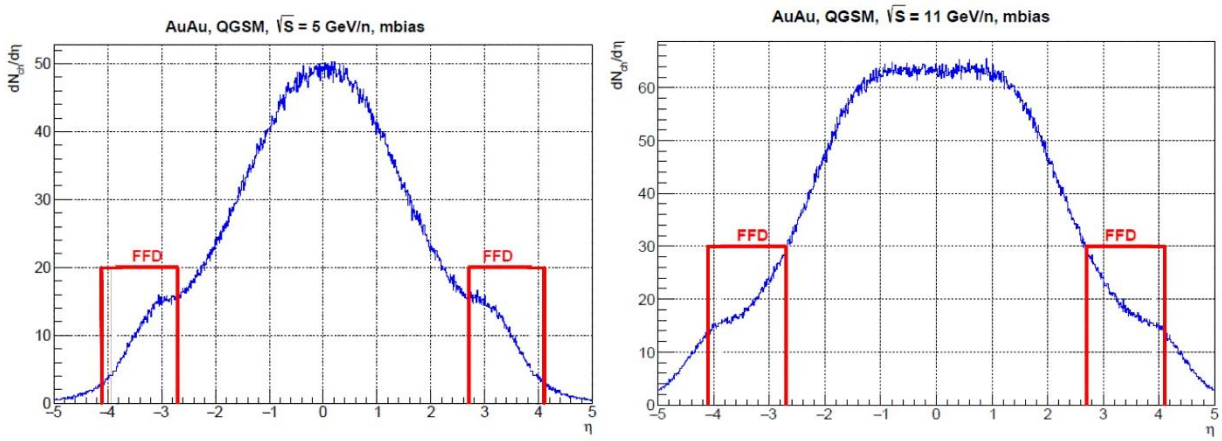

Fig. 1-3. The charged particle distributions on pseudorapidity for Au + Au collisions (min. bias) at $\sqrt{s_{NN}}$ = 5 and 11 GeV. The FFD intervals are indicated in red.

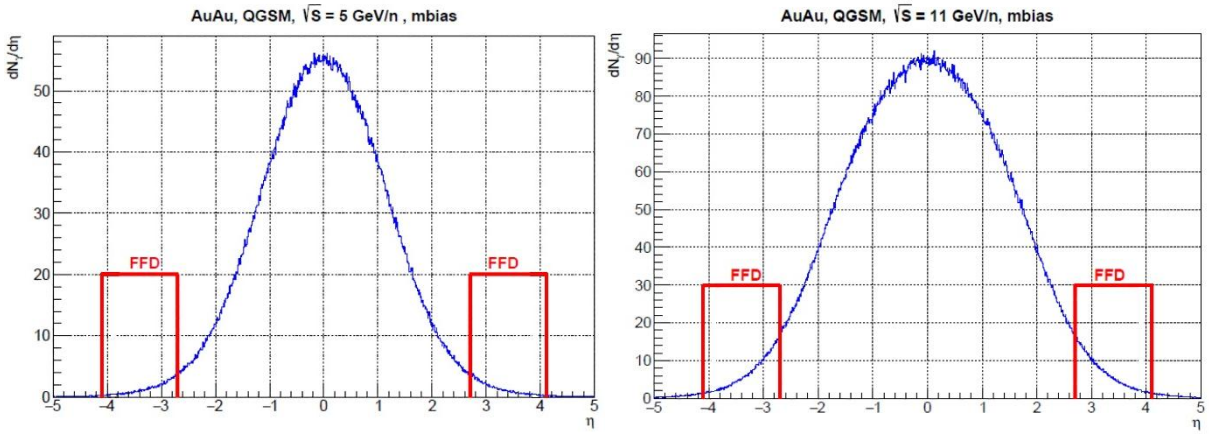

Fig. 1-4. The same as in Fig. 1-2 but for high-energy photons.

A comparison of the vertex-trigger efficiencies simulated for an ideal detector, which active area is a disk with a hole for the beam pipe without dead zones, and for the real modular FFD for Au + Au collisions at low and high energies is shown in Fig. 1-5. In both cases for the central and semi-central collisions the efficiency is 100% and only for the peripheral collisions one some difference appears.

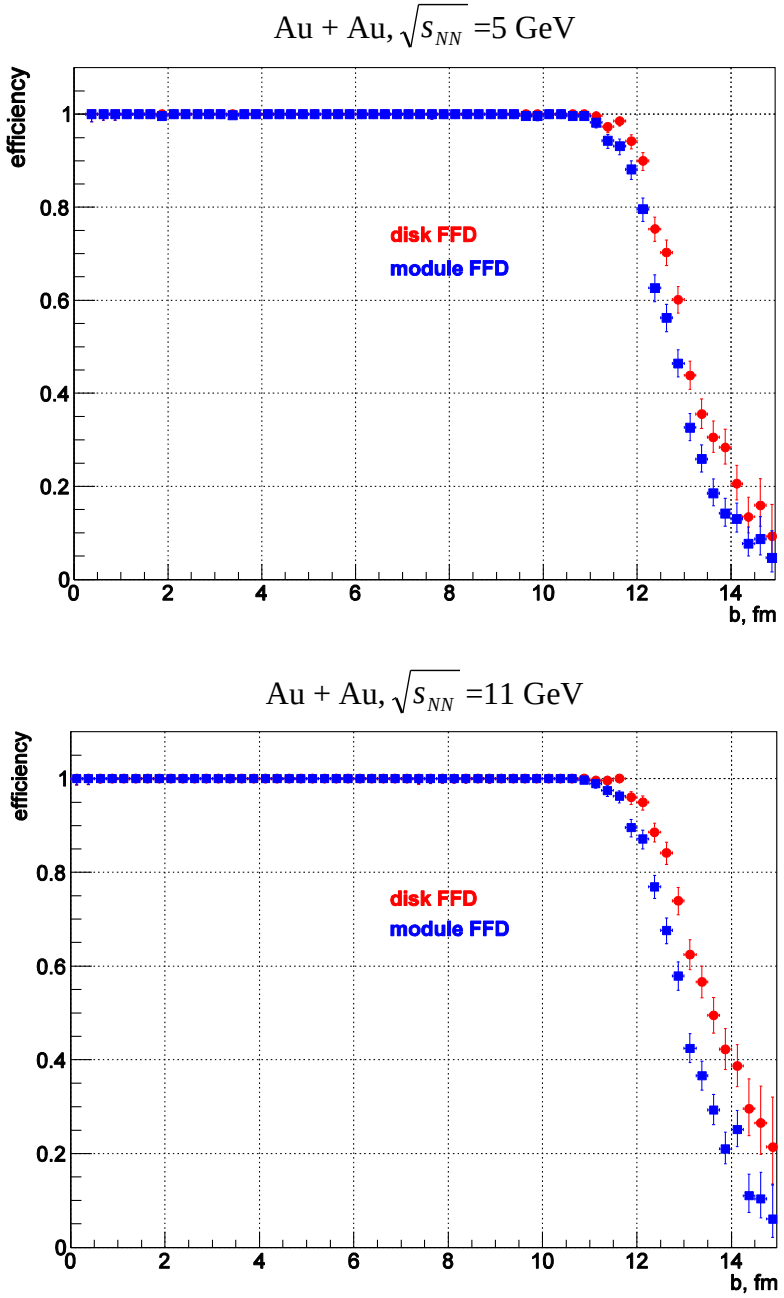

Fig. 1-5. The vertex-trigger efficiencies simulated for an ideal detector, which active area is a disk with a hole without dead zones, and for the real modular FFD for Au + Au collisions at low and high energies.

The energy spectra of photons emitted into the FFD acceptance in Au + Au collisions at $\sqrt{s_{NN}}$ = 5 and 11 GeV are shown in Fig. 1-6. The maximum of photon spectrum for the low energy of beam is ~200 MeV and it shifts to ~350 MeV for the highest beam energy. The spectra overlap a wide energy range from ~50 to 2000 MeV and the FFD must register these photons with a high efficiency to provide the picosecond time resolution of the start signal for the TOF detector.

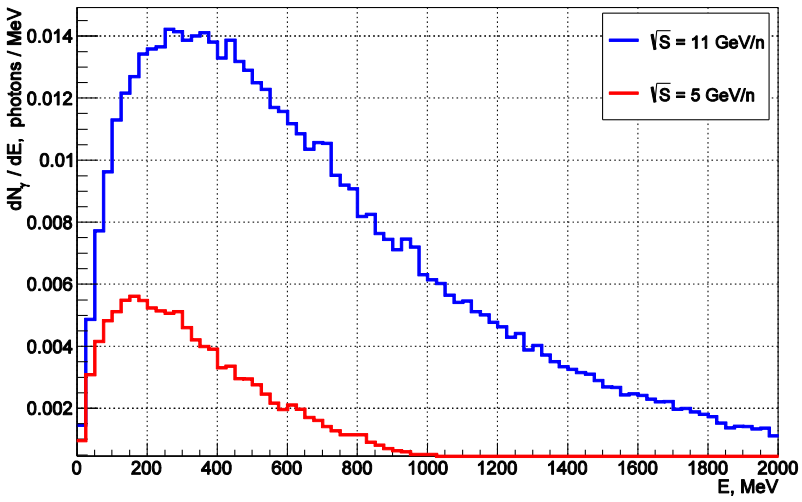

Fig. 1-6. Energy spectra of the photons emitted into the FFD acceptance in Au + Au collisions at $\sqrt{s_{NN}}$ = 5 and 11 GeV.

Some characteristics of the vertex and start detectors of HI collider experiments and FFD/MPD are given in Table 1-1 for comparison. It is clearly seen that the FFD has the largest active area.

Table 1-1. Characteristics of the vertex and start detectors of HI collider experiments.

Experiment	Detector	Active area* (cm^2)	Number of channels*	Distance from IP (cm)	|η|-interval	Photodetector	Time resolution** σ_t (ps)
STAR/RHIC	VPD scintillation	215	19	570	4.25 – 5.1	Hamamatsu mesh dynode PMTs R5946	95 - 150
PHENIX/RHIC	BBC Cherenkov	314	64	144	3.0 – 3.9	Hamamatsu mesh dynode PMTs R3432	52
PHOBOS/RHIC	Cherenkov counters	79	16	530		Hamamatsu PMTs R1924	60
ALICE/LHC	T0 Cherenkov	38	12	70 370	2.9 – 3.3 4.5 – 5.0	Electron mesh dynode PMTs FEU187	28
ALICE/LHC (upgrade project)	FIT Cherenkov	787 674	112 96	70 370	2.2 – 3.3 3.8 – 5.4	Photonis MCP-PMTs XP85012	~40
MPD/NICA	**FFD** Cherenkov	**625**	**80**	**140**	**2.7 – 3.9**	Photonis MCP-PMTs XP85012/A1	**44**

*active area and number of channels of single sub-detector
**single channel time resolution

2. General description of the FFD

2.1. Requirements to the detector

The FFD is the key detector for fast and effective triggering on nucleus – nucleus collisions at the center of the setup with approximately 100%- efficiency for central and semi-central Au + Au collisions identifying *z*- position of the collision with an uncertainty smaller than ±5 cm.

The main requirements for the FFD are:

- fast and effective triggering events of Au + Au collisions in the center of the MPD setup,
- the detector must be able to see each beam crossing (the dead time must be less of 75 ns),
- generation of the start pulse t_0 for the TOF detector with time resolution $\sigma_{t0} < 50$ ps (it corresponds to time-of-flight resolution of <100 ps),
- the detector location must be out of the intervals $-2 < \eta < 2$ and $-125 < z < 125$ cm (that are reserved for the Inner Tracker System (ITS),
- the detector must operate in the MPD magnetic field of $B = 0.5$ T,
- easy installation and de-installation of the detector into the TPC inner tube.

Besides that, there are some additional important tasks where the FFD might be a useful instrument. It can help in the adjustment of beam-beam collisions in the center of the MPD setup with operative control of the collision rate and interaction point position during a run.

The mechanics and geometry of the FFD must be designed and integrated within the MPD setup.

2.2. Concept of the detector

To realize the above requirements at the low energies of NICA, we develop two identical modular sub-detectors FFD_E and FFD_W with large active area placed close to the beam vacuum pipe at a distance of 140 cm to the left and to the right from IP in center of the MPD setup. They cover the pseudorapidity interval of $2.7 < |\eta| < 4.1$ and effectively detect photons from neutral pions decays, charged particles, and low mass fragment-spectators produced in Au + Au collisions as it is schematically shown in Fig. 2-1.

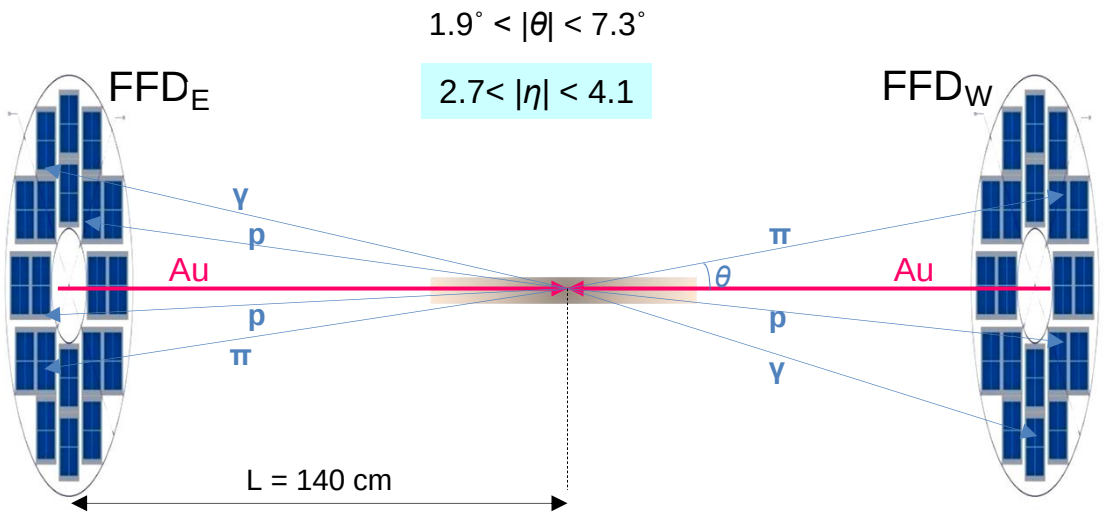

Fig. 2-1. A schematic view of the FFD.

The FFD efficiently detects the high-energy photons by their conversion to electrons in a lead plate with thickness of 10 mm corresponding to ~2 X_0. The similar method was realized in the STAR start detector. The electrons leave the lead plate and pass through a quartz radiator generating Cherenkov light with excellent time characteristics. The Cherenkov light is collected on a photocathode of multianode MCP-PMT XP85012 (Planacon) from Photonis which is suitable for large detector arrays with good granularity and immunity to magnetic field providing excellent time resolution.

Each FFD array consists of 20 identical modules. Front-end electronics board of each module has four independent output channels with pulses from MCP-PMT anode pads. A front view of the FFD array and FFD layout in the MPD setup are shown in Fig. 2-2 and Fig. 2-3 respectively. The inner diameter of the modular array is ~92 mm, the outer diameter is ~360 mm.

The position of the FFD sub-detectors at ±140 cm from the center of the MPD setup was chosen taking into account the following constraints:

- the interval $-125 < z < 125$ cm is occupied by the ITS,
- a longer distance leads to degradation of time resolution and vertex- trigger efficiency,
- the FFD position is close to the end of active area of the TPC and interactions of particles with FFD materials produce only a small background in the TPC (see Chapter 3).

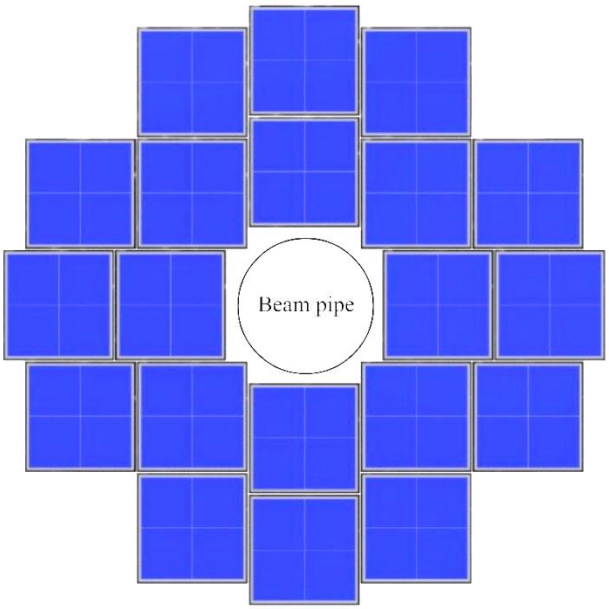

Fig. 2-2. A front view of the FFD array.

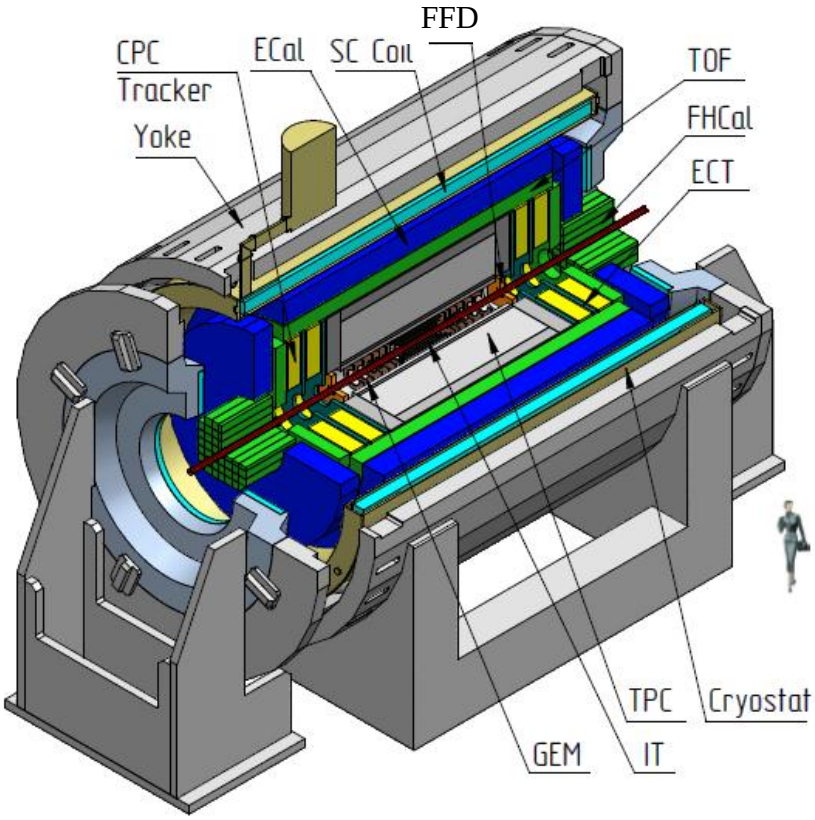

Fig. 2-3. The FFD layout in the MPD setup.

2.3. Fast vertex- trigger

The fast vertex- trigger, provided by FFD, is the main signal of the L0 trigger of MPD. The fast determination of *z*-position of collision point by the vertex requires the appearance of pulses with high amplitudes in both sub-detectors FFD_E (East side) and FFD_W (West side) and it defines the trigger efficiency. For this aim the pulses of each sub-detector are fed to sub-detector electronics unit. Two- threshold method is used to get a good time resolution, only LVDS pulses with lengths above a threshold value (pulses with large amplitudes) are used for production of sub-detector pulses T_E and T_W. The time of generation of these pulses is defined by appearance of the first good pulse from sub-detector modules. The aim of vertex unit is fast measurement of

$$\Delta T = T_E - T_W$$

and checking a condition

$$\Delta T < t_1(z_1) - t_2(z_2)\ ,$$

where the interval $[z_1, z_2]$ defines a selected interval of collision points in center of MPD setup. The variation of path lengths from interaction point to different FFD modules leads to the time uncertainty less than 7 ps.

The trigger efficiency for Au + Au collisions at NICA energies was studied with Monte Carlo simulation (Chapter 3). For all energy range of NICA and impact parameters $b < 11$ fm the efficiency of ~100% was obtained.

The test measurements (section 5.5) and Monte-Carlo simulation (section 3.2) showed that the expected vertex time resolution is ~100 ps (sigma) that corresponds to ~ 3- cm resolution in the *z*- position.

2.4. Start signal for TOF

The start signal for TOF detector requires the appearance of at least one pulse from all FFD channels with good timing and pulse height characteristics. These pulses are used for off-line determination of the start time t_0. The time resolution improves by a factor of $N^{1/2}$, where N is the number of the pulses. But at the NICA energies, in comparison with RHIC and LHC, the number of pulses with good timing is small and the picosecond time resolution of a single detector channel is really important task which is realized in the FFD project.

The time resolution of time-of-flight measurements is

$$\sigma_t = (\sigma_{TOF}^2 + \sigma_{t0}^2)^{1/2},$$

where σ_{TOF} – the time resolution of the TOF detector and σ_{t0} – the time resolution of the start signal. The value σ_{start} is calculated as

$$\sigma_{t0} = (\sigma_{FFD}^2 + \Delta t_{fh}^2)^{1/2},$$

where σ_{FFD} – the time resolution of FFD channel studied experimentally (see Chapter 5), Δt_{fh} – the time uncertainty of the first hit in the FFD (see Chapter 3). There are several different contributions to the time resolution of FFD channel

$$\sigma_{FFD} = (\sigma_{mod}^2 + \sigma_{el}^2 + \sigma_{readout}^2 + \sigma_{meth}^2)^{1/2},$$

where σ_{mod} – the resolution of FFD module itself, σ_{el} – the contribution of FFD electronics and cables, $\sigma_{readout}$ – the contribution of readout electronics, and σ_{meth} – the contribution of method used. The time resolution of FFD module and contributions mentioned above have been studied experimentally (see Chapter 3.2 and 5.4).

Obviously, the smaller the total time resolution gives the better the PID performance. This means that both the TOF time resolution (σ_{TOF}) and the time-zero resolution (σ_{t0}) have to be as small as possible. In the MPD project, requirements to the total time resolution of the TOF system and the time resolution of t_0 pulse are $\sigma_{t0} < 100$ ps and $\sigma_{t0} < 50$ ps.

2.5. The FFD sub-systems

A number of various and important elements and sub-systems are needed for stable operation of the FFD and realization of the detector goals in MPD. The main parts of the detector are schematically shown in Fig. 2-4.

The FFD system consists of two arrays FFD_E and FFD_W which modules are equipped with front-end electronics (FEE) producing output analog and LVDS pulses, two units of sub-detector electronics (SDU) processing the LVDS pulses. These pulses are used for generation of the sub-detector time signal transferred to the vertex electronics unit (VU), estimation of a multiplicity of fired channels, and they are also fed to MPD readout electronics, TDC72VHL. All analog pulses of the detector modules are fed to analog multiplexer and then to a local readout electronics based on CAEN digitizes mod. N6742 used for detector operation control. The picosecond laser calibration system is used for the timing calibration and test of all FFD channels. The low voltage power supply for front-end electronics is a part of the SDU. A multichannel high voltage power supply provides required high voltages for operation of MCP-PMTs in the detector modules. All information provided by FFD sub-detectors is accumulated

in L0 trigger electronics producing a L0 trigger pulse as the first and fastest information about nucleus – nucleus interaction in center of the MPD setup.

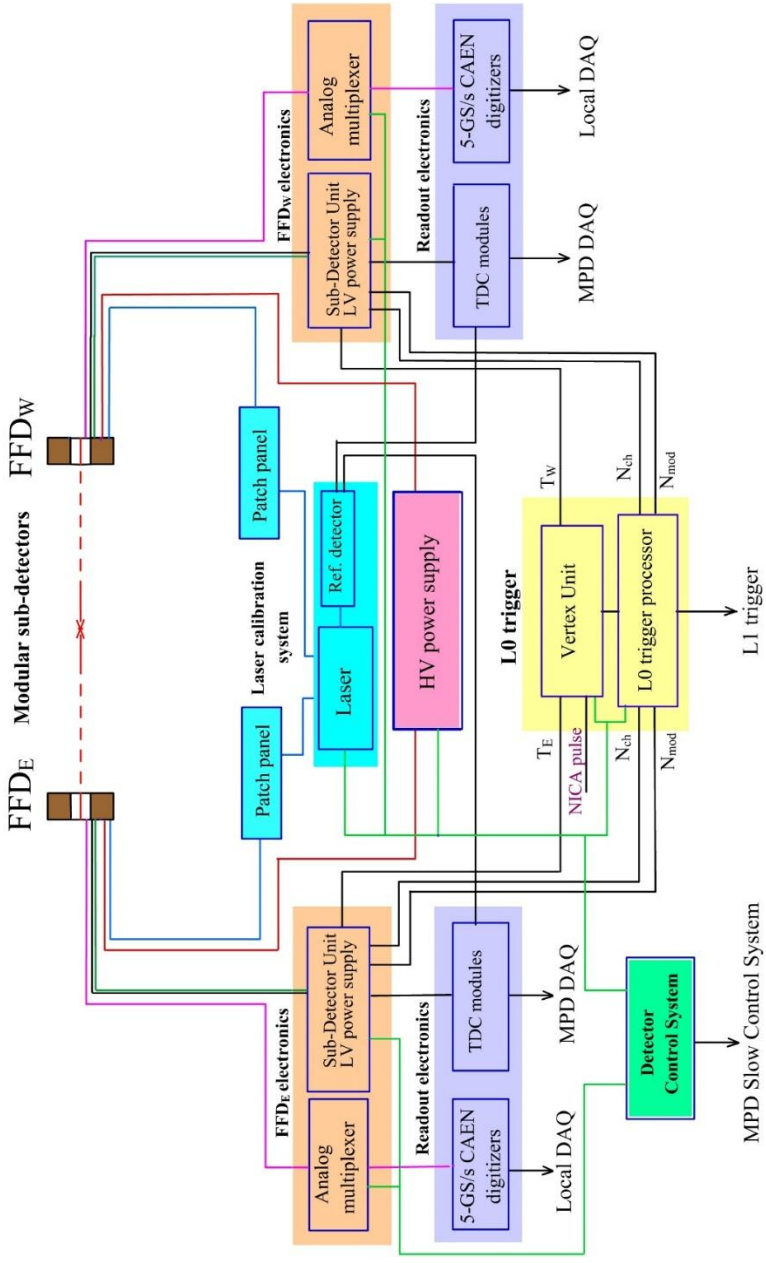

Fig. 2-4. A block-diagram scheme of the FFD system.

The detector control system (DCS) makes a control of the FFD sub-systems and communication with the global slow control system of MPD. The FFD module description and test results are given in Chapters 4 and 5. Other main elements and sub-systems are described in details in Chapters 6 ÷ 10.

3. Detector performance

3.1. General description

The FFD performance was studied by means of Monte- Carlo simulation with QGSM [10 – 12] + GEANT4 codes. The following experimental conditions were taken into account: the MPD magnetic field B of 0.5 T, the vacuum beam pipe made of aluminum tube with 1- mm thickness, the FFD geometry and materials (20 + 20 modules). A fired channel means that the number of Cherenkov photons produced in a single quartz bar of the radiator by a high-energy photon or a charged particle exceeds a threshold set in Cherenkov photons. The simulation was fulfilled for collisions in interval $-50 < z < 50$ cm with $\sigma_z = 25$ cm, in some cases results were obtained for a fixed position of $z = 0$ cm and it is indicated in figure captions.

The vertex and time resolutions were estimated as a time spread of the first detected particle in the FFD sub-detectors. The time resolution of start signal is obtained in off-line analysis of FFD data where the position of collision point is well reconstructed using information from the track detectors. Here, for all the FFD cells (quartz bars), the time of particle arrival is corrected on difference in paths from collision point to the cells. More simple correction procedure is used in on-line determination of the vertex where the arrival time is corrected on difference in paths from the MPD center to the cells. The main items for study were the detector occupancy, the vertex- trigger efficiency, the vertex resolution, the time resolution of start signal for TOF.

For more realistic estimation of characteristics expected in real experiment, the time resolution obtained in tests with detector prototypes with all chain of cables and readout electronics was used.

The study of background detected by FFD and background produced by interactions with FFD materials in TPC is also presented and discussed in this chapter.

3.2. Particle detection and FFD performance

Here the results for chosen distance $L = 140$ cm are presented and discussed as a function of the impact parameter of Au + Au collisions. The mean number of detected charged particles in a single FFD array is shown in Fig. 3-1. The distribution depends on the collision energy. If for the low energy this value increases from central to semi-central collisions by factor of 3

with maximum at $b \approx 8$ fm that for the highest energy it looks flat in region of small impact parameter and from $b \approx 6$ fm it falls with increasing b. In the central collisions the mean number of detected charged particles changes from 12 to 50 with increasing $\sqrt{s_{NN}}$ from 5 to 11 GeV but in peripheral collisions the difference is not visible. The observed peak at $b \approx 8$ fm for $\sqrt{s_{NN}}$ = 5 GeV means that the contribution from spectators exceeds the contribution from emitted hadrons. In the high energy range the number of generated hadrons into FFD acceptance essentially increases that leads to the observed distribution at $\sqrt{s_{NN}}$ = 11 GeV.

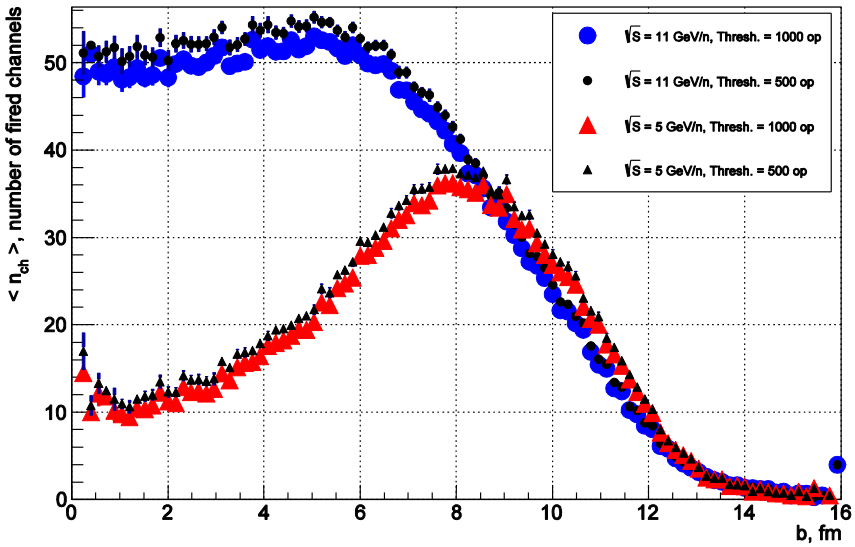

Fig. 3-1. The mean number of detected charged particles in a single FFD array as a function of the impact parameter of Au + Au collisions for two energies $\sqrt{s_{NN}}$ = 5 and 11 GeV and two thresholds of 500 and 1000 Cherenkov photons.

The same distributions but for detected photons in whole FFD are shown in Fig. 3-2. The photons are mainly produced in decay of primary neutral pions generated in the collisions. The numbers of these pions and photons increase with the collision energy and fall with impact parameter with maximum in the central collisions. The maximum mean number of the detected photons increases from 6 to 33 with increasing $\sqrt{s_{NN}}$ from 5 to 11 GeV.

The trigger efficiency for both energies is shown in Fig. 3-3. An important conclusion is that the efficiency is 100% in an impact parameter interval from 0 to 11 fm and it does not depend on the collision energy (only some difference is observed for peripheral collisions).

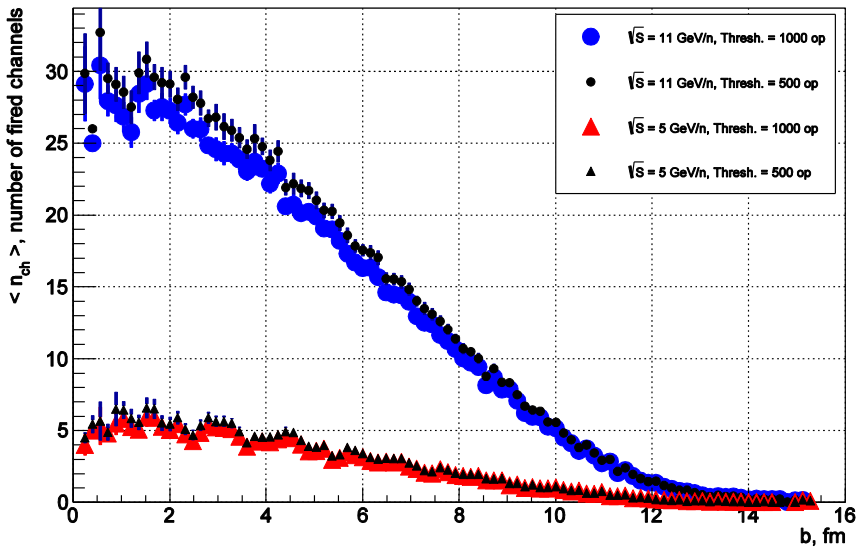

Fig. 3-2. The mean number of detected photons in whole FFD as a function of the impact parameter of Au + Au collisions for two energies $\sqrt{s_{NN}}$ = 5 and 11 GeV and two thresholds of 500 and 1000 Cherenkov photons.

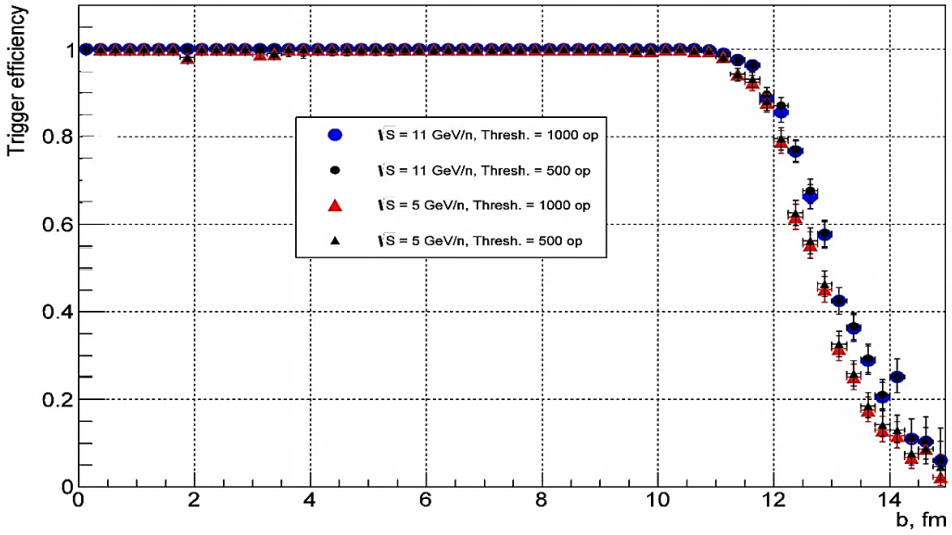

Fig. 3-3. The trigger efficiency as a function of the impact parameter of Au + Au collisions for two energies $\sqrt{s_{NN}}$ = 5 and 11 GeV and two thresholds of 500 and 1000 Cherenkov photons.

A fast coincidence of pulses of the FFD sub-detectors called *Vertex* signal is an origin of the L0 trigger pulse. The obtained vertex uncertainty by detection of the photons and charged particles in FFD arrays is shown in Fig. 3-4. It is better than 1.5 cm for the central and semi-central collisions and the worst case is observed in peripheral collisions at $\sqrt{s_{NN}}$ = 5 GeV.

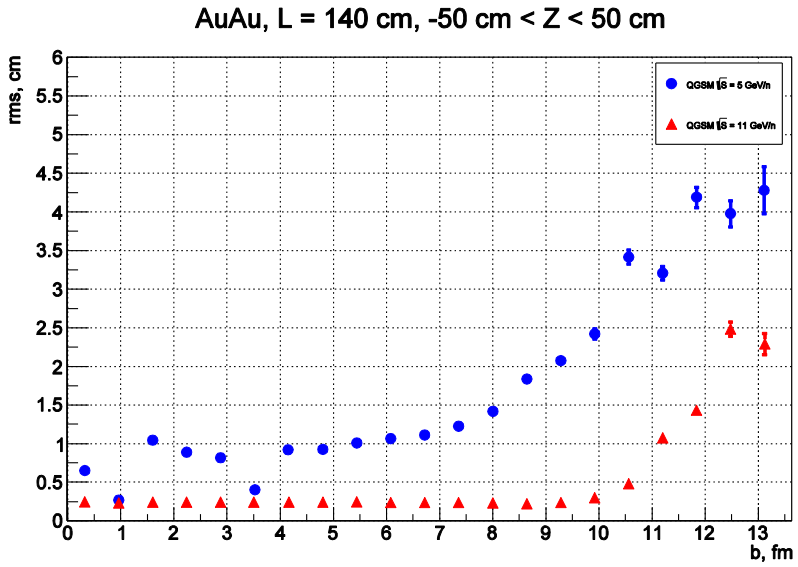

Fig. 3-4. The vertex uncertainty as a function of the impact parameter of Au + Au collisions, the blue points correspond to $\sqrt{s_{NN}}$ = 5 GeV, the red points – to $\sqrt{s_{NN}}$ = 11 GeV.

The time uncertainty of the first hit in FFD shown in Fig. 3-5 is $\Delta t_{fh} < 20$ ps in the impact parameter ranges $b < 8$ fm and $b < 11$ fm at $\sqrt{s_{NN}}$ = 5 GeV and 11 GeV respectively where it has a small dependence on b. Then the time resolution degrades with b and for the peripheral collisions at the low collision energy it becomes worse than 100 ps.

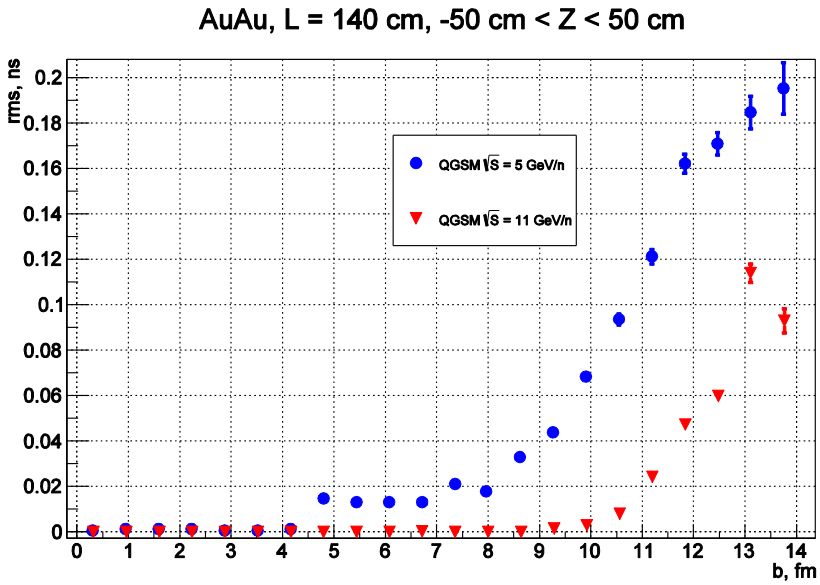

Fig. 3-5. The time uncertainty of the first hit in FFD as a function of the centrality of Au + Au collisions, the blue points correspond to $\sqrt{s_{NN}}$ = 5 GeV, the red points – to $\sqrt{s_{NN}}$ = 11 GeV.

3.3. Estimation of time resolution for real detectors

For estimation of the realistic start signal and time-of-flight resolutions we use the required time characteristics of the FFD and TOF detectors – the time resolution of the FFD channel $\sigma_{FFD} \approx 50$ ps, and the time resolution of the TOF detector $\sigma_{TOF} \approx 80$ ps. The obtained results for $\sqrt{s_{NN}}$ = 5 GeV and 11 GeV are shown in Fig. 3-6, and Fig. 3-7.

The time resolution of the start signal is $\sigma_{t0} \approx 50$ ps at impact parameters $b < 8$ fm for the low energy and at $b < 11$ fm for the highest energy. Together with the TOF detector resolution, it gives the time resolution of time-of-flight measurements σ_t a bit less of 100 ps at $b < 9$ fm for $\sqrt{s_{NN}}$ = 5 GeV and at $b < 12$ fm for $\sqrt{s_{NN}}$ = 11 GeV. The worst case is peripheral collisions at the low energy where σ_t increases with the impact parameter to 200 ps.

Thus, the estimation carried out for the real detectors proves that the FFD performance corresponds to the requirements to the L0 trigger and the start detector of the MPD experiment.

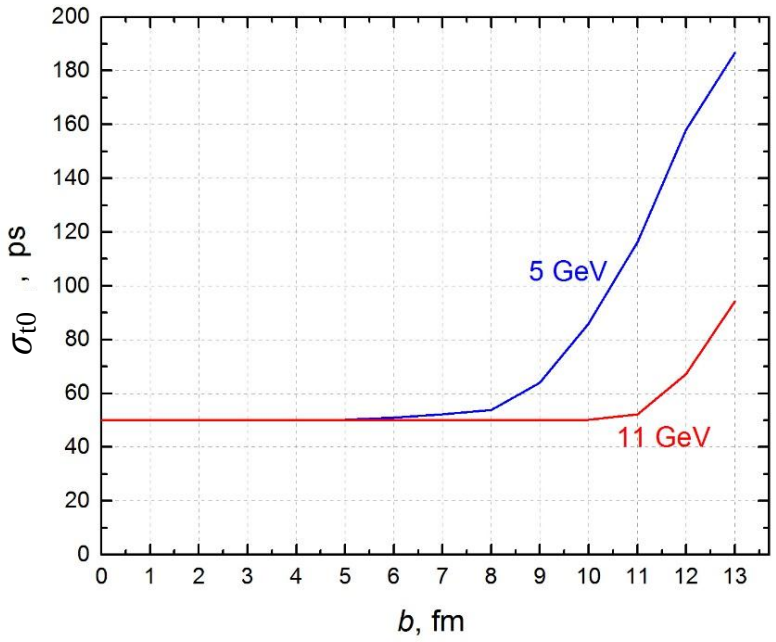

Fig. 3-6. The start signal resolution for Au + Au collisions at $\sqrt{s_{NN}}$ = 5 and 11GeV for the real FFD detector as a function of the impact parameter.

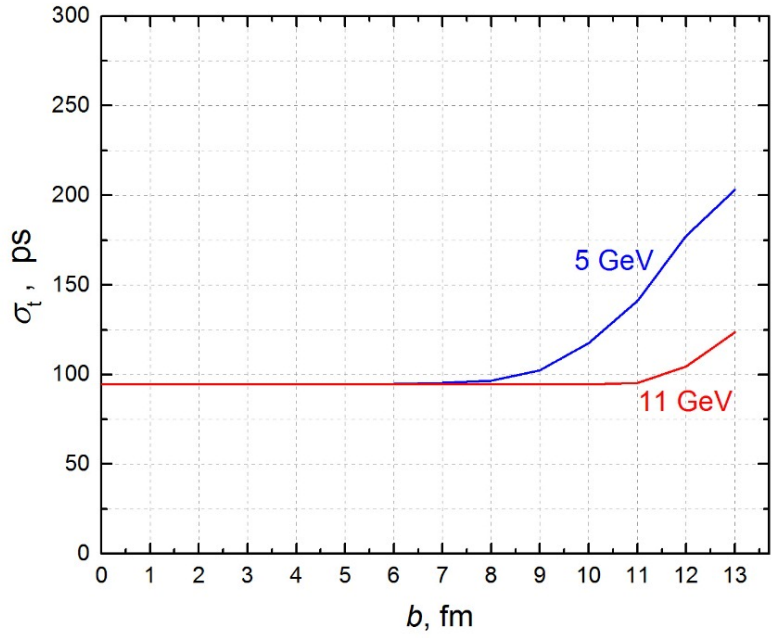

Fig. 3-7. The time-of-flight resolution for Au + Au collisions at $\sqrt{s_{NN}}$ = 5 and 11 GeV for the real FFD and TOF detectors as a function of the impact parameter.

3.4. Background in FFD

Background particles and photons appearing after 10^{-12} s (1 ps) from the moment of Au + Au collision can also be detected in the FFD modules. The sources of this background in MPD are shown for the collisions at $\sqrt{s_{NN}}$ = 11 GeV in Fig. 3-8 and Fig. 3-9 for charged particles and photons respectively. The observed background consists of (1) secondaries produced in decays of unstable particles (the area between IP and FFD location) and (2) particles produced in interactions with MPD materials (beam pipe, ITS, TPC, etc.).

The contributions of background charged particles and photons to the FFD_E + FFD_W response, the number of fired channels, are shown separately in Fig. 3-10 and Fig. 3-11 respectively as a function of the impact parameter for two energies $\sqrt{s_{NN}}$ = 5 and 11 GeV. The number of fired channels increases with the beam energy by a factor of 5 for charged particles and a factor of 6 for photons in central and semi-central collisions and in sum the background reaches of ~14 fired channels for the threshold of 1000 Cherenkov photons in average. It gives ~11% contribution to the FFD response. The most of background secondaries arrive to the FFD during 10 ns after the collision time.

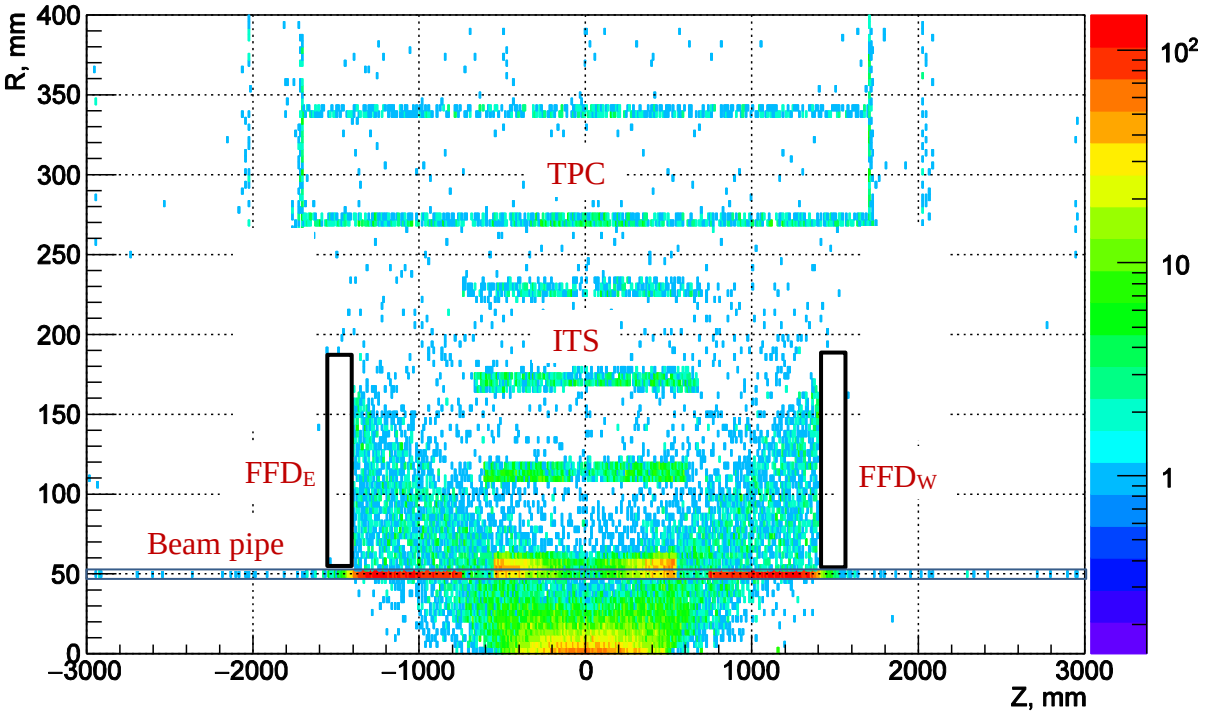

Fig. 3-8. Sources of background charged particles detected in FFD modules for minimum bias Au + Au collisions at $\sqrt{s_{NN}}$ = 11 GeV.

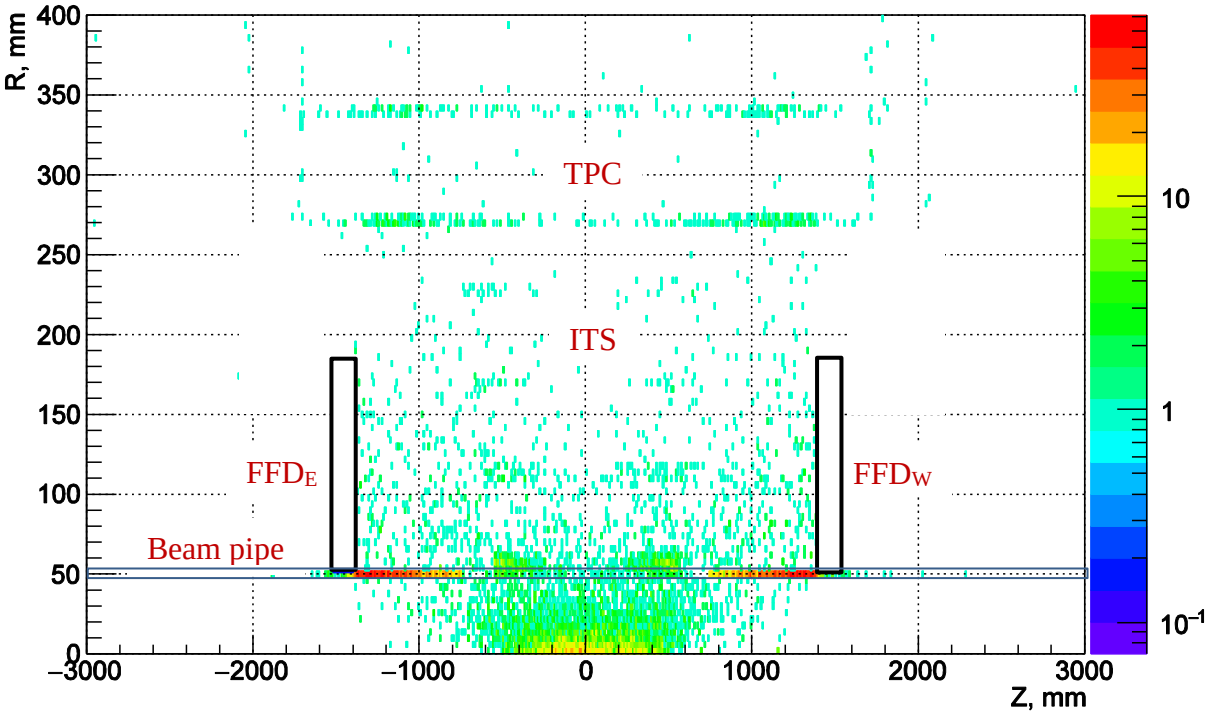

Fig. 3-9. The same as in Fig. 3-14 but for background photons.

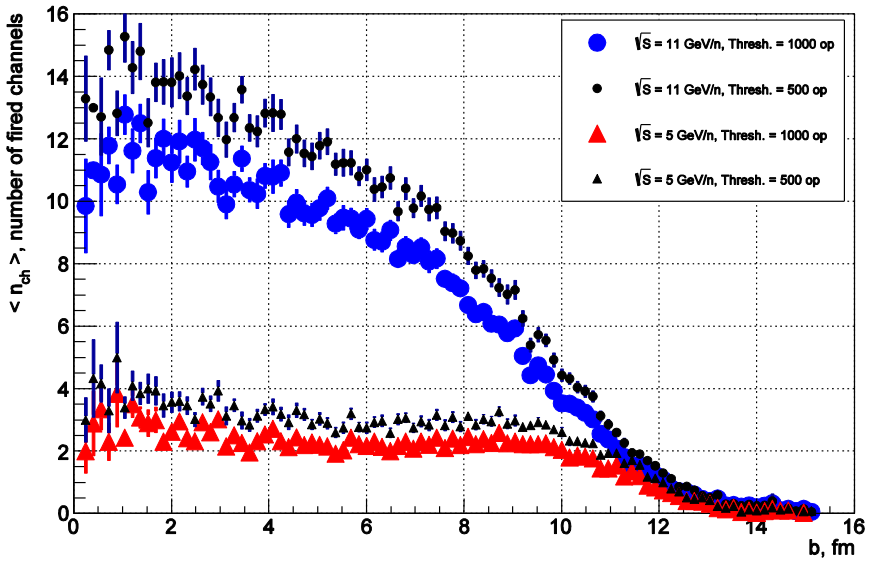

Fig. 3-10. The mean number of fired channels in FFD_E + FFD_W induced by background charged particles for Au + Au collisions at $\sqrt{s_{NN}}$ = 5 and 11 GeV and two thresholds of 500 and 1000 Cherenkov photons.

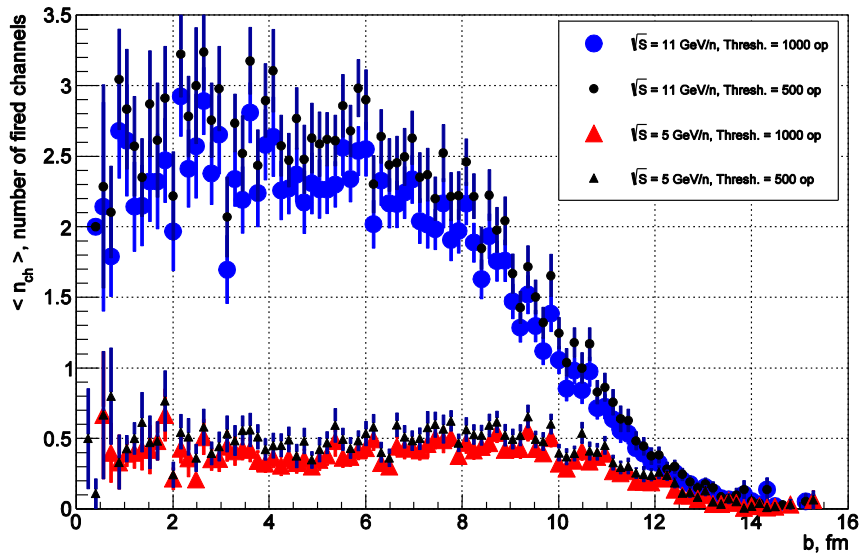

Fig. 3-11. The same as in Fig. 3-16 but for background photons.

3.5. Background induced in TPC

In this section, the production of background hits in the TPC by secondary particles generated in nuclear and electromagnetic interactions in materials of the FFD arrays is discussed.

The efficiency of track reconstruction in the TPC for primaries and secondaries with and without the FFD was simulated for min. bias Au + Au collisions at z = 0, $\sqrt{s_{NN}}$ = 11 GeV, and small L = 100 cm (the worst case). The results are shown in Fig. 3-12 as a function of particle momentum and pseudorapidity. It is clearly seen that there is no visible influence of the FFD on the results.

The number of fired time bin cells of TPC, digits, was calculated for min. bias Au + Au collisions at two energies $\sqrt{s_{NN}}$ = 5 and 11 GeV and FFD distance L = 140 cm. These results are shown in Fig. 3-13 as a function of TPC layer (a row of pads in TPC sectors).

It is clearly seen that for both energies the contribution of background particles coming from FFD (blue points) is small for all TPC layers. This is seen more precisely from the ratios "background digits to all digits" shown in Fig. 3-14 for min. bias and for central Au + Au collisions.

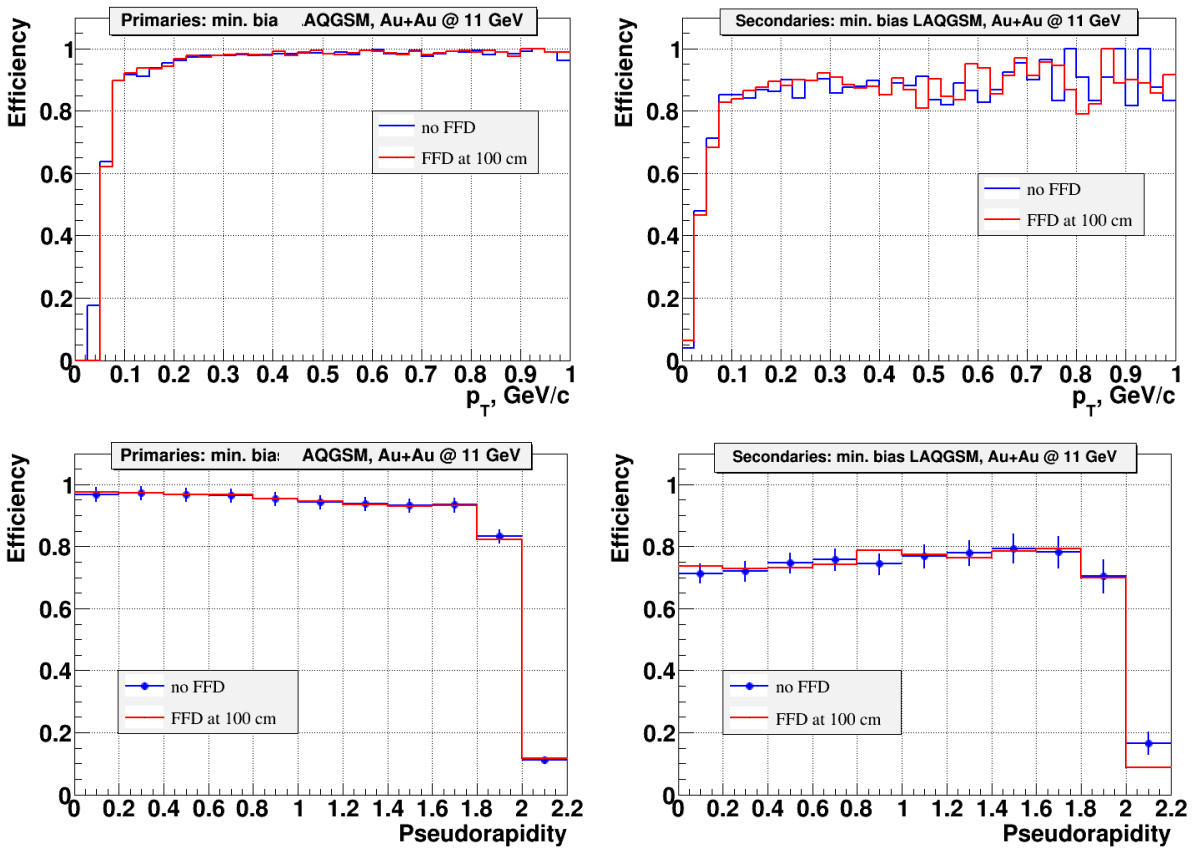

Fig. 3-12. The efficiency of track reconstruction in TPC for primaries and secondaries with and without the FFD for minimum bias Au + Au collisions at z = 0, $\sqrt{s_{NN}}$ = 11 GeV, and L = 100 cm as a function of particle momentum and pseudorapidity.

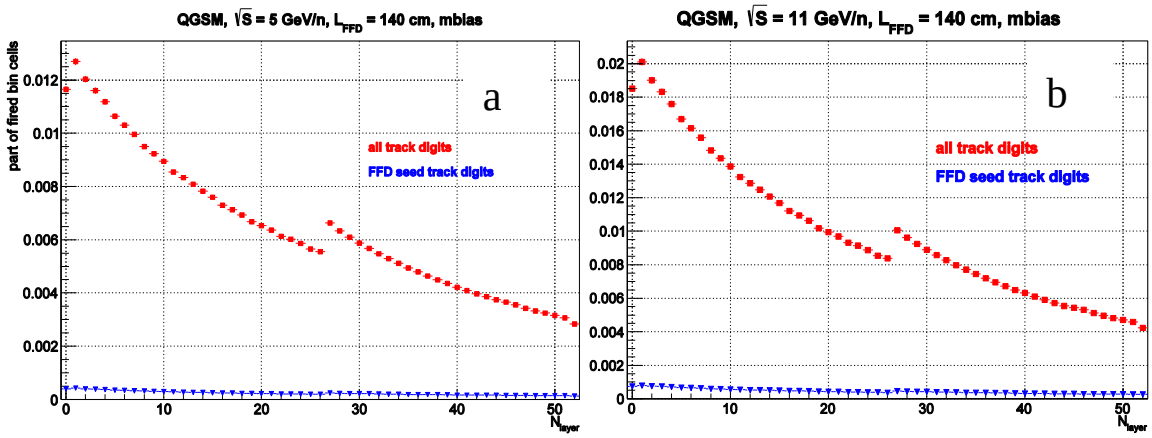

Fig. 3-13. The number of fired bin cells as a function of TPC layer for minimum bias Au + Au collisions at two energies $\sqrt{s_{NN}} = 5$ (a) and 11 GeV (b).

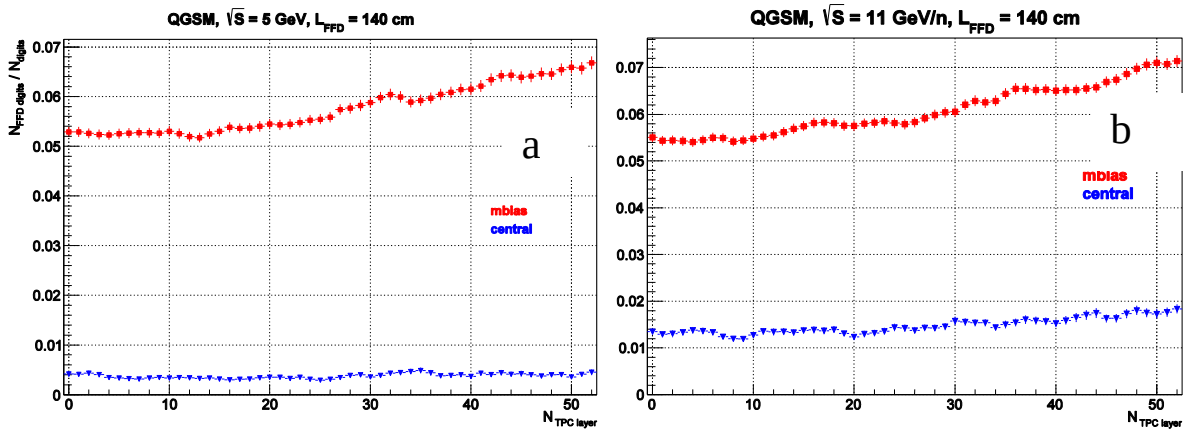

Fig. 3-14. The ratio "FFD induced digits to all digits" as a function of TPC layer for minimum bias (red points) and central (blue points) Au + Au collisions at $\sqrt{s_{NN}} = 5$ (a) and 11 GeV (b).

For minimum bias events the background contribution varies from 5.5% to 6.5%. For central collisions the background contribution is much smaller, it is only ~0.4% at 5 GeV and ~1.5% atthe maximum energy.

Thus, one may conclude that the FFD materials as source of background for the TPC give rather small contribution to TPC response at any layers, collision energy and centrality.

4. FFD module

4.1. General description

The modules of the FFD arrays are Cherenkov detectors for high-energy photons and charged particles. The FFD module must be compact with cross section close to MCP-PMT size to reduce dead space in FFD array. The FFD modules must provide the required time resolution $\sigma_{t0} \leq 50$ ps and produce signals for the vertex and L0 trigger electronics. Also, the detector modules must operate in the MPD's magnetic field with $B = 0.5$ T.

The module has 2 × 2- cell design and the main elements are:

- 10-mm lead plate (~$2X_0$) of high-energy photon converter,
- Cherenkov radiator – 4 quartz bars, 28 × 28 × 15 mm^3 each,
- photodetector MCP-PMT XP85012/A1-Q (S),
- frontend electronics board (FEE),
- module housing with connectors.

4.2. Module design

A module scheme is shown in Fig. 4-1. The module size is 66 × 66 × 110 mm^3, the mass is ~1.5 kg. The quartz radiator with cross section of 56 × 56 mm^2 gives the occupancy of 72%. The module elements are shown in Fig. 4-2.

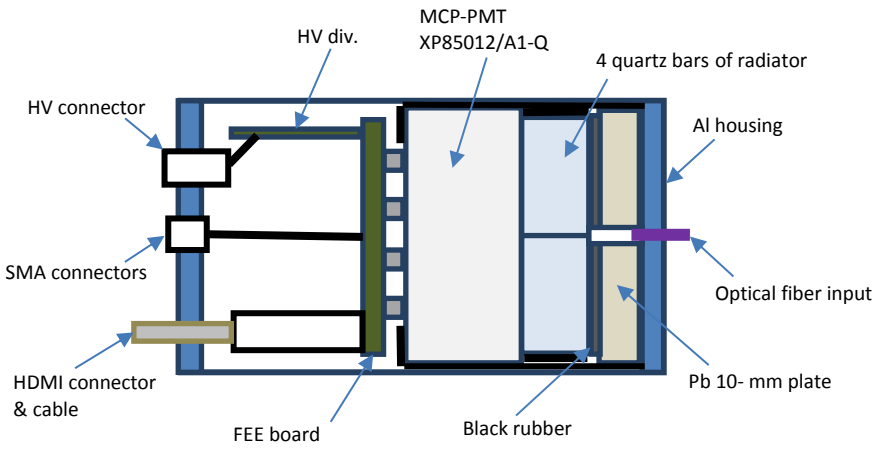

Fig. 4-1. A scheme of the FFD module.

Since 2010 several versions of module prototype were designed, produced, and tested with a laser LED, a deuteron beam of Nuclotron, and cosmic rays. Several module prototypes were produced and tested in 2014 – 2016, one unit is shown in Fig. 4-3. The final production of 40 units of the FFD modules will be made in the 2018 – 2019 period.

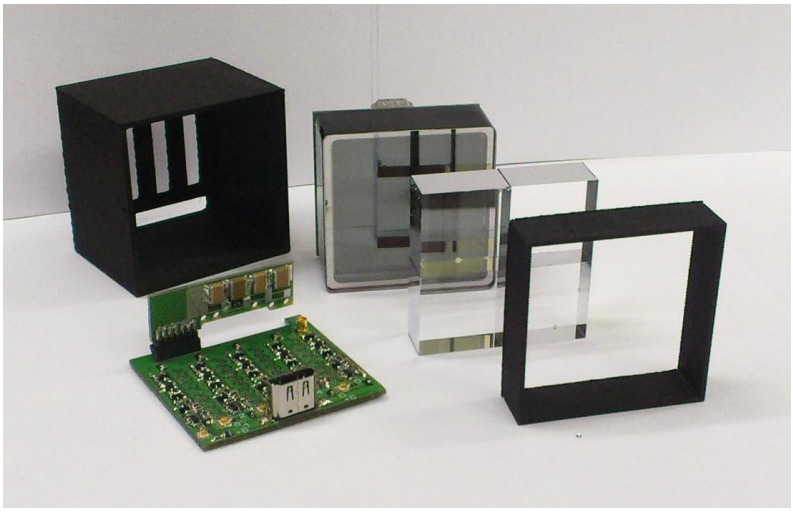

Fig. 4-2. A photo of some elements of the FFD module: the plastic box, the FFE plate with HV divider, the MCP-PMT, the quartz radiator, the plastic frame of the radiator.

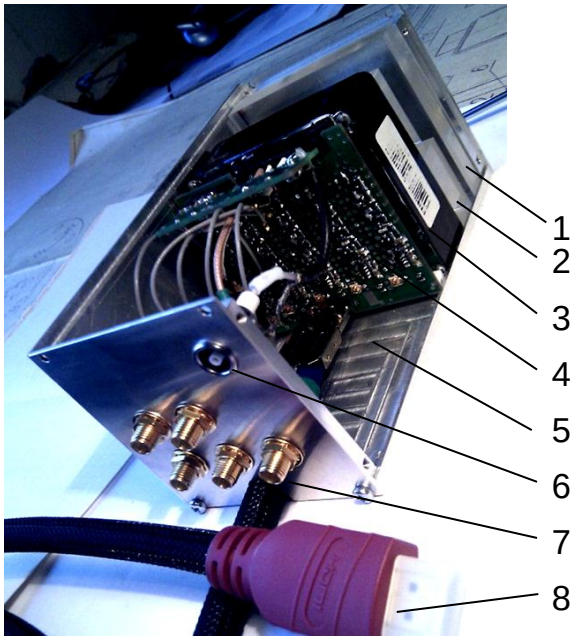

Fig. 4-3. Prototype of FFD module: 1 – the lead plate, 2 – the quartz bars, 3 – MCP-PMT XP85012/A1, 4 – the FEE board, 5 – the module housing, 6 – the HV connector, 7 – the SMA outputs of analog signals, 8 – the HDMI cable (LVDS signals + LV for FEE).

4.3. Photodetector

The appearance of Planacon [13, 14] provoked a wide development of advanced detectors with picosecond time resolution for present and future experiments, e.g. BaBar [15], ATLAS [16], Belle [17], LHCb [18], and PANDA [19]. This device, shown in Fig. 4-4, is sensitive to visible and ultraviolet light. It has a rectangular shape with a photocathode of 53×53 mm^2 that occupies 81% of the front surface. This is very important for fast Cherenkov detectors with dense packing of PMTs into a large-scale detector array.

Careful experimental tests with picosecond lasers, relativistic beams of single-charged particles, and in magnetic fields with ramping up from zero to 1.5 T were carried out by different groups with aim to study the most critical characteristics of the MCP-PMTs for developing a new generation of detectors with picosecond time resolution [17, 19, 20, 21]. These studies showed the following: (i) signals from anode pixels are characterized by a fairly flat response with variation factor of 1.5 and rather low cross talk, (ii) the single photon time resolution does not depend on the magnetic field, (iii) Planacon XP85012 has stable operation up to single photon rates of ~1 MHz/cm^2 at gain 10^6, (iv) the lifetime depends on the integrated anode charge.

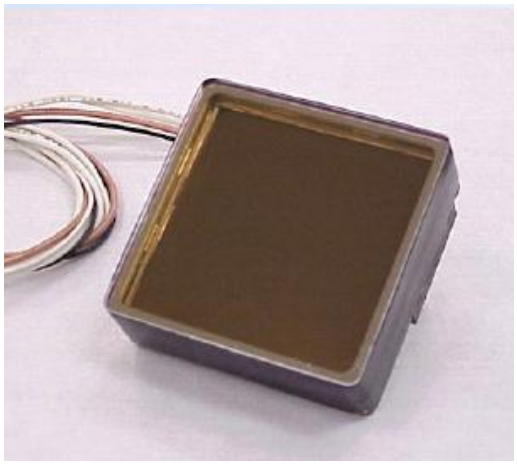

Fig. 4-4. A view of MCP-PMT XP85012/A1 (Photonis).

Main characteristics of XP85012/A1-Q are listed below

- Planacon size: $59 \times 59 \times 24.5$ mm^3
- Photocathode of 53×53 mm^2 occupies 81% of front surface
- 2- mm quartz input window

- Sensitive in visible and ultraviolet region
- 8 ×8 multianode topology
- Chevron assembly of two MCPs
- MCP pore size: 25 μm
- HV_{max} : - 2000 V
- Typical gain factor: $\sim 10^5 \div 10^6$
- Rise time: 0.6 ns
- Transit time spread, σ_{TTS} : ~ 37 ps
- Low noise, dark current: 1 ÷ 3 nA (typical)
- High immunity to magnetic field
- Mass: 128 g

The tests carried out by the DIRC group from the PANDA experiment at FAIR showed that the gain of XP85012 decreases only by a factor of 10% with increasing anode charge up to 100 mC/cm^2 (moreover, experts of Photonis inform that lifetime of Planacon devices has been recently much increased). This leads to the conclusion that the FFD modules based on MCP-PMTs XP85012 will operate without significant change of characteristics during about 10 years of beam time. This estimation is based on the beam conditions planned for MPD/NICA, results of our simulation, and low gain regime of the MCP-PMT operation.

Operation of Planacon at low gain demonstrates good time resolution and gives some advantages. It is better for aging and rate issues. Also, by lowering the gain, the detector becomes sensitive only to relativistic charged particles traveling through the Cherenkov radiator. It does not see the background with a few photoelectrons from γ-rays. Additional amplification is provided by fast front-end electronics (FEE).

The study of results obtained with various photodetectors in other laboratories [20] led us to the conclusion that MCP-PMT Planacon XP85012/A1-Q is the best solution for our application and it covers all requirements to the photodetector of FFD module.

The high immunity to magnetic field of the MCP-PMTs is a crucial factor in our case because the FFD will function in the strong magnetic field of the MPD with B = 0.5 T.

The quantum efficiency of XP85012/A1-Q is shown in Fig. 4-5 and a device drawing is shown in Fig. 4-6.

The list of MCP-PMTs purchased for FFD is shown in Table 4-1. The types with “Q” and “S” mean the Planacons with different material of the photocathode window: Q – quartz and S – sapphire. Both types have good transparence in UV region but the photodetectors with sapphire window have better protection of MCP-PMT vacuum against helium.

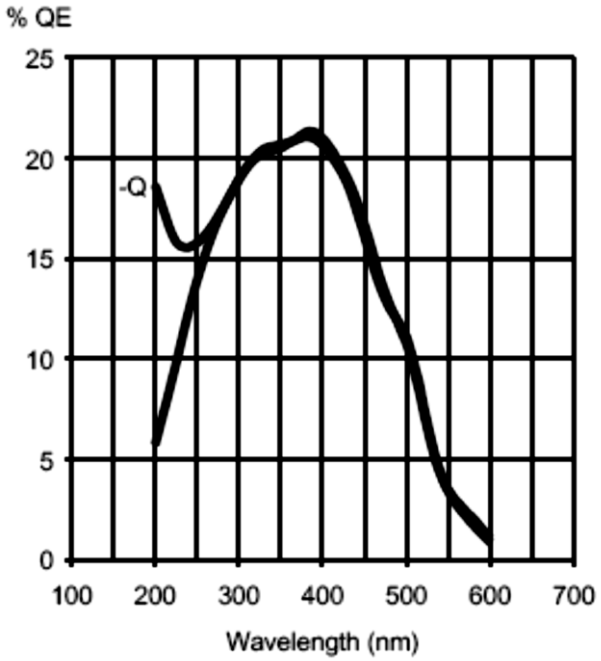

Fig. 4-5. The quantum efficiency of XP85012/A1-Q.

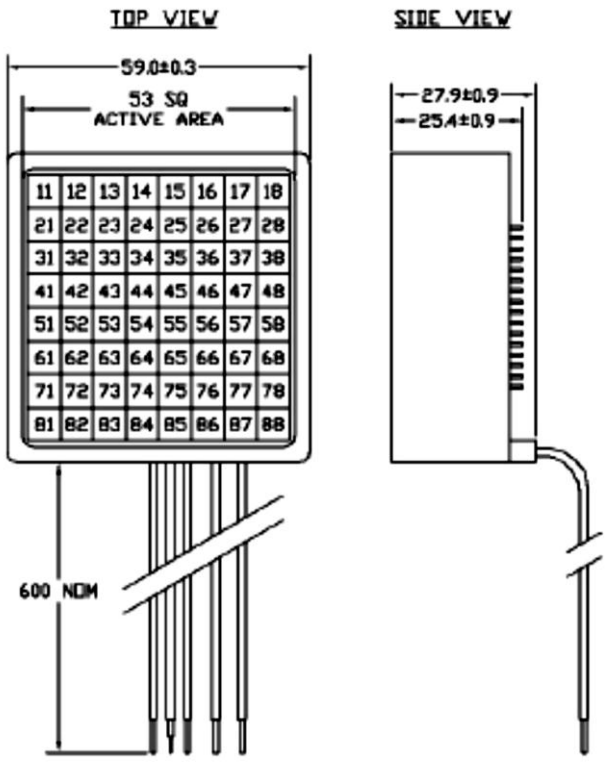

Fig. 4-6. The drawing of XP85012/A1.

Table 4-1. Status of purchase of MCP-PMTs.

#	Type	Date	Units	Comments
1	XP85012/A1	03.2010	2	used in the first tests
2	XP85012/A1-Q	09.2012	6	used for tests with prototypes (in reserve)
3	XP85012/A1-Q	09.2013	20	used in modules of the FFD_E sub-detector
4	XP85012/A1-S	10.2015	1	used for tests (in reserve)
5	XP85012/A1-S	08.2016	20	used in modules of the FFD_W sub-detector

4.4. Lead converter

The photons are detected in the FFD module via conversion to electrons in a lead plate placed in front of the quartz radiator. The efficiency of photon registration depends on the converter thickness and the photon energy. The efficiency of photon detection by FFD module was studied with MC simulation for different thickness of the lead converter in photon energy interval covered by the energy spectrum of photons produced in Au + Au collisions and shown in Fig. 1-6. The converter thickness was varied from 3 to 20 mm. The obtain results are shown in Fig. 4-7 for two thresholds of 500 and 1000 Cherenkov photons in quartz bar.

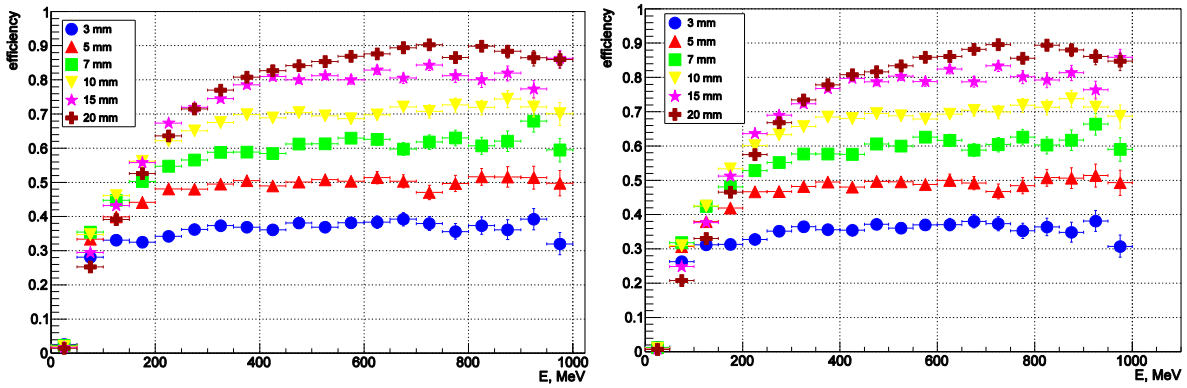

Fig. 4-7. The efficiency of photon detection as a function of the photon energy for six different thicknesses of the lead converter from 3 to 20 mm: the left figure – the threshold of 500 Cherenkov photons, the right figure – the threshold of 1000 Cherenkov photons.

Finally, a 10- mm lead converter was chosen. It provides high detection efficiency both in the range of maximum of the photon spectrum and for higher energies of photons.

4.5. Radiator

In accordance with the 2 × 2- cell structure of FFD module, the radiator consists of a set of four quartz bars. The radiator has to be thick enough to get a large number of photoelectrons N_{pe} from the photocathode. The measurements performed by several groups [20] show that the time resolution degrades very rapidly as N_{pe} goes down for shorter radiator length and one needs at least a 10- mm thick radiator plus a 2- mm thick window, or N_{pe} ~ 30 photoelectrons, to get good time resolution at low gain.

We choose a 15- mm thickness for the quartz bar as a compromise value because further increasing of the thickness gives worse time resolution due to the larger time dispersion of Cherenkov photon arrival on the MCP-PMT photocathode [20]. The 160 quartz radiator bars 28 × 28 × 15 mm^3 with polished surfaces and thin aluminum layer for photon reflection on the side surfaces were produced from high quality optical quartz KU-1 by "Fluorite" Co., St. Petersburg.

Silicon oil from Dow Corning Co. with high transmittance for UV photons is used as optical grease between the quartz bars and the quartz window of XP85012/A1-Q.

A high-energy photon can produce from one to several energetic electrons in the lead plate. Some of these electrons pass through the quartz radiator and generate a large number of Cherenkov photons. The Cherenkov photon multiplicity was studied with MC simulation for different energies of incoming photons 50, 100, 200, and 500 MeV, the results are shown in Fig. 4-8.

The first peak at ~1850 Cherenkov photons corresponds to single electron escaping the lead converter and passing through the quartz radiator. The distribution depends on a photon energy and for 500- MeV photons the maximum number of Cerenkov photons reaches 20 000. Thus, the dynamical range of the pulse height generated by photons is equal to ~ 10.

The time resolution improves with the number of photoelectrons produced by Cherenkov photons in MCP-PMT photocathode. The aim is to increase this number as much as possible. The number of Cherenkov photons produced in a radiator with length L by charged particle with $Z = 1$ and $\beta = 1$ is calculated by formula

$$N_{ph} = 2\pi\alpha L \int_{\lambda_1}^{\lambda_2} \left(1 - \frac{1}{n^2(\lambda)}\right) \frac{1}{\lambda^2} d\lambda \ .$$

The estimation of N_{ph} in the UV region and the region of XP85012/A1-Q sensitivity is given in Table 4-2 together with the photoelectron number N_{pe}.

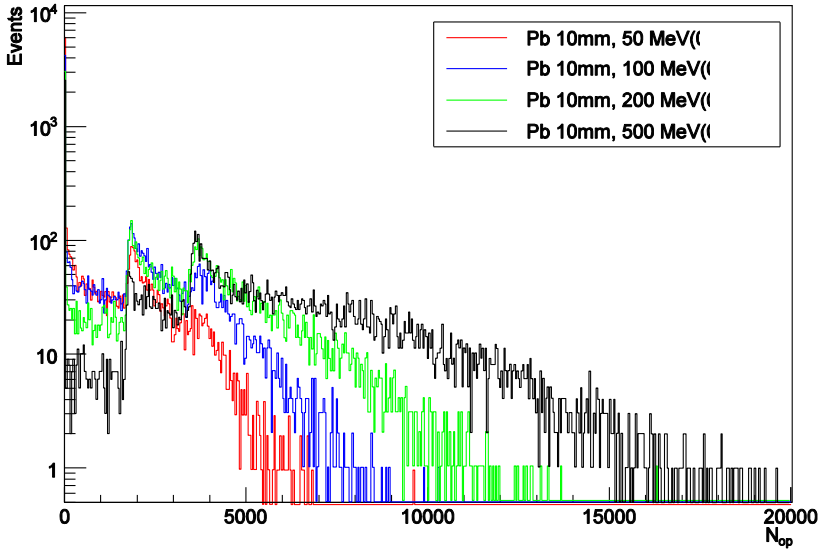

Fig. 4-8. The simulated distributions of Cherenkov photon number for different energies of incoming photons 50, 100, 200, and 500 MeV.

Table 4-2. The estimation of N_{ph} and N_{pe} for UV region and a region of XP85012/A1-Q sensitivity.

Number	$170 < \lambda < 270$ nm	$170 < \lambda < 670$ nm
N_{ph}, photons	979	1909
N_{pe} , photoelectrons	147	278

It is clearly seen that the contribution of UV region to Cherenkov detector response is ~50%.

In a real detector some fraction of the Cherenkov photons is lost and this leads to some decrease of the number of photoelectrons.

4.6. Front-end electronics

In accordance with the FFD design, the MCP-PMT XP85012/A1 output of 64 anode pads is transformed into a 4- channel photodetector by merging16 pads (4 × 4) into a single channel. The common MCP output is used for control of the FFD operation. Thus, the front-end electronics board (FEE) has 4+1 independent channels producing analog and low-voltage differential signaling (LVDS) pulses. The LVDS pulses of all channels are fed to the sub-detector electronics unit (SDU) and after splitting one branch is transferred to TDC72VHL modules of readout electronics and other is processed in correspondence with an interaction trigger logic. The analog pulses are fed to digitizers CEAN mod. N6742 for adjusting of FEE characteristics and HV values and for control of the detector operation.

A functional scheme of a single FEE channel is given in Fig.4-9. The main elements are a low-noise input amplifier with BFR93A transistor, a pulse shaper minimizing signal to noise ratio, a RC chain filtering signal frequency, a fast amplifier of ~40 dB gain with MAR-8 chip of DC – 8GHz bandwidth, and LMH7220 discriminator (1.2 GHz, Low Distortion Operational Amp).

The length of the LVDS pulses depends on the pulse height of the MCP-PMT signal. The pulses with maximal width correspond to signals with the largest amplitudes. The FFD modules operate at MCP-PMT gain of ~10^5 and FEE amplifier gain of ~30-50. The analog pulse rise time is ~1.3 ns and the LVDS pulse widths of accepted signals are above 6 ns.

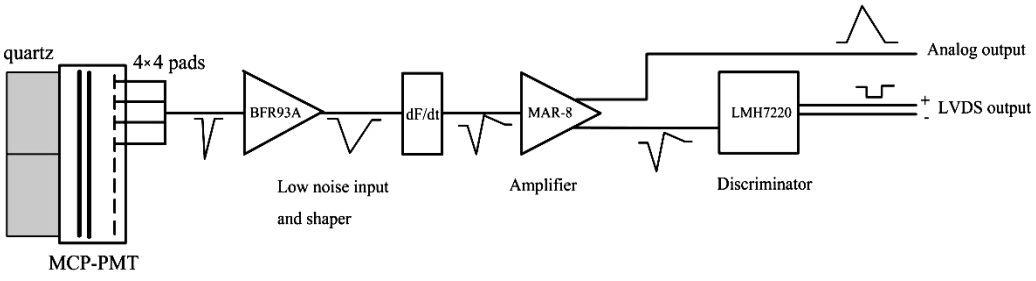

Fig. 4-9. A functional scheme of a single FEE channel.

5. Test measurements and results

5.1. General description

Many different tests with FFD module prototypes were carried out with a laser LED, cosmic muons, a deuteron beam of Nuclotron, and in a magnetic field. The goal of the tests is to study the module characteristics and module performance. The items of this study are

- Optimal operation regime (HV and FEE gain),
- Detector response,
- Time resolution of FFD modules,
- Time resolution of FFD – RPC (TOF detector),
- Influence of cable and electronics chain on time resolution,
- Detector performance in magnetic field.

Two different methods of readout were used in the test measurements: (1) Evaluation Board DRS4 digitizer [22] or CAEN mod.N6742 digitizer based on DRS4 chip and (2) time-to-digital converters TDC32VL or TDC72VHL, VME modules produced in LHEP/JINR [23].

In 2014 – 2015 period, main experimental results were obtained with readout electronics: E. B. DRS4 V4 digitizer and TDC32VL. Since 2016 novel modules of readout electronics, E. B. DRS4 V5 digitizer, CAEN digitizer, and TDC72VHL are used in our tests in laboratory and with beams of Nuclotron. Contribution of these readout electronics to the time resolution measured with FFD module prototypes was estimated as

~3.5 ps for the E. B. DRS4 V5,

~14 ps for the E. B. DRS4 V4 (it depends on delay used),

~15 ps for the CAEN digitizer,

~20 ps for the TDC32VL and TDC72VHL.

The TDC72VHL modules will be used as readout electronics for the TOF detector and FFD in the MPD experiment.

Two special rooms in Bld. 201 LHEP were rebuilt and equipped for detector production and experimental tests. Experimental studies with deuteron beams of Nuclotron were carried out at beam channels of MPD-test area and BM@N area.

5.2. Tests in laboratory

The test measurements in laboratory were carried out with LED pulses and cosmic rays. A view of the experimental stand with tested FFD modules is shown in Fig. 5-1. Majority of the tests were performed with the E. B. DRS4 digitizers. For the E. B. DRS4 V5 digitizer the time resolution dependence on the delay between pulses was studied with a generator, a laser LED, and variable cable delays. The result is shown in Fig. 5-2. The obtained time resolution of 3 – 4 ps is negligible with respect to the expected time resolution of FFD modules.

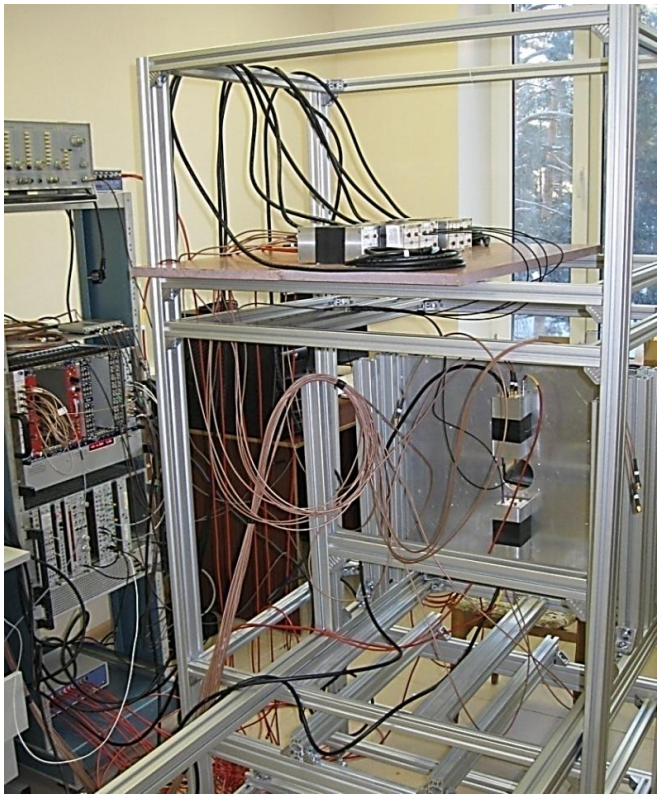

Fig. 5-1. Test of FFD modules in experimental room.

The time resolution of FFD modules was measured with two module prototypes D1 and D2 using analog and LVDS pulses. For this purpose, shot light pulses were produced by a fast LED into a bundle of 1- m optical fibers used for light transport to the detectors. A separate measurement was made to study the influence of cable length on the resolution. The obtained results are shown in Fig. 5-3 as a function of the pulse height. In both cases, analog and LVDS pulses, the time resolution of a single detector becomes better than required 50 ps when the pulse height exceeds 150 – 200 mV due to better statistics of photoelectrons. The measurement

with the LVDS pulses gave a bit worse result in comparison with the result obtained with the analog pulses. No influence of cable length on the result was found.

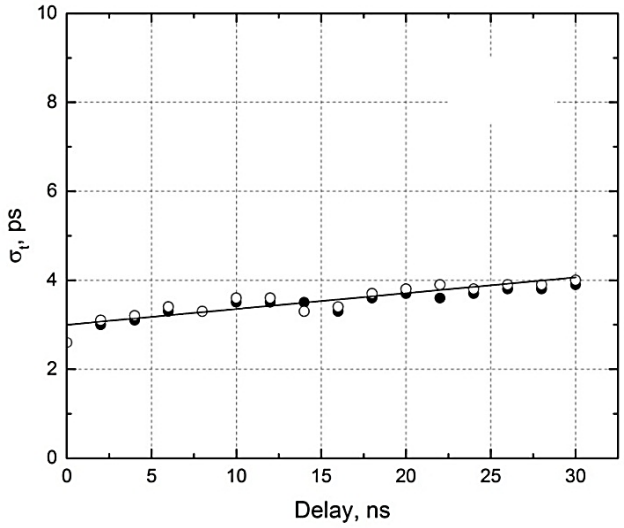

Fig. 5-2. Time resolution of the E. B. DRS4 V5 digitizer as a function of delay.

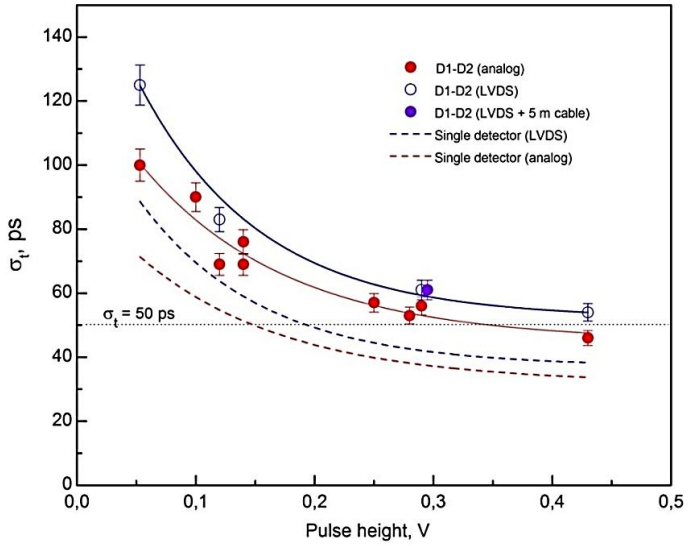

Fig. 5-3. Time resolution measured with LED and module prototypes D1 and D2.

5.3. Beam tests

A study of detector module performance was carried out with external beam of deuterons of the Nuclotron at LHEP/JINR. The energy of deuterons was 3.5 GeV in measurements at "MPD-test" beam channel and 3.5 GeV/nucleon at "BM@N" beam channel.

The number of Cherenkov photons produced in our detector by a high-energy deuteron corresponds to a response for a relativistic single charged particle such as proton or electron. The result of MC simulation for 3- GeV protons is shown in Fig. 5-4. The maximum of distribution corresponds to ~1860 Cherenkov photons and it corresponds to the first peak in Fig. 4-8 showing the pulse height distribution for detected photons in terms of the number of Cherenkov photons. The delta-electrons give an additional contribution and increase the response.

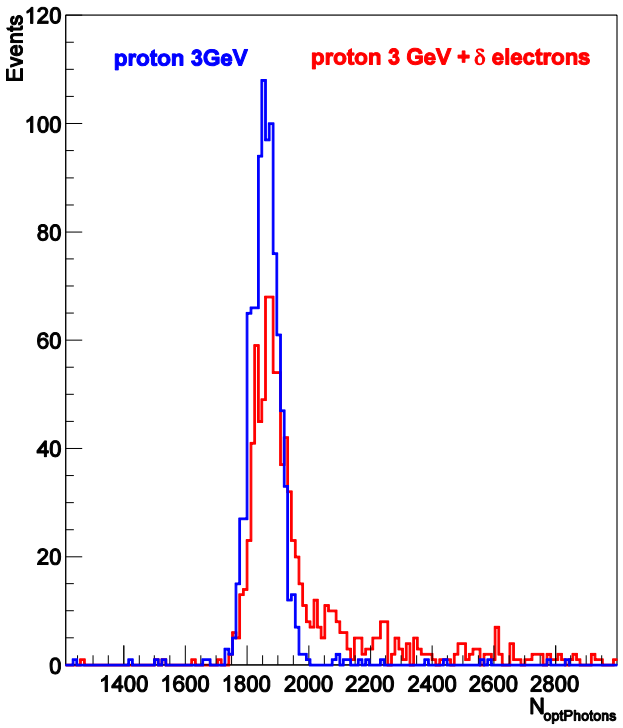

Fig. 5-4. The pulse height distribution for 3- GeV protons in terms of Cherenkov photons produced in the quartz radiator.

In studies at MPD-test beam line, the beam intensity was varied from 10^3 to 10^5 deuterons per 2- s spill. A photo and a scheme of the experimental setup at the beam line are shown in Fig. 5-5 and Fig. 5-6, respectively.

Two pairs of detector modules were installed along the beam axis. The modules did not contain the lead converters. The first pair of modules D1 and D2 were placed behind the first MWPC, the second pair D3 and D4 – at a distance of 2.7 m behind the first pair. RPC prototypes of the TOF detector were located in the middle of the experimental setup. The distance between modules in the pairs was ~22 cm.

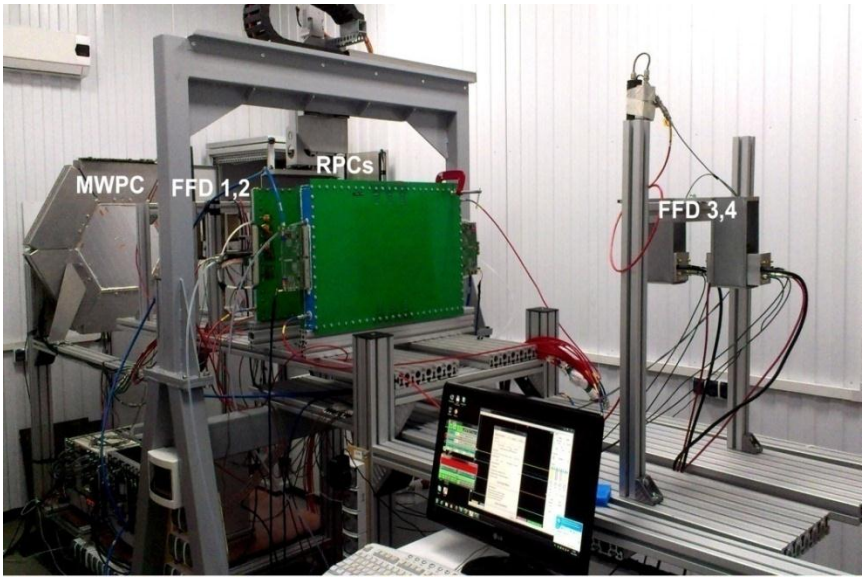

Fig. 5-5. The layout of FFD modules D1 ÷ D4 together with other detectors on the beam line of MPD-test area.

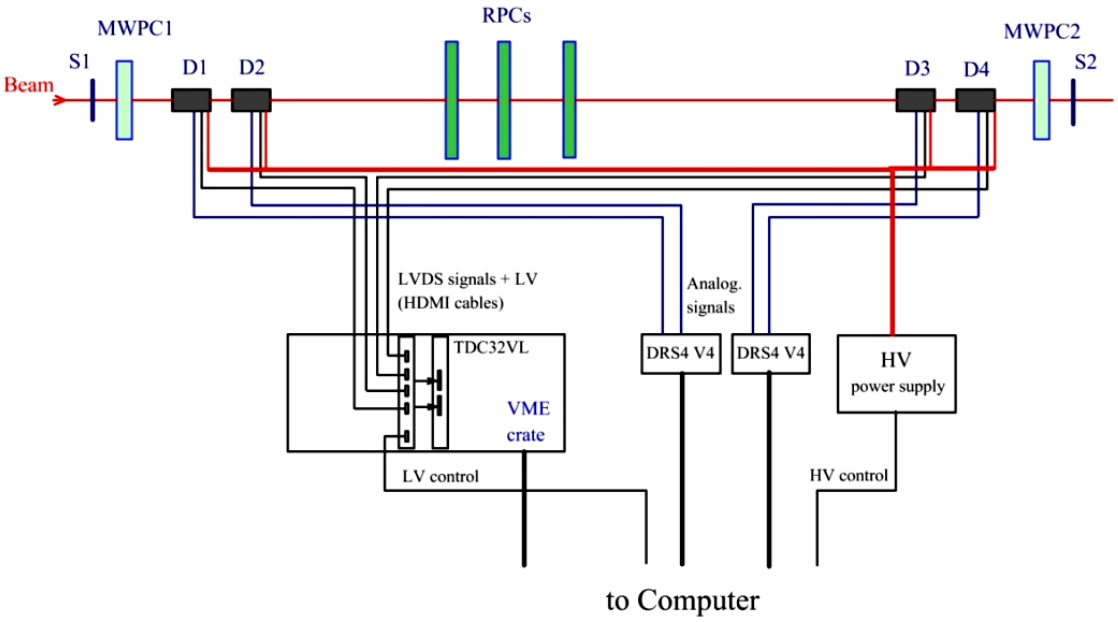

Fig. 5-6. A block-diagram scheme of the experimental setup for study of detector modules: S1, S2 – the scintillation counters, MWPC1, MWPC2 – the multiwire proportional chambers, D1 ÷ D4 – the tested detector modules, RPCs – the resistive plate chambers of TOF detector.

Two scintillation counters S1 and S2 were used for trigger pulse production for each beam particle passing through the experimental area. The information from MWPCs was used for track reconstruction.

The LVDS signals from modules D1 ÷ D4 were fed via HDMI cables to a special board whose aim was (i) production and control of low voltages for FEE, and (ii) transport the LVDS signals to inputs of a VME module TDC32VL. The analog pulses were fed from the modules to two E. B. DRS4 V4 digitizers.

Thus, two different readout methods were applied in the time-of-flight measurements to estimate the time resolution of the Cherenkov detector. In the first approach, used also for the TOF RPC detectors, the LVDS signals were fed to TDC32VL modules. The length of LVDS pulses gives information about the pulse height that is used for the slewing effect correction in off-line analyses. The second method was digitizing the analog pulses. The rise time of the pulses after FEE is ~1.3 ns and it corresponds to six time bins on the front slope of the pulses. This is enough for a good interpolation and finding t_0 position by off-line analysis.

In the measurements with E. B. DRS4 V4 digitizer we studied (i) the form of detector pulses, (ii) the pulse height distribution for beam particles hitting the back surface of module, (iii) the cross talk, and (iv) the time resolution of single detector channel.

Typical responses of the detectors D1 ÷ D4 are shown in Fig. 5-7 for 10 events induced by 3.5- GeV deuterons. Here the deuteron tracks passed through the central area of quartz radiators. The rotation of detector by 180° leads to decreasing the pulse height by a factor of ~3.
Thus, in a real experiment, background particles will mostly give much smaller responses which can be rejected by a discriminator.

The measurements showed a negligible contribution of cross talk between module channels to the detector response.

Results of the TOF measurements with two pairs of FFD modules is shown in Fig. 5-8. A linear fit of the pulse front was used for t_0 finding. The obtained TOF peaks are well approximated by a Gaussian distribution with $\sigma \approx 33.5$ ps.

The uncertainty of the beam velocity gave only a few picosecond spread that is negligible contribution. Taking into account the time jitter of E. B. DRS4 digitizer, one can estimate the time resolution of FFD module itself $\sigma_{mod} \approx 21.5$ ps.

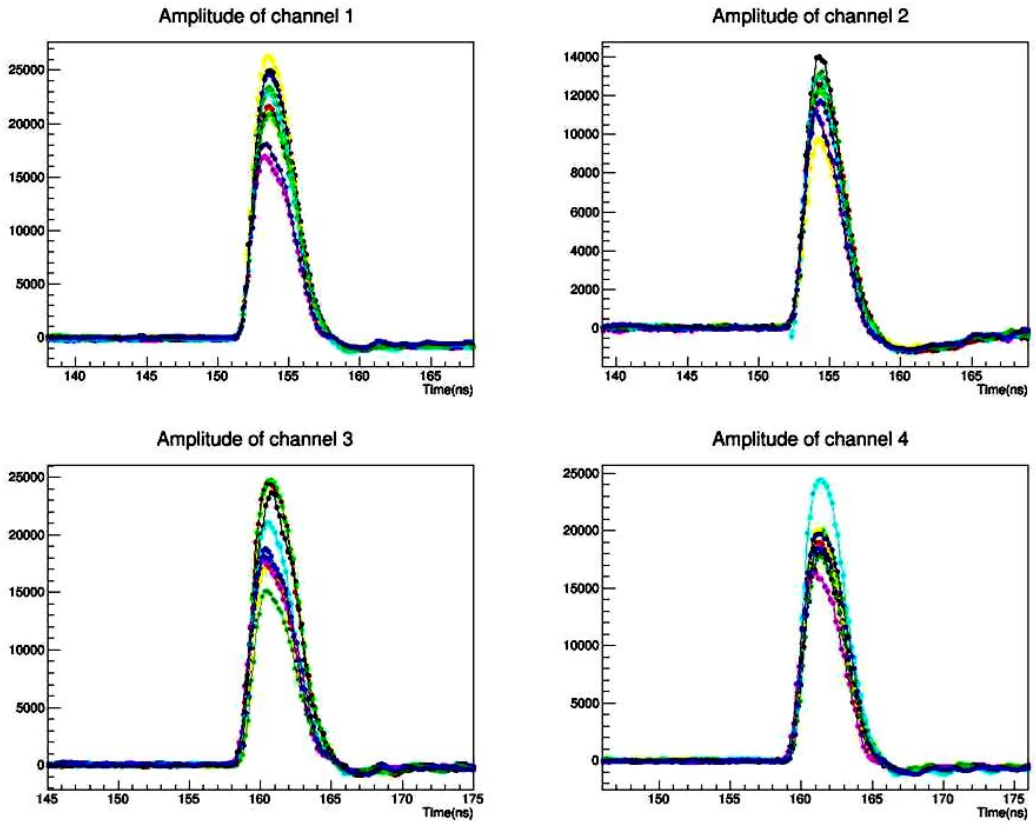

Fig. 5-7. Analog signals of FFD modules for 10 events measured with the E. B. DRS4 V4 digitizer.

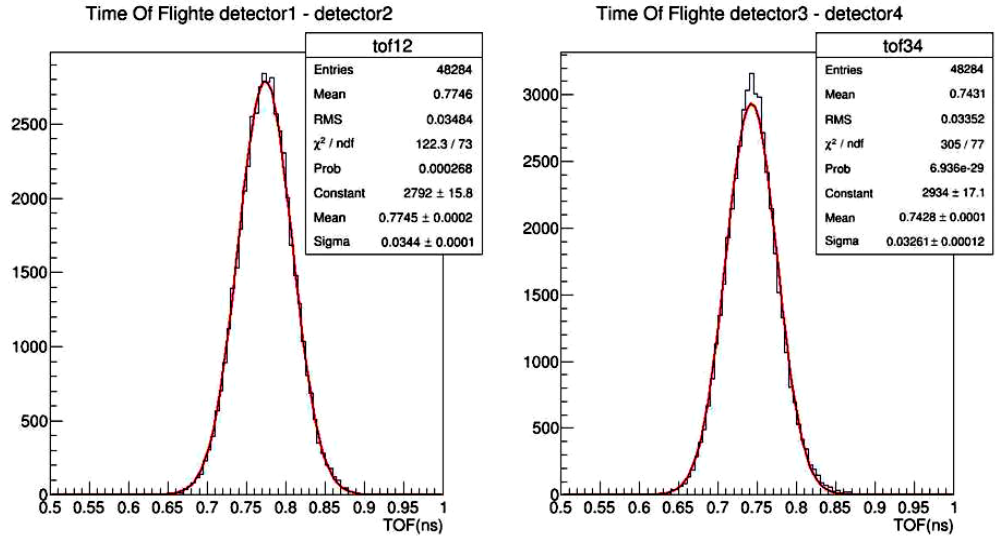

Fig. 5-8. TOF measurements with two pairs of FFD modules and E. B. DRS4 V4 digitizer (run 2014): D1 – D2 (left) and D3 – D4 (right).

Next test was made with pair of modules CD1 and CD2 on the beam line of BM@N setup where TOF measurements with 3.5- GeV/n deuterons and CAEN mod.N6742 digitizer were carried out. The results are shown in Fig. 5-9. The data were obtained for the four individual channels of the modules. The time resolution of a single detector channel with electronics is σ_{FFD} = 33 ÷ 36 ps that is worse than the results earlier obtained with E. B. DRS4 V4 digitizer but it also satisfies the requirement.

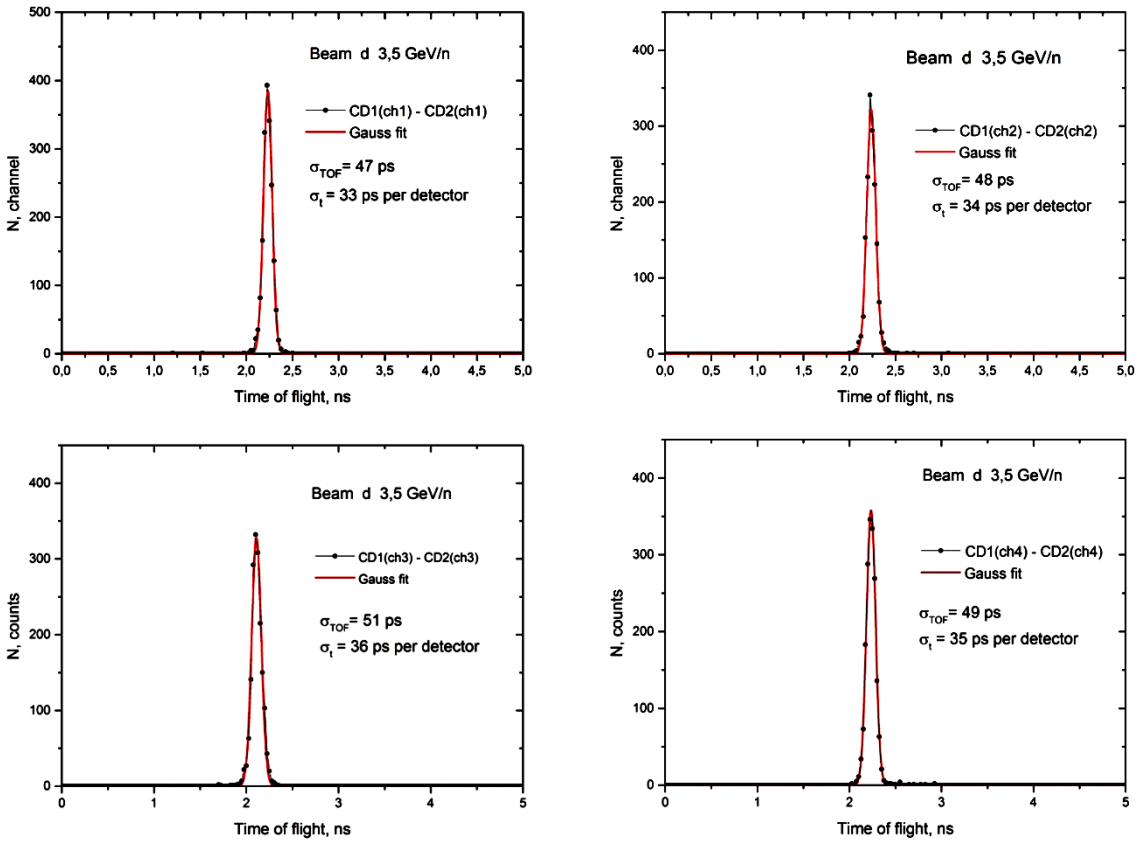

Fig. 5-9. The TOF peaks obtained with pair of modules CD1 and CD2 and the CAEN digitizer in measurement with 3.5- GeV/n deuteron beam.

A more careful study of the detector characteristics and how they depend on the hit position in the quartz radiator was carried out in a special run on the beam line of the MPD-test area with a beam of deuterons. Detectors were equipped with quartz radiators 59 × 59 mm^2 (4 units of 29.5 × 29.5 mm^2 quartz bar) which are equal to the full size of XP85012. The LVDS pulses were fed to TDC32VL. Two MWPC were used for finding track position of each beam particle on the radiators of tested modules. The tracking allowed the study of detector pulses and time resolution for selected virtual cells with size of 7.4 × 7.4 mm^2. A scheme of the quartz bar layout

with a set of 4 × 4 virtual cells used for detector response analysis is shown in Fig. 5-10. The distributions of LVDS pulse length obtained for the different virtual cells are shown in Fig. 5-11. The TOF peaks shown in Fig. 5-12 were obtained as a time interval between pulses in the same cells of the detectors.

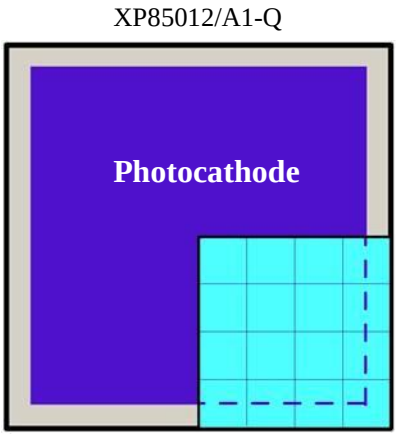

Fig. 5-10. A scheme of 29.5 × 29.5 mm^2 quartz bar layout with a set of 4 × 4 virtual cells.

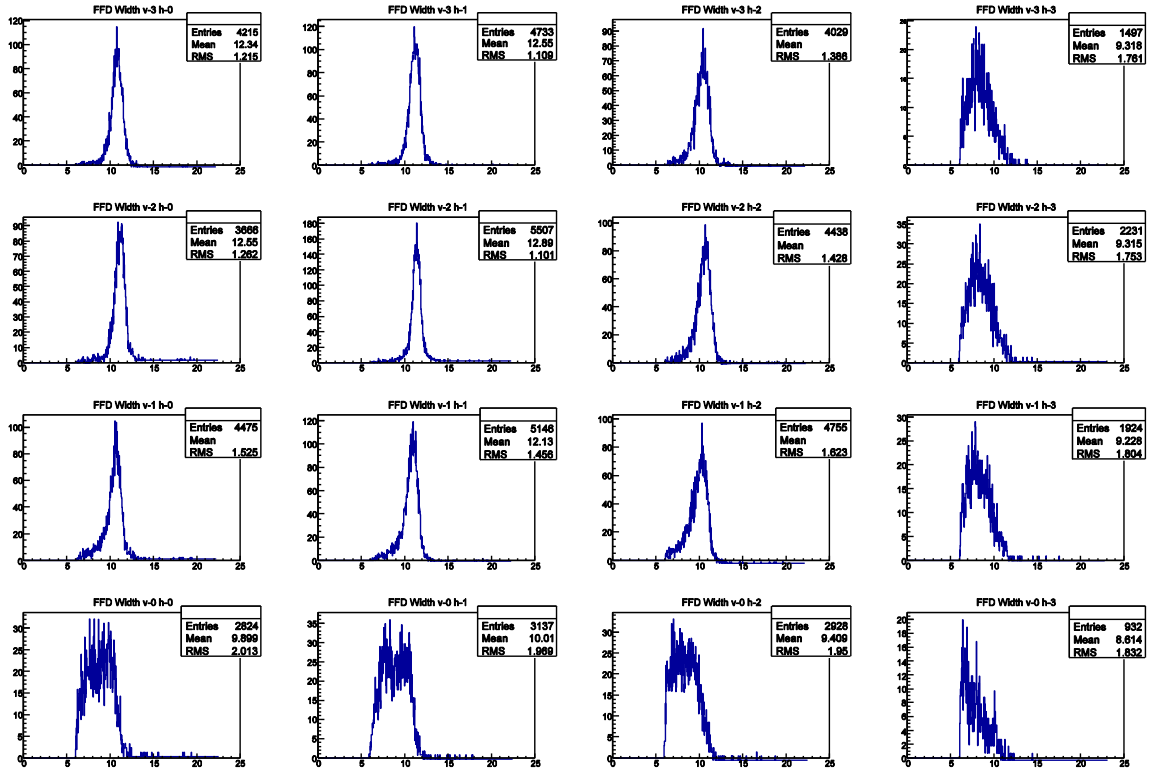

Fig. 5-11. Distributions of LVDS pulse length in different virtual cells of the quartz radiator.

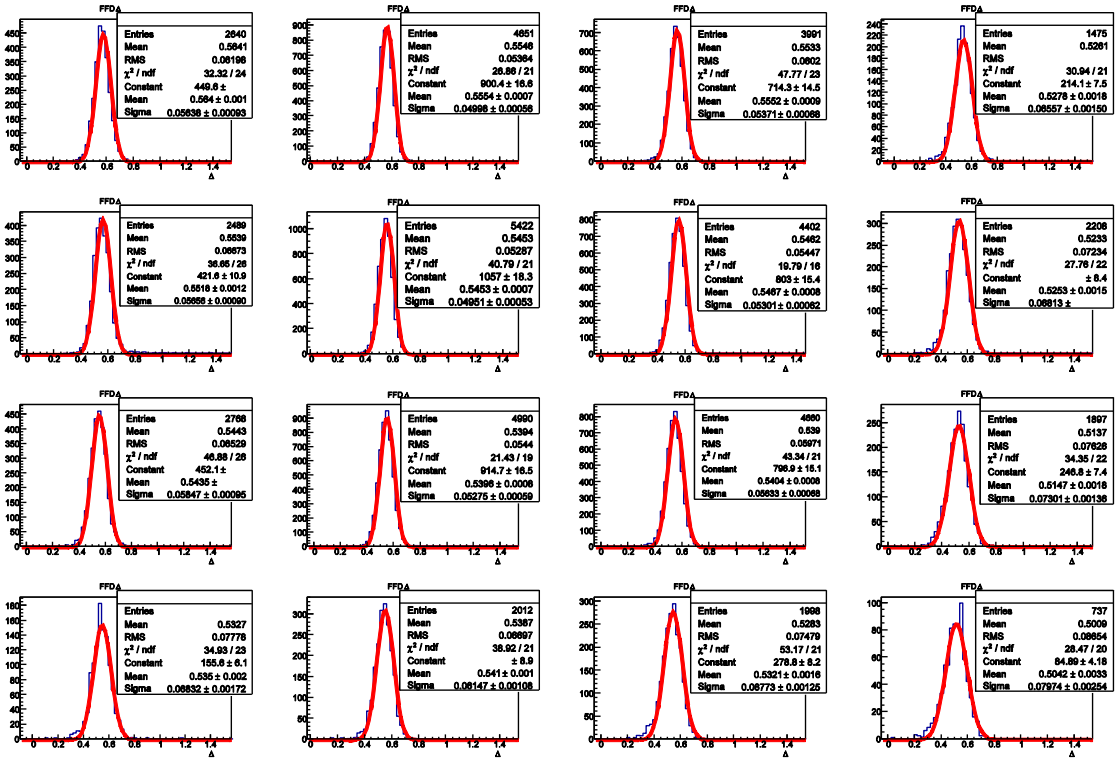

Fig. 5-12. TOF peaks obtained with two detectors for different virtual cells.

The results of the test measurements show a degradation of pulse height (pulse length) and corresponding time resolution in the virtual cells placed along the perimeter of XP85012. The reason of this effect is decreasing of the number of photoelectrons in responses of cells located close to the edge of radiator because these cells lay over the dead area of MCP-PMT and photocathode efficiency decreases over its perimeter. The sigma of TOF peak changes from ~50 ps to ~80 ps in the right-down corner that corresponds to ~35 and ~57 ps for the single channel of FFD module.

Taking into account the results of the test measurements, the final size of the quartz bars of $28 \times 28 \times 15$ mm^3 was chosen. It provides the required time resolution with large active area of FFD module.

5.4. Tests with realistic chain of cables and electronics

Before we discuss the results obtained in test measurements with FFD module prototypes where the analog and LVDS pulses from FEE were directly fed to different readout electronics by means of rather shot cables with length from 2 to 5 m. In this section we describe the experimental study with a realistic chain of cables and electronics expected in the MPD experiment.

The experimental setup with two modules of FFD on MPD-test beam line is shown in Fig. 5-13. The measurement was made with deuteron beam in Dec. 2016. The LVDS pulses of detector modules, on a way to TDC72VHL (DAQ), pass 10- m HDMI cables, sub-detector electronics unit, and 5- m Molex cable. This scheme reproduces real scenario of transport of FFD signals in MPD. The obtained time resolution of the TOF peak shown in Fig. 5-14 is 62.5 ps which corresponds to 44- ps resolution for single individual channel of FFD. This result is close to the value obtained with short cables shown in Fig. 5-12. Thus, no essential influence of cable length and detector electronics on the time resolution was found.

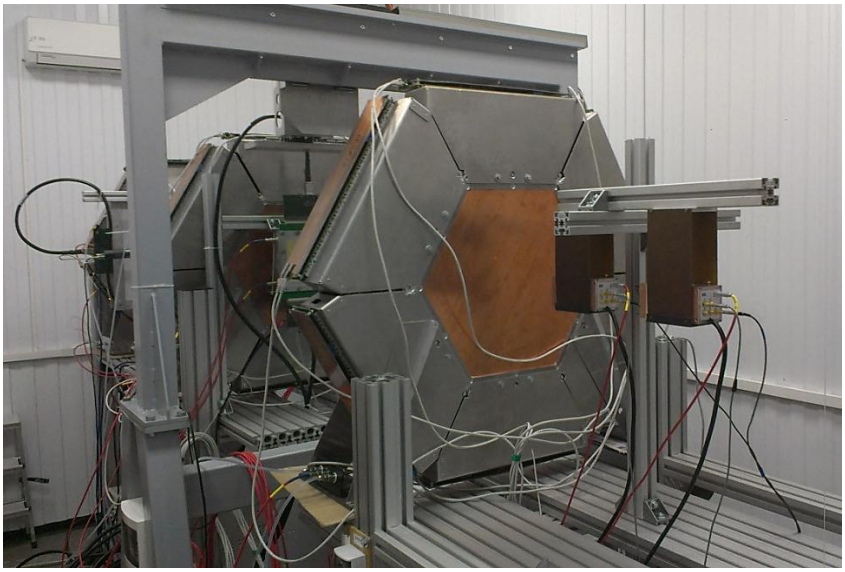

Fig. 5-13. The experimental setup with two modules of FFD on MPD-test beam line.

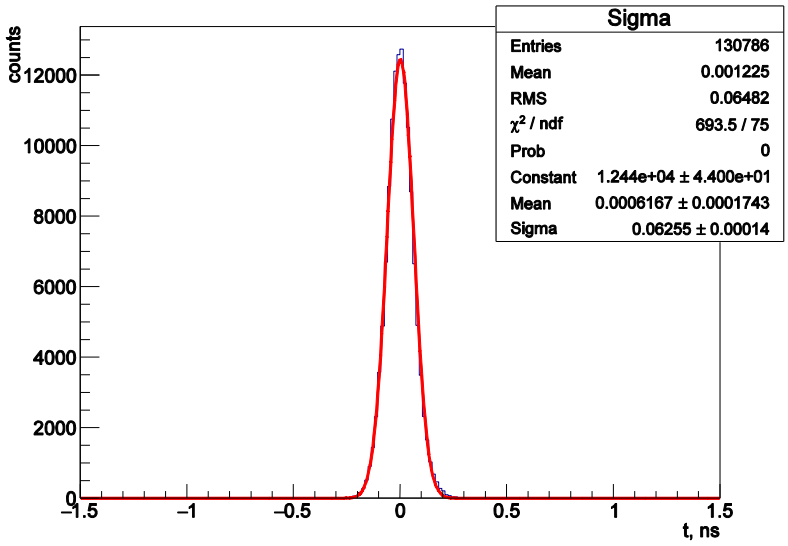

Fig. 5-14. The time resolution of the TOF peak obtained with two FFD modules and realistic chain of cables and electronics.

Thus, the results of experimental studies with FFD prototypes lead us to the conclusion

- the contribution of individual channel of FFD module itself to the time resolution of start signal is $\sigma_{mod} \approx 21.5$ ps,
- the measurements with short cables and different readout electronics gave $\sigma_{FFD} \approx 24$ ps with E. B. DRS4 digitizer, ≈ 34 ps with CAEN mod.N6742 digitizer, and ≈ 44 ps with TDC72VHL used in MPD DAQ,
- the time resolution of individual channel of FFD module with cables and electronics used in MPD is $\sigma_{FFD} \approx 44$ ps and it is better than 50 ps required.

Some results obtained in the test measurements have been reported and published elsewhere in [24 – 30].

5.5. Tests in magnetic field

Operation of FFD modules in magnetic field was studied with the BM@N magnet. The modules were placed inside the BM@N magnet one opposite to the other along the field axis reproducing the FFD location in the MPD. The tests were done with light pulses of laser LED and E. B. DRS4 V5 digitizer was used for readout. Typical shapes of the pulses without and with magnetic field of 0.5 T are shown in Fig. 5-15.

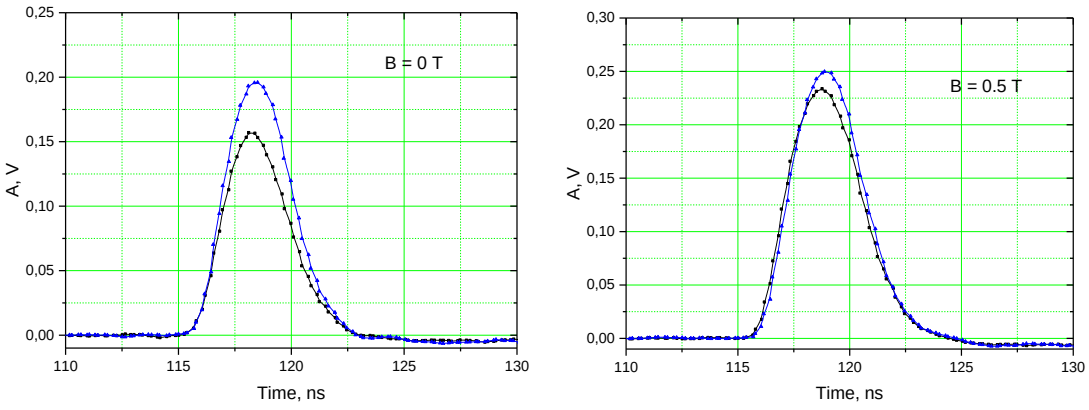

Fig. 5-15. Typical pulse shapes of FFD modules without and with magnetic field of 0.5 T.

Some delay of electron transport through MCP-PMTs of the detectors was observed. It increases with magnetic field but the result does not depend on the detector orientation (on or opposite the field axis) because both the detectors showed the same tendency as it is shown in Fig. 5-16 (a). As a result, the time interval between D1 and D2 pulses does not depend on the

magnetic field as shown in Fig. 5-16 (b). This means that the MPD magnetic field does not affect the time (vertex) measured between pulses of the FFD sub-detectors.

The time resolution in a magnetic field of B = 0.5 T was estimated in TOF measurement with two detectors D1 and D2. The measurement showed that the result slightly improves with the high voltage of MCP-PMTs. For a single detector the time resolution is $\sigma \sim 40 \div 50$ ps for individual channels.

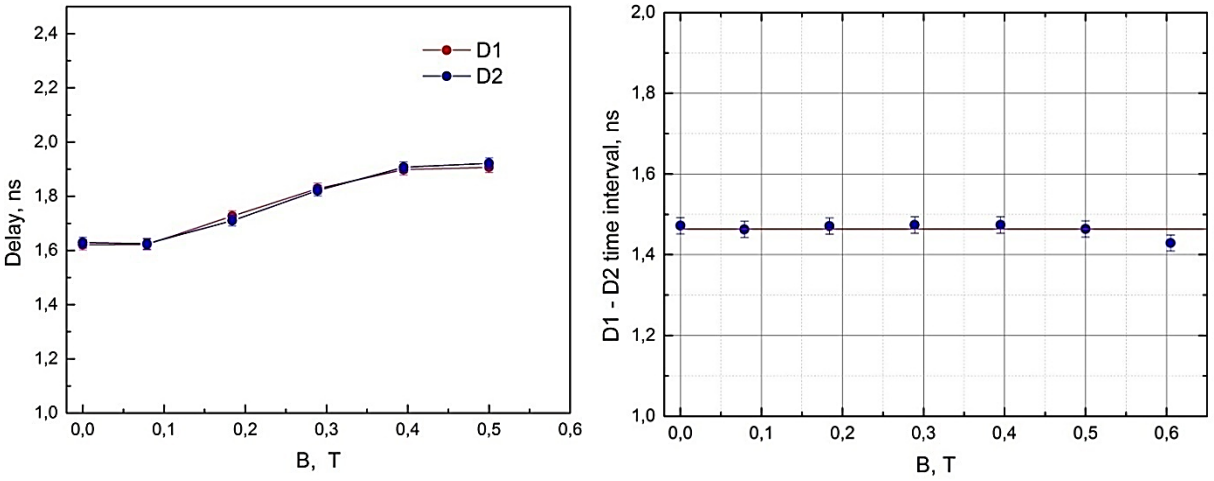

Fig. 5-16. The detector pulse delay (left) and the time interval between D1 and D2 pulses (right) as a function of magnetic field B.

The detector showed good performance in our tests with magnetic field up to B = 0.9 T. But for operation in so high field MCP-PMT requires additional ~100 V of HV magnitude.

5.6. Special stand for tests with cosmic muons

A special stand was created in the laboratory for final test measurements of the FFD modular arrays with all electronics, cables, and the control detector system shown in Fig. 2.4. Aim of the stand is study of FFD performance, adjustment of electronics and sub-systems, development of algorithms of calibration, monitoring, and analysis. In the measurements, the cosmic muons induce the pulses in FFD modules and simultaneously in strips of four scintillation planes used for generation of a trigger pulse and information about the muon trajectories. A scheme of the stand is shown in Fig. 5-17. Each scintillation plane has dimensions 50 × 50 × 1 cm^3 and consists of 10 strips with width of 5 cm. Crossing of the strips of X- and Y- planes on the top and bottom of the stand provides information about direction of incoming cosmic muons. The scintillation light in the strips is detected with two SiPMs 6 × 6

mm^2 (Micro FC-60035-SMT from Sensl) placed on the strip's ends. The pulses are summed and fed to input of FEE amplifier. Production of the scintillation planes is shown in Fig. 5-18. The 10- cm lead layer deletes the soft component of the muons.

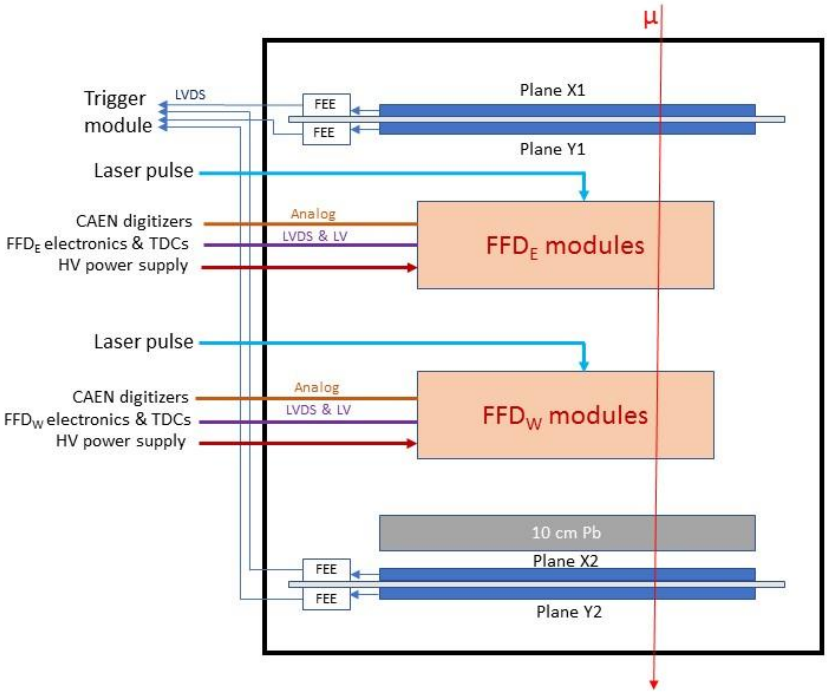

Fig. 5-17. A scheme of the stand for tests with cosmic muons.

Fig. 5-18. Production of the scintillation planes.

6. The FFD electronics

6.1. General description

The electronics of FFD pulses processing consists of three relatively independent parts: East and West branches of Sub-Detector electronics Units (SDU), a Vertex Unit (VU) and L0 trigger module, and readout electronics of MPD DAQ (main) and FFD DAQ (local). The FFD electronics is located in a special rack outside the MPD magnet. The length of cables from FFD array to the electronics is approximately of 8 m.

The SDU consists of a fan-out of LVDS and analog pulses coming from outputs of FFD modules, a counter of the number of fired channels of FFD sub-detector, 20 discriminators with high threshold adjusted by the Detector Control System (DCS), and a pulse processing logic generating a pulse for the VU.

The L0 trigger pulse is generated only if required conditions are met: time interval between sub-detector pulses V_E and V_W is into a selected interval, the number of fired channels in FFD arrays exceeds a threshold settled, a NICA pulse is in coincidence with the FFD pulse.

A functional scheme of the FFD electronics is shown in Fig. 6-1.

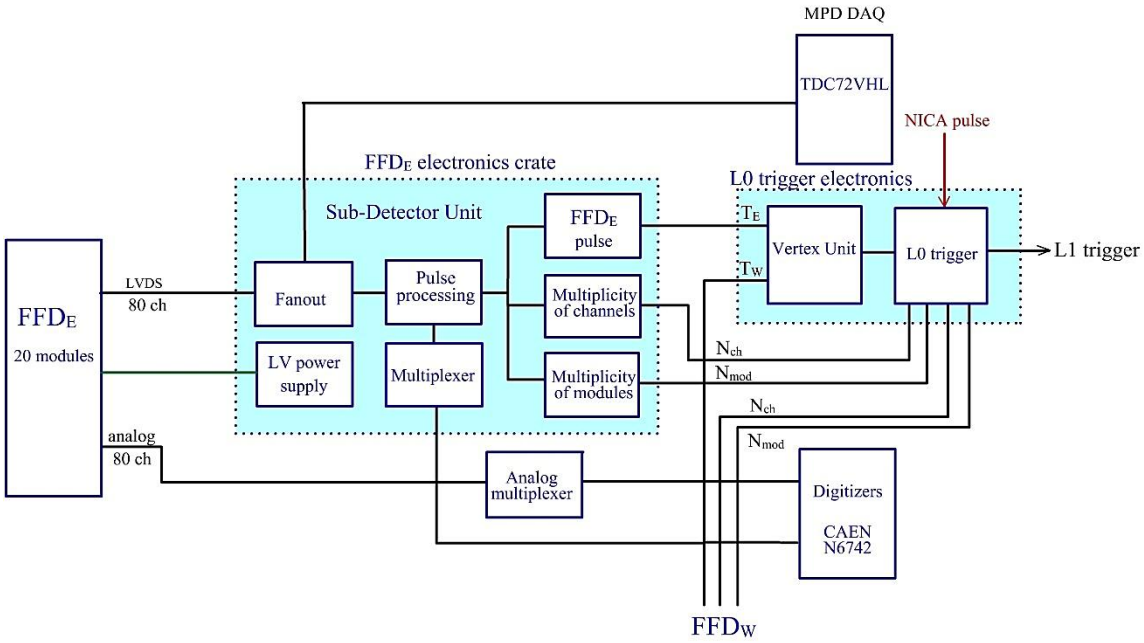

Fig. 6-1. A functional scheme of the FFD electronics.

6.2. Sub-Detector Electronics Unit

The SDU has a modular structure, it contains a set of modules placed in a VME crate having a custom back-plain see fig. 6-2. The SDU is able to handle up to 24 FEE boards. The set of modules includes a LV power supply Module (LVM), a Signal Processing Module (SPM), a Central Processing Module (CPM) and an Interface Module (IM).

To provide fast FPGA configuration file downloading each module containing FPGA is equipped with the FPGA Configuration Loading Module (CLM) connected directly to a serial link interface.

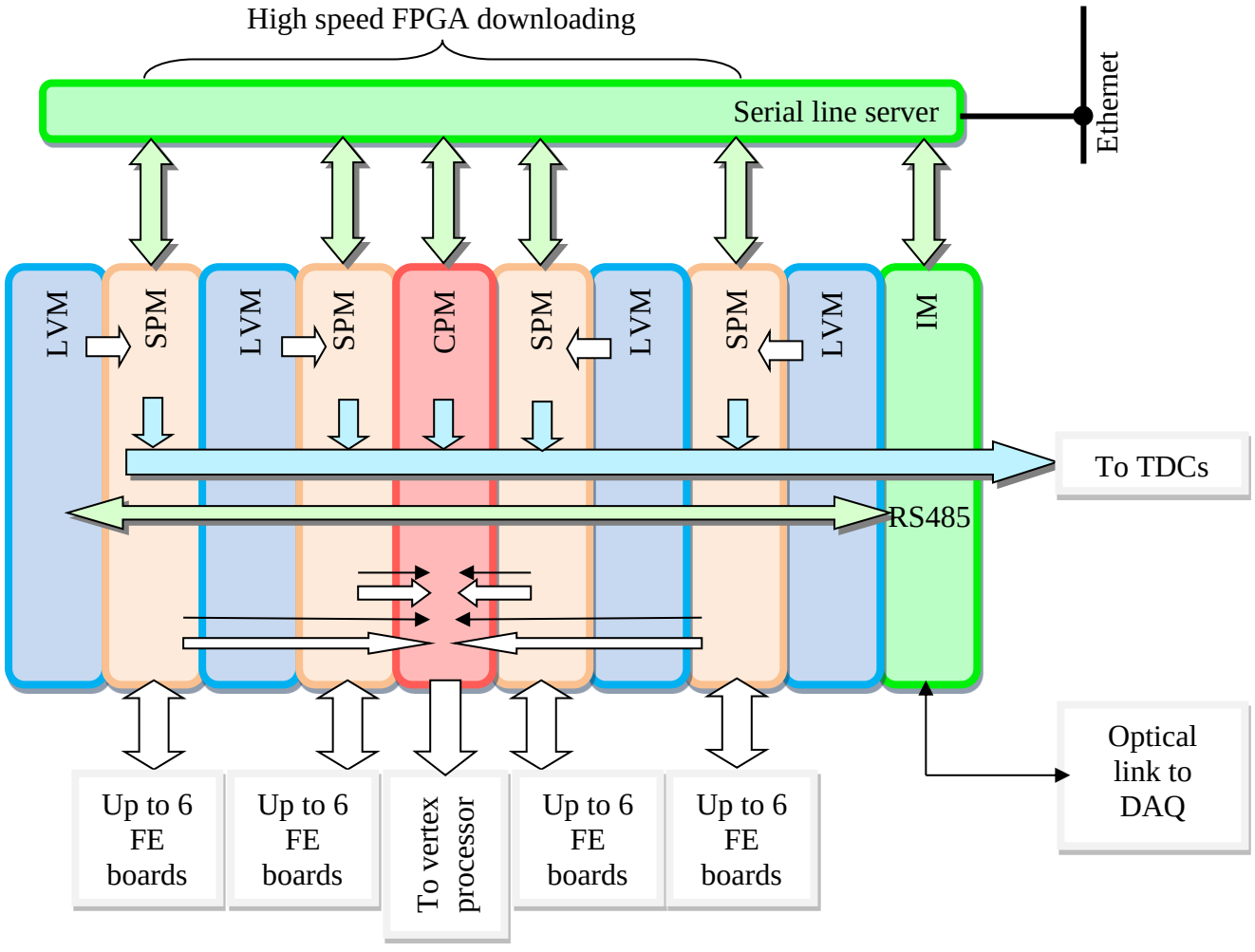

Fig. 6-2. A block-diagram of the SDU.

The backplane contains a parallel bus to control all modules located in the SDU crate using full-duplex multi-drop RS485 serial line and inter-module connections for fast signals and LV power lines between LVM and SPM.

The LVM provides power for 6 FEE boards and contains 6 groups of 3 independent LV power supply channels.

All output power lines go through a back-plane to the corresponding SPM and then go to HDMI connector, see fig. 6-3.

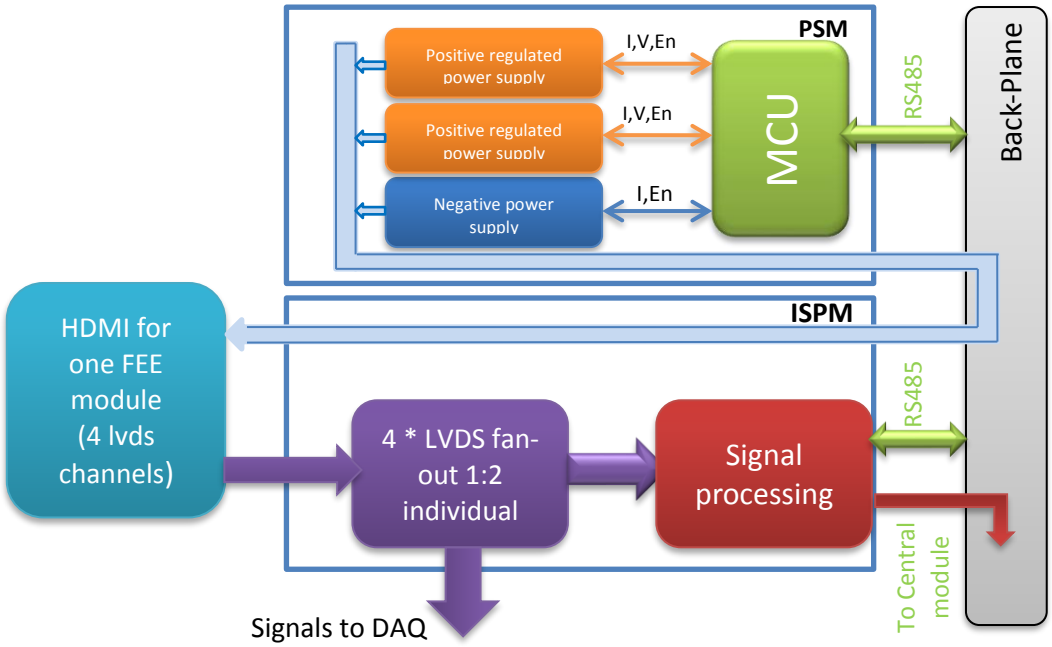

Fig. 6-3. A block-diagram connection of LVM and SPM.

Each LV power channel is monitored and controlled with high precision and could be switched On or Off independently. The Power supply module uses MCU STM32F103 to control LV channels.

The power supply unit technical specifications are as follows:

- the negative voltage channel provides current up to 100 mA at -7.3 V,
- two positive channels provide current up to 150 mA in a voltage range from 4.0 V to 8.0 V and could be adjusted with ~1- mV step,
- the voltage setting is done by 12-bit DACs and reading back of values of output voltages and currents are performed by 12-bit ADCs

The control of LVM MCU and reading back of actual voltage and current values is done via back-plane RS485 serial link.

The SPM receives LVDS signals from up to 6 FEE boards and sends to the Central processing module a number of lighted FFD cell individual signals and a number of lighted FFD modules strobed by the first received pulse with some delay.

The HDMI standard connector has been chosen as a low cost high quality standard industrial solution for signal and power distribution.

The simplified diagram of a SPM is shown in fig. 6-4.

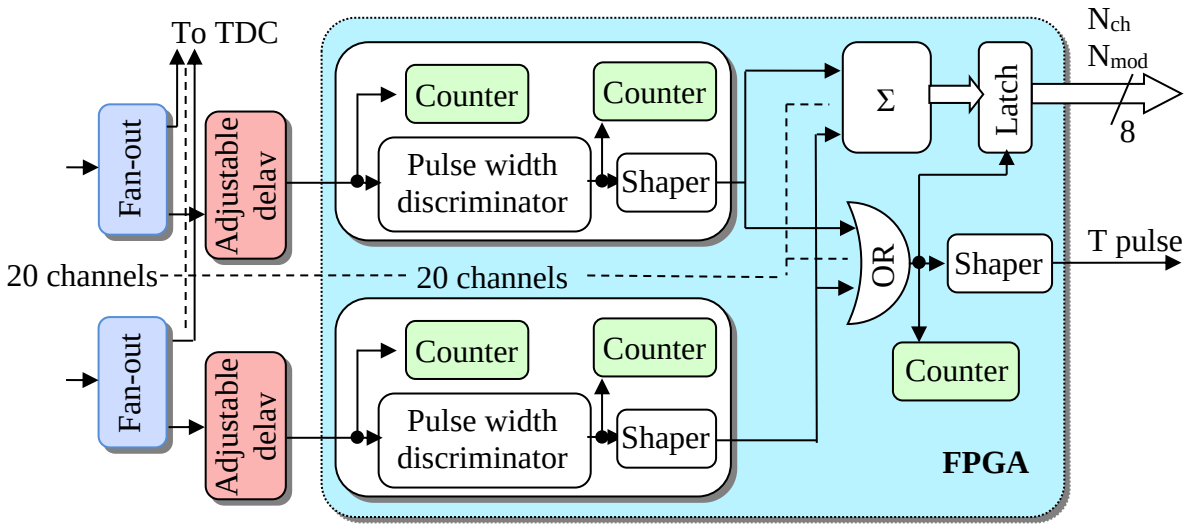

Fig. 6-4. A simplified block-diagram of SPM.

SPM has 20 (plus 4 in reserve) channels and each of them contains following elements:

- a fan-out 1:2 with Micrel chip SY58608U with jitter < 1 ps.
- A precise adjustable delay to align delays in all inputs. The delay value could be set with accuracy 10 picoseconds by a DCS. The delay control board is built as a mezzanine card and contains delays for 4 channels and one microcontroller STM32F103 communicating to DCS by a serial link. The SPM contains 6 delay control boards.
- The pulse width discriminator (PWD) is incorporated in the SPM FPGA. The PWD allows to reject signals with low amplitude and therefore having short signal. This PWD could be adjusted with ~0.7 ns step by the DCS using the serial link. We expect that 5-7 ns rejection time could be good enough to suppress small amplitude pulses.
- Summing unit is used to calculate the multiplicity of signals in individual FEE channels and in FFD modules. The output of this unit is latched by the delayed and shaped fastest input signal generated by ORing of all input individual cell

signals. The values of multiplicities are transmitted as 8-bit parallel code together with the strobe to the SDU Central Processing Module via back-plane.

- Counters are used for FEE monitoring and for the FEE signals alignment. The counters are red-out from FPGA by the serial link.
- All communications between SPM sub-modules like delay board or a signal processing FPGA and the FFD DCS is performed by the RS485 serial link via the crate back-plane.

The SPM is connected to TDC modules via cables with Molex 76105-0585 connectors.

All key points of the SPM FPGA are connected to the output multiplexers inside the FPGA. The output pulses are fed via SMA connectors to coaxial cables transferring the pulses to a scope or CAEN digitizers. This feature is used for the SPM operation monitoring and for the input signal alignment during the FFD adjustment. Multiplexers are controlled by the back-plane serial link.

The CPM collects information from all SPMs of SDU and sends sum number of all lighted sub-detector FFD cells and modules to the Vertex processor and to the L0 Trigger processor via a cable with Molex 76105-0585 connector. The same module is connected to a TDC.

In addition, this module builds multiplicity distribution histograms for SPM modules and counts SPMs strobe signals.

The CPM is also controlled by the via back-plane RS485 serial link.

The Interface Module is used to provide communication between SDU modules and a DCS computer. We plan to use multi-drop RS485 full-duplex serial line with moderate speed of 115200 Bauds. IM has RJ45 connector at the front panel for this link and it is connected to the serial interface with a standard network patch-cord cable.

The IM is able to communicate with DAQ system via optical link to receive commands and reporting its status to DAQ.

In addition, the IM should monitor the crate LV power voltages at the crate back-plane.

The CLM is used to download FPGA configuration "in the flight". Since the SDU is located in a restricted access area the special attention has been applied to provide fast FPGA configuration downloading.

The CLM is built as a mezzanine board with JTAG interface connected to FPGA and RS422/RS485 serial link connected to the DCS computer. The board contains a high-performance microcontroller STM32F405 and a micro-SD card which is used as a local FPGA configuration library, see fig. 6-5.

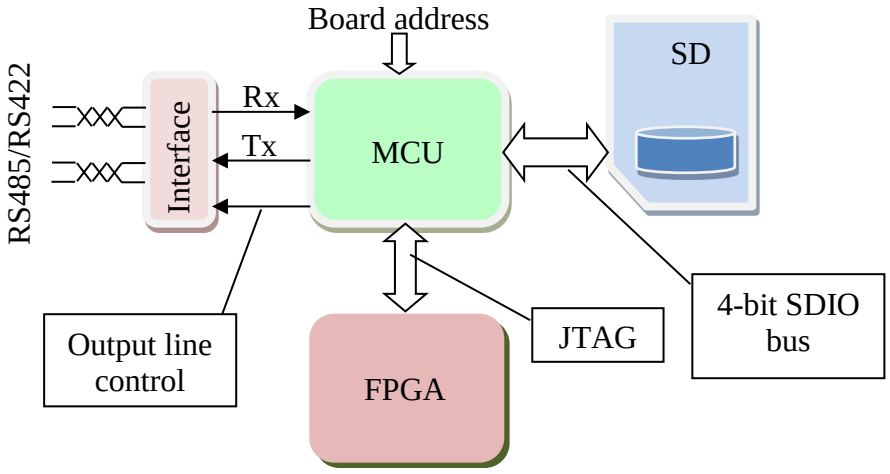

Fig. 6-5. A simplified block-diagram of CLM.

The micro-SD card contains FAT32 file system and the content and a structure of a file system could be browsed by the CLM server at DCS computer. The CLM server is also able to download FPGA configuration files to SD. We plan to use .svf format for FPGA configuration files.

The set of CLMs allows parallel downloading of configuration files to local CLM libraries or directly to FPGA and gives a possibility start parallel configuration downloading from local CLM libraries to corresponding FPGAs by one broadcast command.

To improve configuration loading speed the RS422/RS485 link baud rate is set to 921.6 KBaud.

CLMs are able to run being connected in a daisy chain or having individual lines to a serial interface. Switching of connection mode is done by a switch at the CLM board.

As a Serial Line Server the MOXA NPort 5650-16 module is used. It has 16 selectable RS232, RS485 or RS422 ports and the Ethernet connection to the host computer.

The FFD sub-detector also contains Analog Multiplexer Modules (AMMs) to monitor individual FFD module channel signals. AMMs are built as NIM module and they are located in the NIM crate. Each AMM has 20 input and 5 output SMA connectors at the front panel. The inputs are connected to individual analog channels and output connectors are connected to CAEN digitizer inputs. To transmit selected input to output a 4-to-1 analog multiplexer chip with low open channel resistance is used.

AMM is controlled by a STM32F103 microcontroller. All AMMs are joined together in a daisy chain with multi-drop RS485 serial link connected to the Serial Line Server. The serial line is done using couple of RJ45 connectors situated at the AMM back panel. The AMM number is selected by a switch at the AMM's front panel. The baud rate is set to 115200 Baud. All AMM interconnections are done using a standard network patch-cord.

6.3. Vertex electronics

The FFD is the main detector providing fast identification of nucleus – nucleus collisions in center of the MPD setup by fast vertex analysis of signals generated by the SDUs of FFD_E and FFD_W. Since the beams crossing occurs every ~75 ns, the time needed for vertex analysis and generation of pulse for L0 trigger electronics must be less than 70 ns.

The Vertex Unit (VU) uses preprocessed data coming from the both SDUs (SDU_E, SDU_W).

The VU consists of a Vertex Unit Module (VUM) and an Interface Module located in a VME crate with a custom backplane. During future development the VU could obtain additional modules places in the VU crate.

The VUM performs the following jobs:

- The Vertex processing,
- The generation of pulse for L0 trigger using signals from the SDU_E and SDU_W,
- The control and monitoring of the PiLas picosecond laser calibration system,
- The accumulation of the trigger monitoring information like trigger counts and multiplicity histograms which is sent to the VU server running at the DCS PC by RS422 serial link

To provide connection between VU and other MPD systems the VUM has a set of mezzanine cards providing connectors at the front and back planes.

The set of VU mezzanine cards includes:

- 50-Ohm TTL – LVDS converter cards,
- LVDS buffers.
- 50-Ohm TTL out board,
- Ethernet interface board,
- Optical link board

A block diagram of the VU is shown in Fig. 6-6.

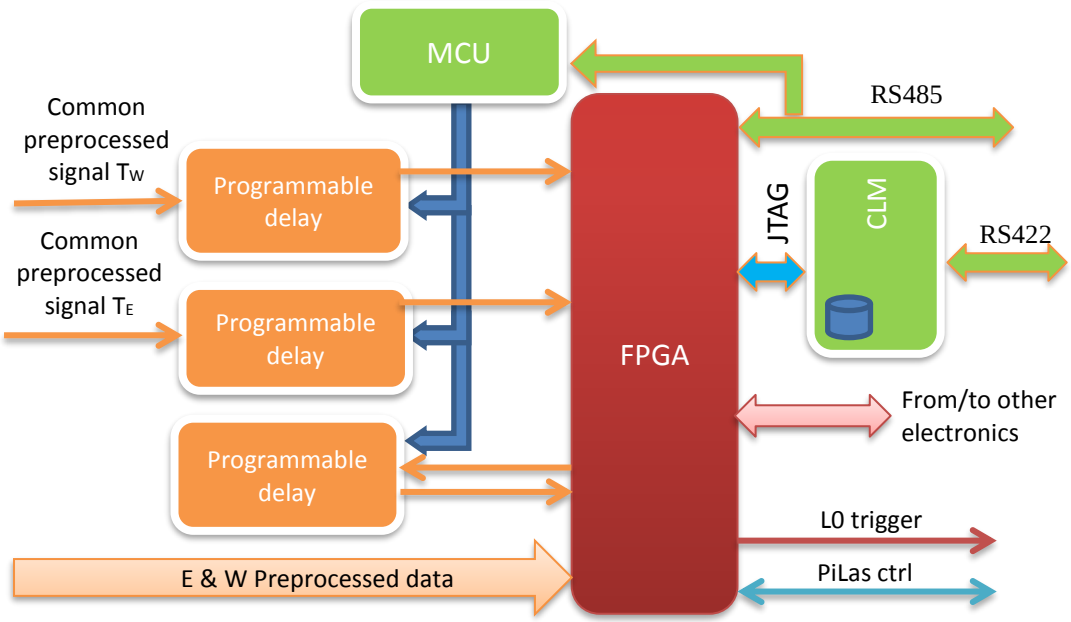

Fig. 6-6. A Block-diagram of the VUM.

Preprocessed common signal from each SDU passes programmable delay controlled by DCS via FPGA. It has a programmable delay chip IC SY89295 or IC854S296I-33 (the same chip is used in SDU) which provides quite stable adjustable delay in a range from 3.2 to 14.8 ns with 10- ps step and a small time jitter.

The vertex processor is shown in Fig. 6-7. The length of cable coming from the FFD_W side is as short as possible and its signal arrives to VU before the signal of FFD_E side. The pulse of the right branch is used as the start signal for vertex coordinate processing and it generates the "Vertex gate signal". The arrival of the left branch signal during the "Vertex gate signal" means that the interaction takes place inside an acceptable range in the center of MPD setup. The geometrical boundaries of the acceptable interaction area are selected and tuned by the adjustable delays of the first branch signal and gate length.

The VU FPGAs are equipped with the CLM providing fast FPGA configuration loading. CLM is connected to a Serial line server with RS422 high speed line.

The control of delay lines is done with STM32F103 MCU.

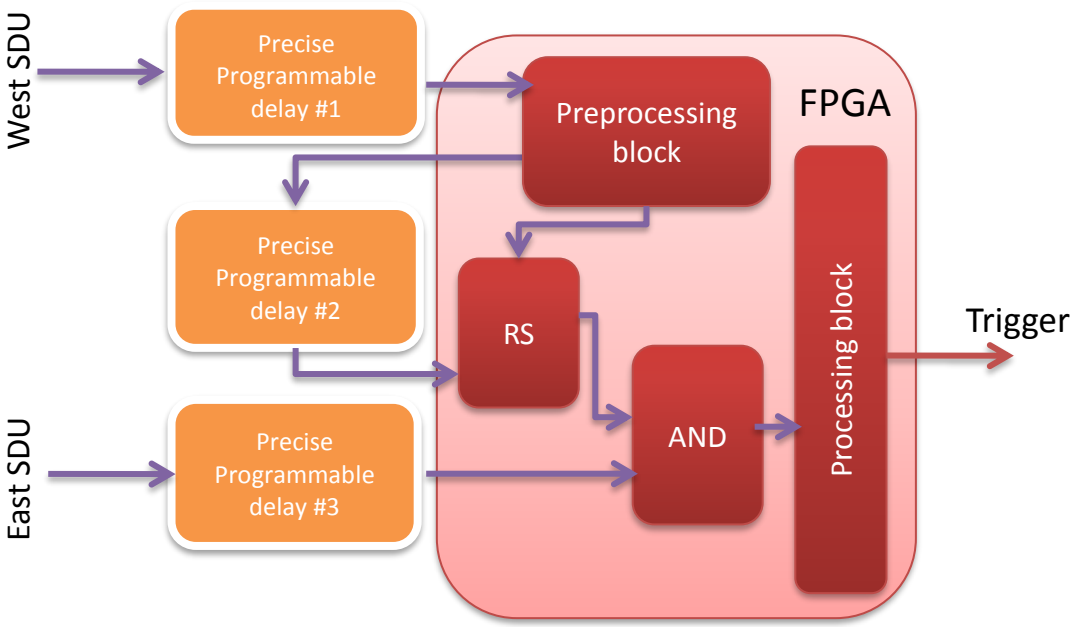

Fig. 6-7. A Block-diagram of the vertex finding logic.

6.4. Readout electronics

The main readout electronics of FFD and TOF detectors is based on TDC72VHL (25 ps multi-hit time stamping TDC developed and produced in Laboratory of high energy physics, JINR). Each FFD sub-detector has 80 LVDS lines plus 2 lines for calibration purpose and it requires two the TDC modules fixed in a nearest VME crate. The LVDS pulses are fed to TDC inputs using cables Molex P/N 11102512xx with connectors Molex 76105-0585.

The FFD local DAQ, which scheme is shown in Fig. 6-8, is based on 5- GS/s 16-inputs digitizers, CAEN mod. N6742, shown in Fig. 6-9. Four these modules are required for adjustment and control of the detector modules and electronics. For this purpose, three different pulses of each FFD module are fed to digitizer inputs: common analog pulse, common logical pulse (NIM), and analog pulse from one of four individual FEE channels. The digitizer modules are fixed in a NIM crate located in rack of sub-detector electronics.

The length of signal cables from FFD modules to the readout electronics is 8 m.

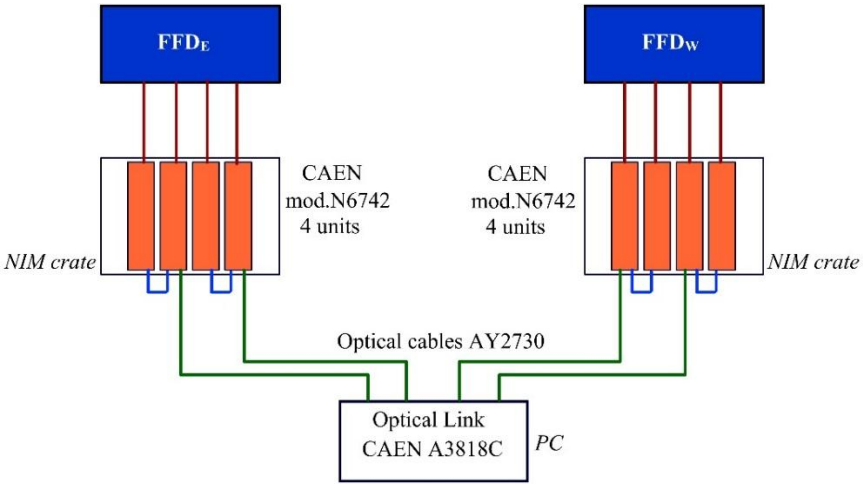

Fig. 6-8. A scheme of FFD local DAQ for control of FFD operation.

Fig. 6-9. A view of CAEN mod. N6742 digitizer.

7. High voltage power supply

To provide HV power to the MCP-PMTs of FFD modules, a high voltage system produced by ISEG and WIENER companies (Germany) is used. It consists of three 16- channel modules with multiple floating ground and controller module from ISEG which are fixed in Mpod mini crate from WIENER. Photos of HV module and Mpod mini crate with two HV modules and controller are shown in Fig. 7-1.

Fig. 7-1. A view of the 16- channel HV module and HV crate with 2 modules and controller.

The HV module characteristics are

- HV range up to -3 kV,
- Current up to 3 mA,
- Low ripple and noise,
- Voltage and current control per channel,
- Hardware current and voltage limits per module,
- Programmable trip parameter,
- 24 bit ADC and 16-20 bit DAC.

Main features of the Mpod mini crate with the integrated Mpod controller card are

- 19" x 5U mini bin with module cage for 4 HV modules, with built-in low noise primary power supply and super-blower ventilation fan,
- MPOD controller with Ethernet, USB and CAN-bus interface,
- 4 slots for HV modules,
- built in primary power supply (600W), low noise and ripple,
- integrated cooling fan,
- Mpod controller card with Ethernet 10/100, CAN-bus and USB-2 interfaces, Interlock connector, optional with ISEG CC24 controller (linux OS with iCS web service, EPIC's IOC, OPC and SNMP).

The HV system is controlled by the FFD Detector Control System (DCS) described in Chapter 8. The central DCS will be allowed only to switch ON/OFF all channels simultaneously and to select and download existing predefined HV configuration from the local repository. The actual values of voltages, currents etc. will be published to central DCS by retrieving data from low-level server.

8. Detector control system

8.1. General functions

The Detector Control System (DCS) provides the control and monitoring of

- the HV power supplies for MPC-PMTs,
- the LV power supplies for frond-end electronics,
- the FFD module operation,
- the SDUs and VU logic operation,
- the laser calibration,
- the local DAQ for calibration and monitoring of the FFD.

8.2. Concept

Each subsystem has its own low level server handling communication between a control PC and a subsystem. The server also provides GUIs for subsystem state presentation and for the expert level control and monitoring of subsystem.

The relevant server information is published by each server in a shared memory as a text having JSON structure. The information update is followed by triggering of "Named event". This information is taken by a FFD DCS server and passed to the DCS tree of whole detector. The general interest information archiving is provided by the central DCS system. Servers also could provide archiving of private information to local files at the DCS PC.

Some fraction of the information could be published by a private web-server running at the DCS PC.

The general FFD DCS scheme is shown in Fig. 8-1.

The FFD experts could have full control of all systems and MPD shifters should have limited control on subsystems. Shifters will be able to switch On/Off channels and select and download predefined configurations of subsystem parameters.

Configurations files are generated by experts using server GUIs. These files are stored as local files and could be only read-out by the MPD DCS server for publishing and archiving.

The subsystem DCS servers publish all relevant information for the FFD DCS server and receive limited set of commands from the FFD DCS server.

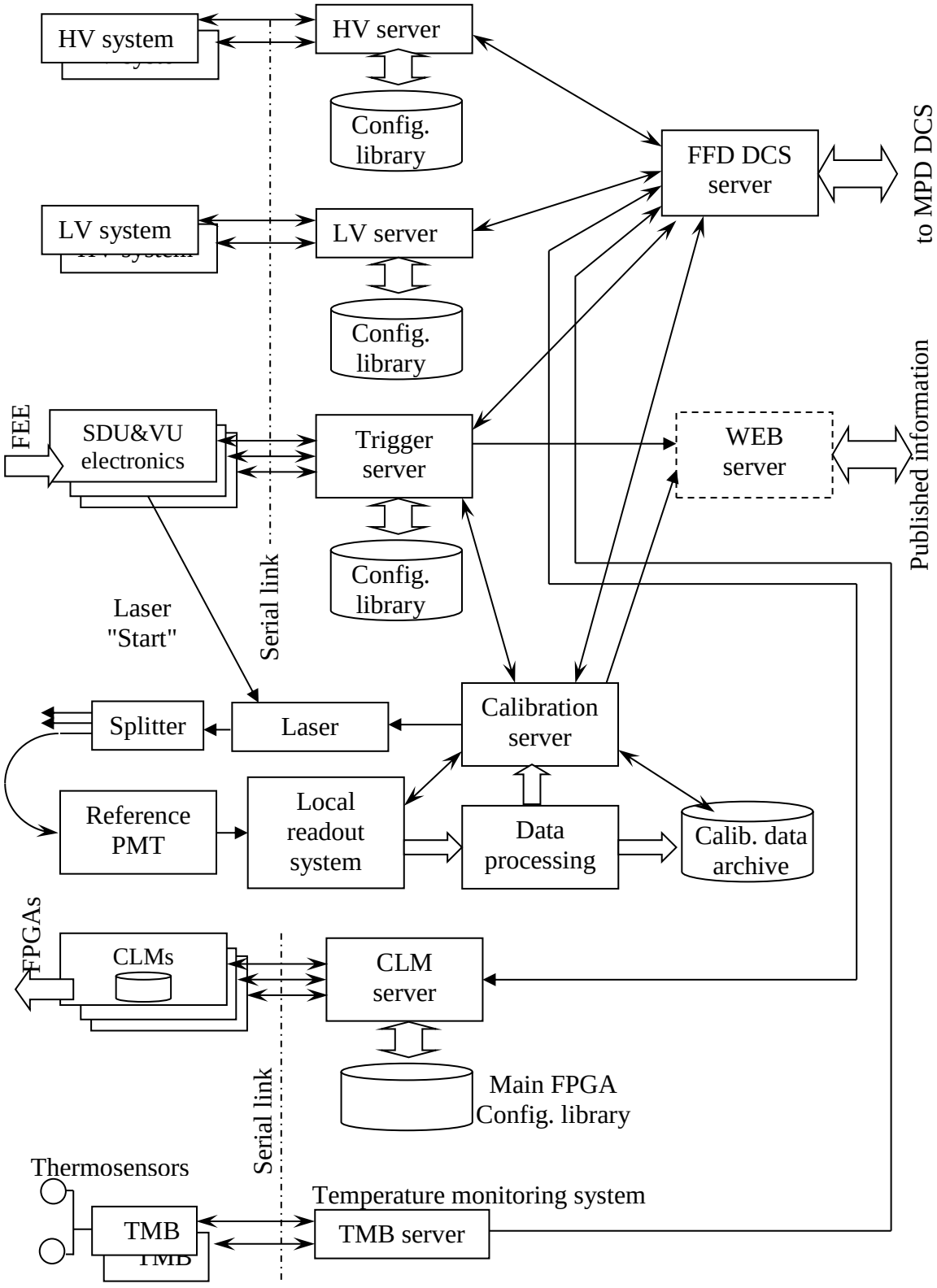

Fig. 8-1. The diagram of the FFD DCS.

8.3. Electronics and software

The DCS PC runs Windows as operation system. The servers are written using Delphi and MS VS development platforms.

The prototype of the FFD DCS web-server has been developed and tested. To provide data presentation in a real-time mode we use AJAX technology. We expect that our single server will be able to provide connection to tens of http clients.

To provide a stable work of servers the "Watch Dog" Windows service program has been developed. This service checks presence of all servers in a PC memory and if a server process is missing then the service restarts the server.

The electronics of DCS has been described above.

A serial link (RS232, RS422 or RS485) or Ethernet-based TCP/IP protocol is used as the main communication protocol. A WizNet W5300 chip which has been tested with a prototype board is used as the TCP/IP node hardware.

We got a communication speed up to 3.5 Mbytes/s at a point-to-point connection.

Microcontrollers of STM32F and STM8L families from ST Microelectronics are used as the base microcontroller in self-made boards.

8.4. Interaction with slow control system of MPD

The FFD DCS is a self-consistent system and it will not have any internal partitioning. It could be partitioned only at FFD/MPD interface.

The states of FFD FSM will follow standard MPD scheme. FFD DCS will publish some fraction of internal information to MPD DCS and it will receive a limited set of commands from MPD DCS including commands to switch On or Off power supply channels and commands to download predefined named configuration to a subsystem. Used channels of FE, LV or HV should be defined inside the configuration file.

Shifters will have a possibility to switch off tripped channels and to suppress error messages from blocked channels to continue.

9. Calibration system

A special method for precision time calibration of FFD channels and monitoring the detector operation is required. For this purpose, we developed a system based on PiLas laser with 30-ps pulse width and 405- nm wavelength. The laser and optical system focused the laser beam on the end of a fiber bundle were produced and delivered by Advanced Laser Diode Systems (Germany). Main parts of the system are

1. the PiLas control unit,
2. the box with laser head and optical system,
3. the quartz fiber bundles,
4. the reference photodetector.

The optical system was specially designed for our application. By means of this system the laser beam is input into quartz fibers with a low loss of the beam power and good uniformity over the fibers. Total number of the fibers is 130 units. They are split in three bundles, two equal bundles with 60 fibers and length of 7.5 m and one short bundle with 10 fibers. The long bundles are coming to patch panels of the FFD sub-detectors and then only 20 fibers with minimal scattering of pulse amplitudes are used for transferring the laser pulses to the sub-detector modules by means of optical cables. The connectors at the ends of optical cables are fixed in center of front surfaces of the module housings (see Fig. 4-1) and by this way the laser pulses simultaneously illuminate all four quartz bars with light spot of ~10 mm in diameter. For this purpose, the lead converters have special hales in the center. The fiber bundles and optical cables were manufactured by CeramOptec Co. using multimode optical fibers WF100/140/300N, NA 0.22. The test carried out with 15- m fiber and PiLas laser showed that the width of pulse increased from 45 ps to 90 ps (FWHM) after passing the fiber. The length of our optical lines is 18.5 m.

A photodetector MCP-PMT PP0365G from Photonis is used as the reference detector.

The characteristics of this photodetector are

- MCP double, chevron, with 6- μm pore size,
- quartz window,
- photocathode diam.: 17.5 mm,
- rise time: 200 ps,
- sensitivity in UV range, QE: ≈ 25–30 %,
- typical gain: 7×10^5.

A view of these elements (besides the optical fiber bundles) is shown in Fig. 9-1.

A scheme of the calibration system is shown in Fig. 9-2. The laser beam is focused on fused end of optical fiber bundle which is split into two branches transported the beam to the quartz radiators of modules of both sub-detectors FFD_E and FFD_W. Additionally, some short fibers are used for reference detectors.

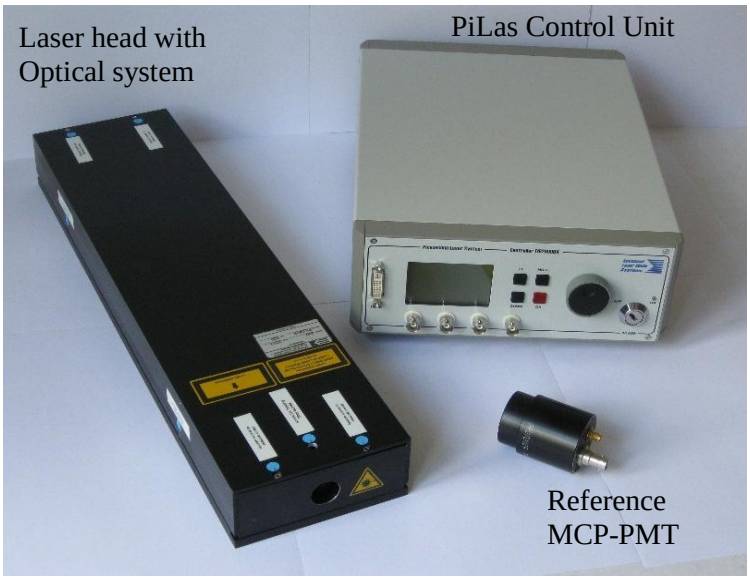

Fig. 9-1. A view of the PiLas control unit, the box with laser head and optical system, and the photodetector MCP-PMT PP0365G.

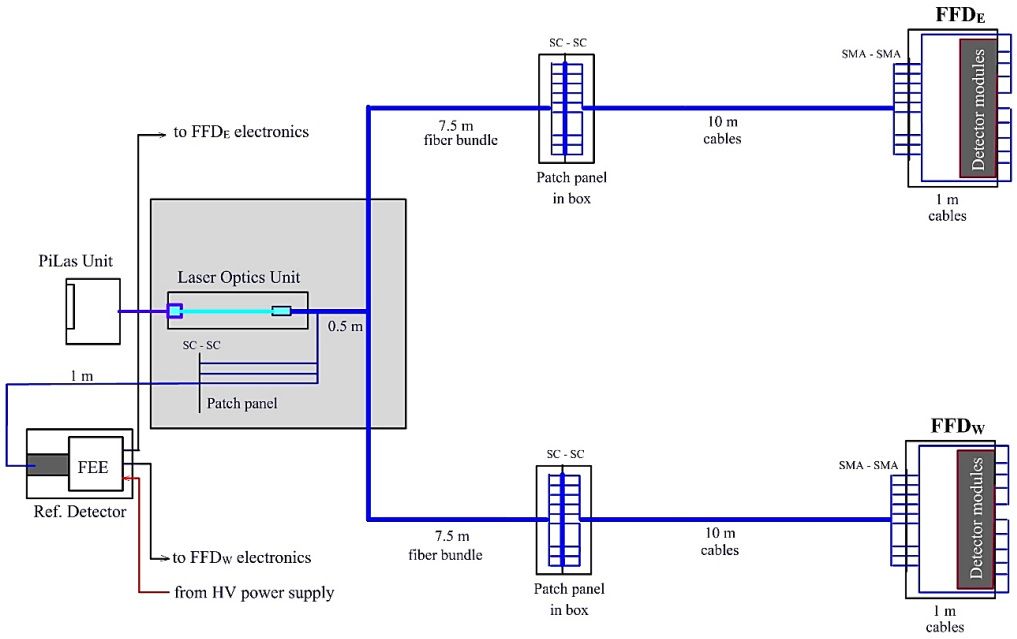

Fig. 9-2. A scheme of the calibration system with PiLas laser.

Distributions of pulse amplitude over 60 fiber outputs in the West and East bundles as ratio to the mean magnitude are shown in Fig. 9-3. The measurement was made with a reference detector. The red and green lines mark 10 and 20 % displacements from the mean magnitudes. It is clearly seen that 20 units with scattering within ~10% interval can be found for both the bundles.

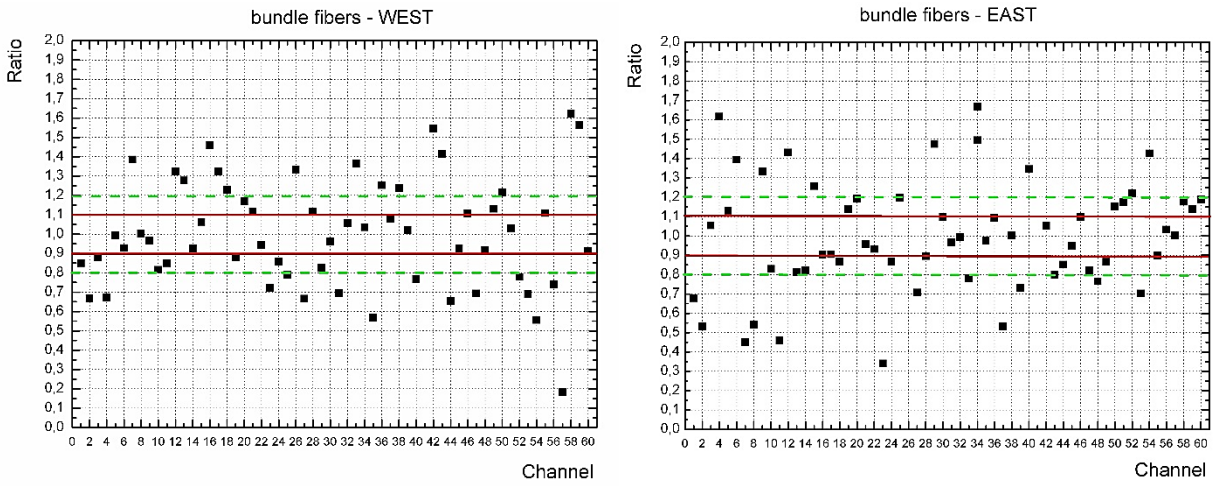

Fig. 9-3. Distributions of pulse amplitudes over fiber outputs in the West and East bundles as ratio to the mean magnitudes.

The module response with laser pulse was studied for three different cases:

- laser pulse in center of the first quartz bar Q1,
- laser pulse in centers of two quartz bars Q1 and Q2,
- laser pulse in center of module (center corners of bars Q1 – Q4).

All these cases are shown in Fig. 9-4. The distance from fiber end and the quartz radiator is 19 mm and total thickness of quartz in front of the photocathode is 17 mm. The light spots on the photocathode for these three cases are shown as blue circles with radius of 6.7 mm that is close to anode pad size of XP85012.

The pulse shapes measured with a digitizer CAEN mod. N6742 are shown in Fig. 9-5. For the last case, the pulse was normalized on a pulse height. The first two measurements gave equal pulse shapes, the third measurement gave similar rise time of the pulse but a bit shorter its width because a pulse width in applied FEE electronics increases with a pulse height.

The time resolution obtained with Q1 and Q2 pulses was 40 ps (sigma) or 28 ps per channel.

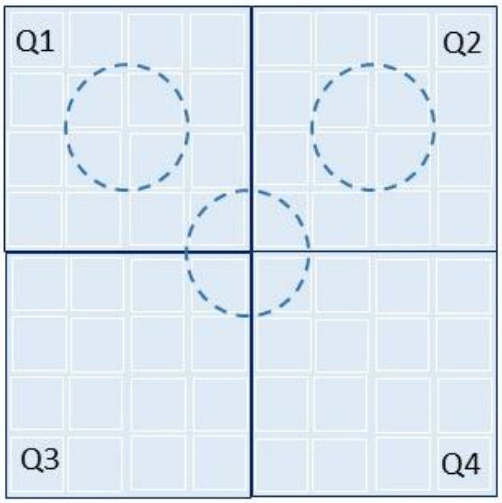

Fig. 9-4. A scheme of laser spots on XP85012 photocathode (blue circles) for three cases of optical fiber inputs.

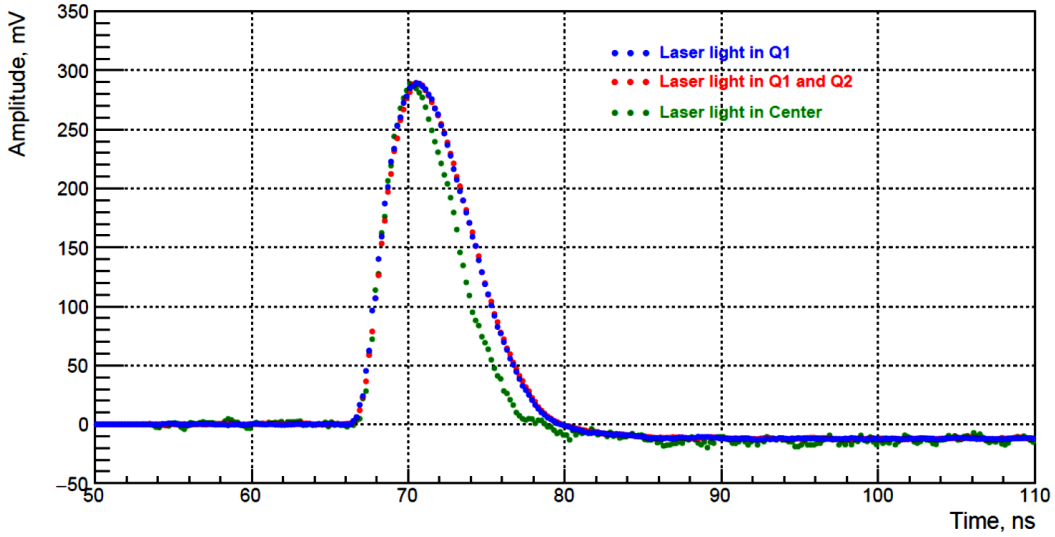

Fig. 9-5. The pulse shapes measured with laser for three cases of optical fiber inputs.

The cross-talk responses in the channels Q2 – Q4 with laser pulse in center of the quartz bar Q1 are shown in Fig. 9-6. Pulse heights of the responses are less of a few mV and these magnitudes are negligible in comparison with 300 mV pulse of the Q1 channel.

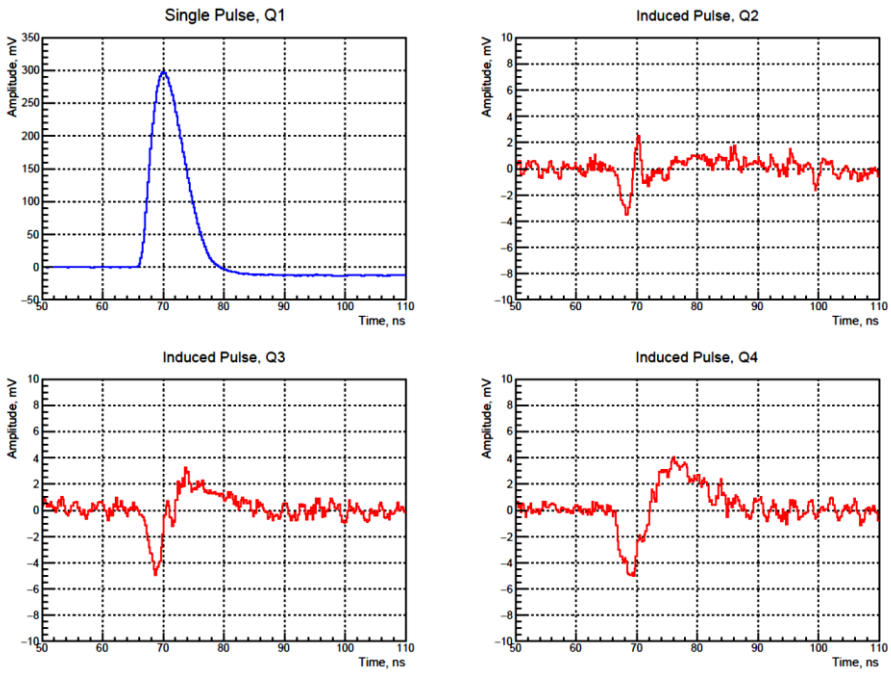

Fig. 9-6. The cross-talk responses in the channels Q2 – Q4 with laser pulse in center of the quartz bar Q1.

10. Cable system

Each FFD module is connected (1) by a HDMI cable with the sub-detector electronics unit (SDU), (2) by a HV cable with the HV power supply, (3) by a 50- Ohm coaxial cable with CAEN mod. N6742 digitizers, and (4) by a quartz fiber with fiber bundle of the laser calibration system.

Additional cables are needed for connection between the SDUs of both FFD sub-detectors and the main and local readout electronics and the vertex electronics VU. The Detector Control System (DCS) also uses some cables for realization of its functions. The data from the local readout electronics, CAEN mod. N6742 modules, are transferred via optical link to a computer.

The high-quality HDMI cables are used for transport of LVDS pulses from FEE to main electronics unit SDU. The list of cables is given in Table 10-1.

The cables are laid out in a plane behind TPC to minimize material budget on a path of particles. We use one of 28 outlets in the magnet for output of the cables. Each sub-detector cable output needs 20×13 cm^2 pass in one from 2×28 outlets of the MPD magnet as it is shown in Fig. 10-1. The sub-detector electronics and readout electronics are located on the

upper platform of the MPD setup, close to the cable output from the magnet providing a minimal length of the cables.

Table 10-1. Total list of the cables of the FFD system.

#	Cable	Cable type	Length (m)	Number (units)
	FFD modules			
1	50-Ohm coax.	K02252D /TFD	10	80×2
2	HDMI	VAA-A01-S500bHigh Speed	8	20×2
3	HDMI	SM1815, High Speed W/E	1	20×2
4	HV	HV FFB	20	20×2
	TDC readout			
5	MOLEX	Molex P/N 11102512xx	3	10
6	MOLEX	Molex P/N 11102512xx	8	1
	CAEN digitizers			
7	50-Ohm coax.	RG316 /TFD	0.4	68×2
8	Optical link	LC/UPC-LC/UPC-D-MM/62,5	15	4
	Vertex Unit			
9	50-Ohm coax.	K02252D /TFD	8	2
	Laser system			
10	Optical cables	WF 100 / 140 / 190 / 300 N	10	20×2
11	Optical cables	WF 100 / 140 / 190 / 300 N	1	20×2
	Reference Detector			
12	HV	HV FFB	1	1
13	50-Ohm coax.	K02252D /TFD	8	1
14	50-Ohm coax.	K02252D /TFD	0.4	1
15	HDMI	VAA-A01-S500bHigh Speed	8	3

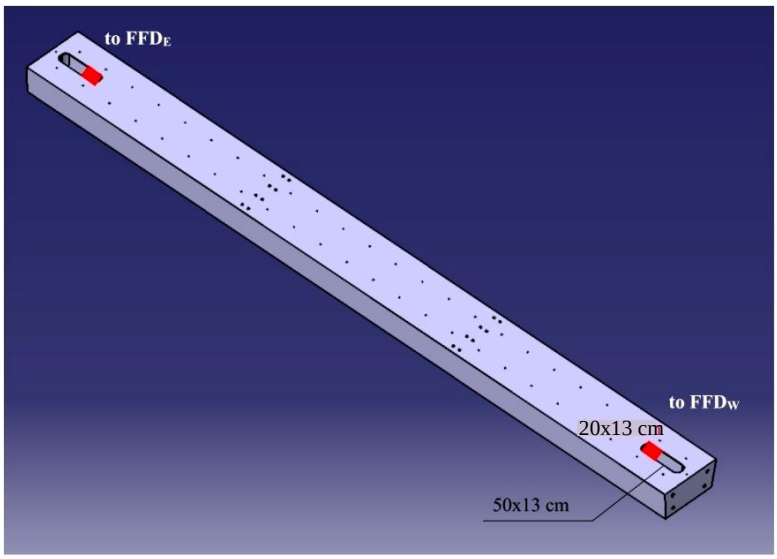

Fig. 10-1. Two passes in the MPD magnet outlets for the FFD cables.

11. Cooling

The temperature around FFD assembly in MPD is not under control. Contributions to the power consumption into FFD module by FEE and HV divider are ~0.4 and ~0.5 W respectively and it leads to some increasing of temperature inside the module. On other hand, the proper operation of MCP-PMT XP85012 requires a definite temperature regime with the maximum temperature of 50^{o} C. Some results of test measurements with a single FFD module at different surrounding conditions and room temperature of ~24^{o}C are shown in Tabl. 11-1. As it was expected, the highest temperature inside the module was obtained with thermoisolated side surfaces and the minimal discrepancy between outside and inside temperatures was measured for module placed on a large aluminum plate.

Table 11-1. Results of temperature measurements with a single FFD module.

#	conditions	T_{outer} (C)	T_{inner} (C)	ΔT (C)
1	Module thermoisolated around side surface	24.5	34	9.5
2	Module itself	24.0	29.3	5.3
3	Module connected with Al plate	24.4	27.5	3.1
4	Module connected with Al plate	23.2	26.8	3.6

For keeping the temperature around +30^{o} C inside the modules of the FFD arrays, more careful experimental tests and calculations will be performed in the nearest future with aim to find an optimal regime of the cooling using a flow of nitrogen gas.

12. Detector design

The 3D design of FFD was made in framework of Autodesk Inventor Professional. The FFD sub-detector assembly with mechanics and beam pipe is shown in Fig. 12-1 (the cables are not shown).

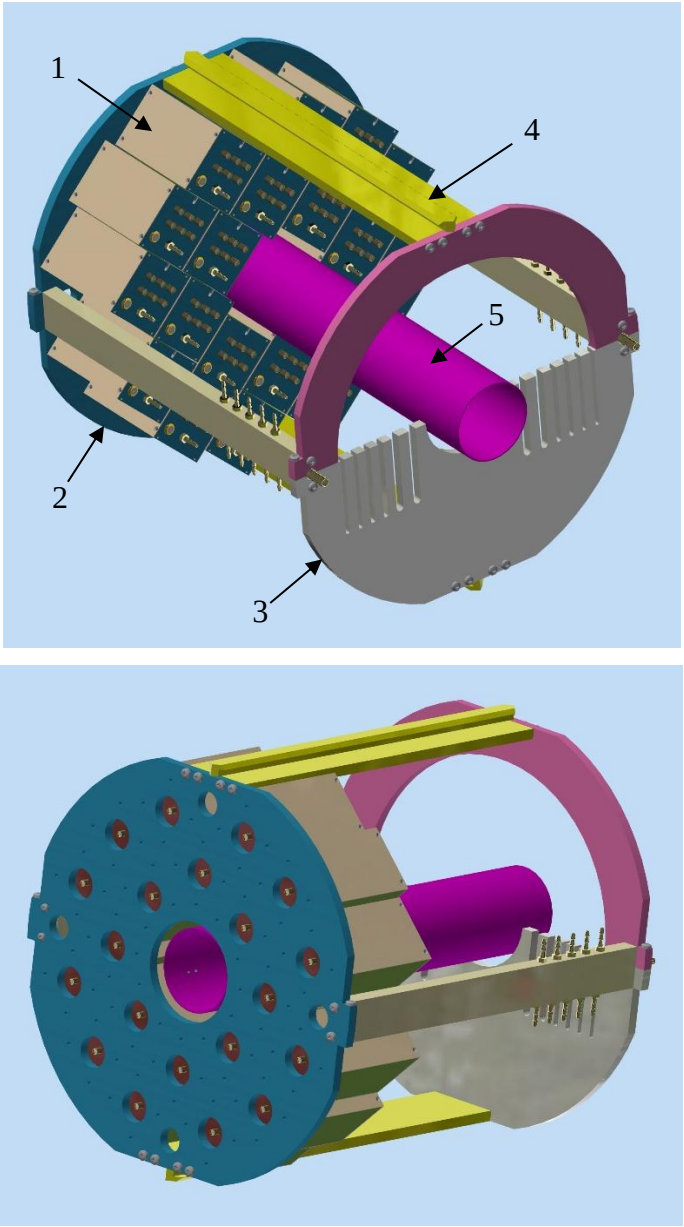

Fig. 12-1. A view of assembly of FFD sub-detector: 1 – the modules, 2 – the mechanical support of FFD modules, 3 – the mechanical support of cables, 4 – the support of sub-detector assembly, 5 – the beam pipe.

The requirements for detector design are

- small dead space in FFD arrays,
- nonmagnetic materials,
- minimal mass of the detector mechanics,
- convenience in mounting and dismounting,
- floating ground, FFD modules don't have electrical contact with MPD mechanics,
- geometrical compatibility with other detectors in MPD setup.

All mechanical elements are made from polymeric material Tecaform AH (POM-C) which has good mechanical and dielectric properties.

Whole FFD setup with FFD_E and FFD_W arrays fixed on two aluminum profiles (rails) along the beam pipe, is shown in Fig. 12-2. The aluminum profiles are fixed to the main aluminum frame of the MPD.

The mass of the FFD sub-detector is ~45 kg, its outer diameter is ~360 mm, the hole diameter for the beam pipe is ~92 mm, and the thickness is 45 cm.

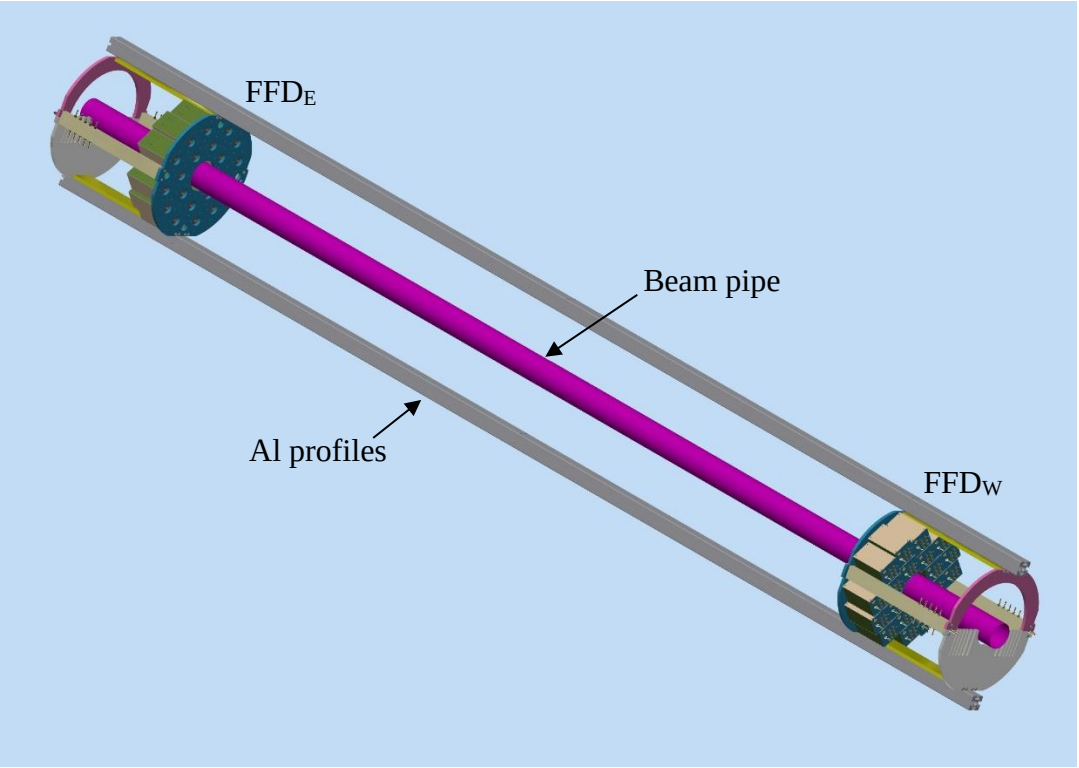

Fig. 12-2. A view of whole FFD setup.

13. Integration in MPD

The installation of the FFD sub-detectors is made on special aluminum profiles (rails) fixed to the main aluminum frame of the MPD which also supports the TPC. By these rails the sub-detectors FFD_E and FFD_W can be moved into the TPC inner tube to the FFD position. The distance of moving into the TPC is 30 cm.

The installation of the FFD sub-detectors in the MPD setup is carried out after installation of main MPD detectors (TOF, ECAL, TPC) and the beam pipe. The installation procedure has the following stages:

1. Putting the cables along the aluminum profile of the TPC outer wheel,
2. Mounting the detector around the beam pipe,
3. Cabling and connecting to FFD modules,
4. Moving the sub-detector arrays into the TPC inner tube to its position.

The de-installation is fulfilled in the opposite way.

A view of the FFD sub-detectors inside the MPD setup is shown in Fig. 13-1 and Fig. 13-2.

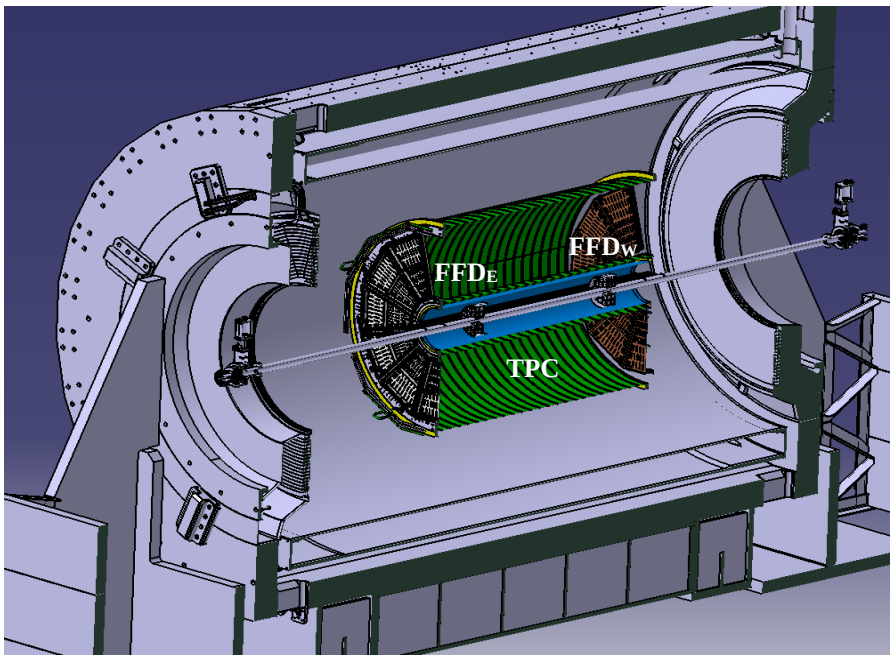

Fig. 13-1. A view of the FFD sub-detectors inside the MPD setup.

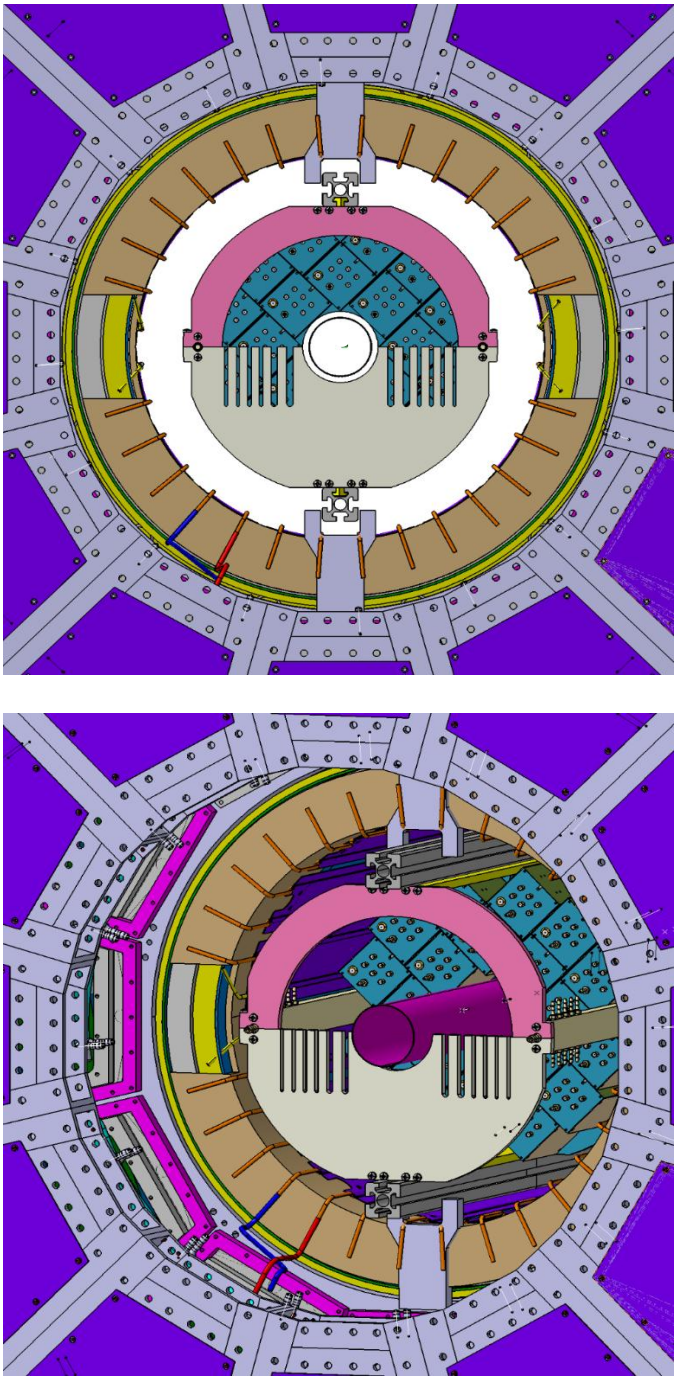

Fig. 13-2. A view of the FFD installed into the TPC inner hole with the vacuum beam pipe.

A special mechanical system is used in period of FFD installation. This mechanics is applied for assembly the sub-detectors outside the TPC and it includes two rails, the same as the aluminum profiles used for FFD sub-detector support in MPD setup. These rails are mechanically connected with the main rails for moving of the sub-detectors to its position after the assembly.

The FFD electronics and equipment are settled in three racks as it is shown in Fig. 13-3. The two racks are identical and contain the sub-detector electronics and optical patch panel. These racks are located close to cable outlets of the MPD magnet. The central rack is place for the laser system, the trigger electronics, HV crate and computer. The racks are located on platform and overpass of the MPD facility.

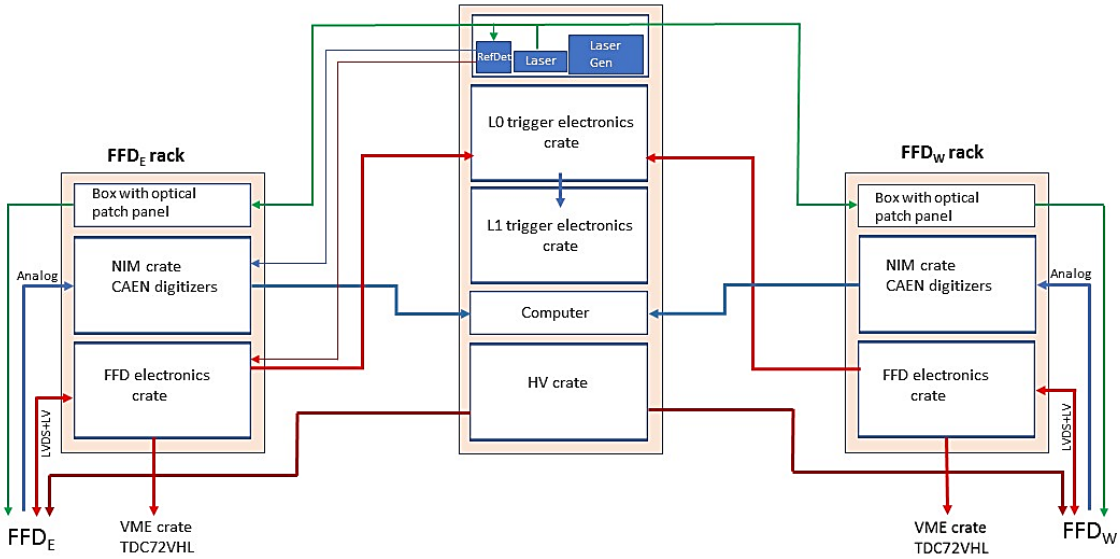

Fig. 13-3. The racks with the FFD electronics and equipment.

14. Commissioning

Currently a commissioning road map is being developed by the MPD collaboration.

The plan of FFD module and electronics production is based on the experience and results obtained with prototypes during last years. The 2018 – 2019 period is dedicated to

- module production and tests with cosmic rays and beam of Nuclotron,
- the study with prototypes of FFD electronics with aim to begin the production of electronics modules in 2019,
- the final design of calibration system, delivery of some components, production of the system, and tests,
- the cable production and delivery,
- the development of DCS (detector control system).

The digitizers CAEN mod.N6742 for the FFD local DAQ and the high voltage system from ISEG/WIENER have been delivered in 2018.

The main readout electronics based on TDC72VHL modules will be produced and tested in 2019. Also, in this year the laser calibration system will be completed and tested. A single sub-detector modular array will be constructed in late 2019.

Next year 2020 is dedicated to production and testing of the FFD sub-detectors, electronics and the detector control system.

Special mechanics and tools for installation of FFD in the MPD are under development and it is a part of common plan of the MPD collaboration.

15. Safety

The FFD modules and support system are manufactured out of aluminum, lead, quartz, and carbon fibre with some safe materials inside the modules. Cables and connectors conform to the required fire standards. Thus, we identify no particular safety concerns in the use of materials.

Detectors and electronics are supplied with low voltage ($< \pm 10$V) and high voltage (< -1.5 kV). The power supplies are located in the racks with electronics outside the MPD detector volume. They are remotely controllable and are enabled with automatic trip mechanism activated by the drawn current. Monitoring of the currents are enable to switch off automatically in case of too high current and report errors to the Detector Control System.

16. FFD organization

All participants in the FFD project are specialists of Laboratory of high energy physics, JINR. The list of participants is:

Vladimir Yurevich (project leader)

Sergey Sedykh (FFD modules, tests, DAQ, data analysis, calibration system)

Sergey Sergeev (electronics, trigger, detector control system, HV power supply)

Dmitriy Bogoslovsky (electronics, trigger, low voltage power supply)

Viktor Rogov (electronics, FFD modules, test stand, cable system)

Vladimir Tikhomirov (detector design, FFD mechanics, installation to MPD, cooling)

Alexander Timoshenko (mechanics of FFD modules, test stand, calibration system)

Nikita Lashmanov (FFD modules, tests, data analysis, calibration system)

Geidar Agakichiev (data analysis)

Georgiy Averichev (test measurements)

Gennady Yarigin (cable system, test stand)

Anatoliy Zubarev (mechanics)

Valeriy Pavlyukevich (mechanics)

Vladislav Kuzmin (HV power supply, electronics)

17. Time table

The timetable for the FFD project is given in Table 16-1.

Table 16-1. The timetable for the FFD project.

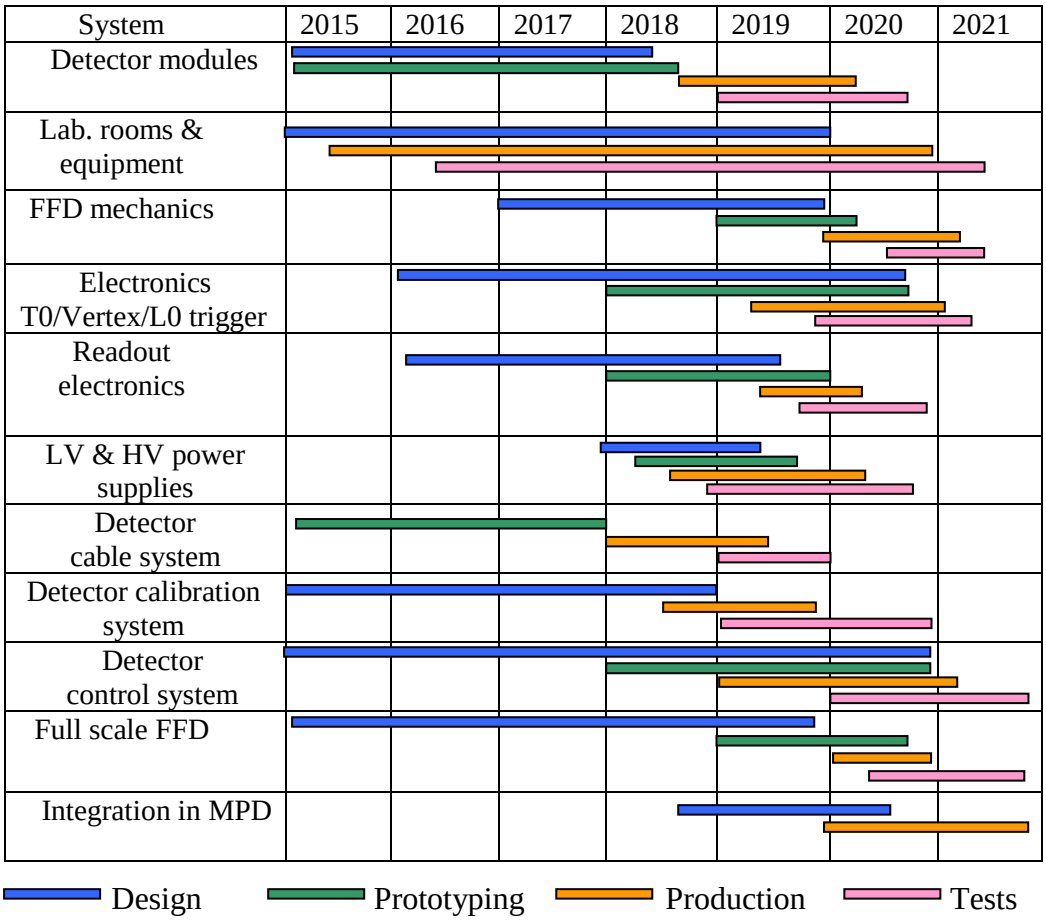

18. Detector budget

The detector budget in k$ is given in Table 15-1. The cost of MCP-PMTs XP85012/A1 takes 485 k$ of the budget.

Table 15-1. The budget of the FFD (k$).

#	Subject	-2015	2016	2017	2018	2019	2020	2021	Total
1	Detector modules	320	194.2	2.7	5.1	14	5		541
2	Lab. rooms & equipment	100		30	25.9	2	30	2.1	190
3	FFD mechanics			4.4	5.3	2	10	3.3	25
4	Electronics T0/Vertex/L0 trigger	3.6	1.1	11.8	52	31	10	5.5	115
5	Readout electronics			52.8	30.5	15	15	1.7	115
6	LV & HV power supplies			22		1	4		27
7	Detector cable system		0.7		4.7	26	10	3.6	45
8	Detector calibration system	40			0.6	22	5	2.4	70
9	Detector control system						10	10	20
10	Full scale FFD						10	12	22
11	Integration into MPD						20	10	30
	Sum:	463.6	196	123.7	124.1	113	129	50.6	**1200 k$**

References

1. *Ikematsu K. et al.* Nucl. Instr. Meth. A. 1998. V.411. P.238.
2. *Allen M. et al.* Nucl. Instr. Meth. A. 2003. V.499.P.549.
3. *Back B. B. et al.* Nucl. Instr. Meth. A. 2003. V.499.P.603.
4. *Bengtson B., Moszynski M.* Nucl. Instr. Meth. 1970. V.81. P.109.
5. *Bondila M. et al.* IEEE Transactions on Nucl. Sci. 2005. V.52. P.1705.
6. *ALICE collaboration.* The T0 Detector. ALICE TDR 011, CERN-LHCC-2004-025, Sep. (2004).
7. *The ALICE collaboration* Technical Design Report for the Upgrade of the ALICE Read-out & Trigger System. CERN-LHCC-2013-019 / LHCC-TDR-015, 3 July 2014.
8. *Karavicheva T.* The Fast Interaction Trigger detector for the ALICE Upgrade. ICPPA 2016, Oct. 10-14, 2016.
9. *Llope W. J. et al.* The STAR vertex position detector. arXiv:1403.6855v1 [physics.ins-det] 26 Mar 2014.
10. *Amelin N. S., Gudima K. K., and Toneev V. D.* Sov. J. Nucl. Phys. 1990. V.51. P.327; V.52. P.172.
11. *Mashnik S. G., A.J. Sierk A. J., K.K. Gudima K. K., and M.I. Baznat M. I.* J. Phys.: Conf. Series 2006. V.41. P.340.
12. *Mashnik S. G., Gudima K. K., Mokhov N. V., and Prael R. E.* arXiv:0709.1736 [nucl-phys].
13. www.photonis.com.
14. *Schyns E.* Workshop on Large Area Photo-Detectors, Electronics for Particle Physics and Medical Imaging, Clermont Ferrand, Jan. 28, 2010.
15. *Va'vra J. et al.* Report SLAC-PUB-12803, Sep. 2007.
16. *Albrow M. G. et al.* Quartz Cherenkov counters for fast timing: QUARTIC, arXiv:1207.7248v1 [physics.ins-det] 31 Jul 2012.
17. *Korpar S. et al.* Nucl. Instr. Meth. A. 2009. V.595. P.169.
18. *Garcia L. C.* DT Detectors Physics Meeting, CERN, 14 June 2011.
19. *Lehmann A.* RICH 2010, Cassis, France, May 2010.
20. *Va'vra J. et al.* RICH 2010, Cassis, France, May 2010; Report SLAC-PUB-14279, Oct. 2010.
21. *Britting A. et al.* Workshop on fast Cherenkov detectors, Giessen, Apr. 2011, 2011 JINST 6 C10001.

22. www.psi.ch/drs/evaluation-board.
23. Internet site: afi.jinr.ru/TDC
24. *Yurevich V. I. et al.* Fast forward detector for MPD/NICA project: concept, simulation, and prototyping. Phys. Part. Nucl. Lett. 2013. V.10(3). P.258 – 268.
25. *Yurevich V. I.* Development and study of picosecond start and trigger detector for high-energy heavy ion experiments. 7th International Conference on New Developments In Photodetection (NDIP14). 30 June – 4 July 2014, Tours, Nucl. Instr. Meth. A787 (2015) 308.
26. *Yurevich V. I.* Modular Detector with Picosecond Time Resolution. The Technology and Instrumentation in Particle Physics conference (TIPP 2014). 2-6 June 2014, Amsterdam.
27. *Yurevich V. I., BatenkovO. I. et al.* Beam Tests of Cherenkov Detector Modules with Picosecond Time Resolution for Start and L0 Trigger Detectors of MPD and BM@N Experiments, Phys. Part. Nucl. Lett., 2015, Vol. 12, No. 6, pp. 778.
28. *Yurevich V. I., Batenkov O. I.* Picosecond Cherenkov detectors for high-energy heavy ion Experiments at LHEP/JINR, 13th Pisa Meeting on Advanced Detectors – Frontier Detectors for Frontier Physics, 24 – 30 May 2015, Elba, Italy, Nucl. Instr. Meth. A824 (2016) 162.
29. *Yurevich V. I., Agakichiev G. N., Sergeev S. V., Bogoslovski D. N., Lobastov S. P., Rogov V. Yu., Averichev G. S., Tikhomirov V. V., Timoshenko A. A.* Development of trigger and start detectors for experiments with high-energy heavy ions at JINR, The 2017 International Conference on Applications of Nuclear Techniques, Crete, Greece June 11-17, 2017, Intern. Journal of Modern Physics: Conference Series.
30. *Yurevich V. I., Agakichiev G. N., Sergeev S. V., Bogoslovski D. N., Rogov V. Yu., Lobastov S. P., Averichev G. S., Tikhomirov V. V., Timoshenko A. A.* Cherenkov and scintillation detectors with MCP-PMT and SiPM readout for MPD and BM@N experiments at JINR, The International Conference on New Developments In Photodetection – NDIP 17, 3 – 7 July 2017, Tours, France.